EFFECT OF STEADY AND TIME-HARMONIC MAGNETIC FIELDS ON MACROSEGREGATION IN ALLOY SOLIDIFICATION

F. P. Incropera and P.J. Prescott

School of Mechanical Engineering
Purdue University
W. Lafayette, IN 47907

ABSTRACT

Buoyancy-induced convection during the solidification of alloys can contribute significantly to the redistribution of alloy constituents, thereby creating large composition gradients in the final ingot. Termed *macrosegregation,* the condition diminishes the quality of the casting and, in the extreme, may require that the casting be remelted. The deleterious effects of buoyancy-driven flows may be suppressed through application of an external magnetic field, and in this study the effects of both steady and time-harmonic fields have been considered. For a steady magnetic field, extremely large field strengths would be required to effectively dampen convection patterns that contribute to macrosegregation. However, by reducing spatial variations in temperature and composition, turbulent mixing induced by a time-harmonic field reduces the number and severity of segregates in the final casting.

INTRODUCTION

During solidification of an off-eutectic metal alloy, zones of pure solid and liquid are separated by a two-phase (solid/liquid), or *mushy*, region, consisting of fluid saturated dendritic structures. When solidification is induced by chilling a static mold from the side and/or from below, dendritic crystals which initially form at the cold surface may reject a lighter constituent which is redistributed by the combined influence of solutal and thermal buoyancy forces in the mushy and molten zones. Composition changes within the mushy zone may also induce regions of localized remelting in which channels develop and provide preferential paths for the flow of interdendritic fluid. The channels ultimately become sites of large composition gradients (termed *segregates*), and the large-scale redistribution of constituents in a fully solidified ingot is termed *macrosegregation.* One objective of research on alloy solidification is to reduce macrosegregation by altering patterns of natural convection inherent in the solidification process. Options include solidification in a μ-gravity environment or active control of the process by thermal, mechanical or electromagnetic means. In the following sections consideration is given to the effects of both steady and time-harmonic magnetic fields on flow and macrosegregation occurring during solidification.

Regardless of the manner in which a magnetic field is applied, the induced Lorentz force is determined by a cross product of the current density and the field strength, $\mathbf{F_L} = \mathbf{J} \times \mathbf{B}$. For a moving medium, the current density follows from Ohm's law, $\mathbf{J} = \sigma_e(\mathbf{E} + \mathbf{V} \times \mathbf{B})$, where σ_e is the electrical conductivity of the medium, $\mathbf{E}$ is an externally applied electric field, and $\mathbf{V} \times \mathbf{B}$ is the electric field induced by fluid motion through the magnetic field. *Magnetic damping* occurs when an electrically conducting fluid flows transversely through a steady magnetic induction field, and with $\mathbf{E} = 0$, the Lorentz force reduces to $\mathbf{F_L} = \sigma_e(\mathbf{V} \times \mathbf{B}) \times \mathbf{B}$. In contrast to the passive (dissipative) influence exerted by a steady (d.c.) magnetic field on a convecting liquid metal, a time-harmonic (a.c.) magnetic field has an active influence which involves stirring of the molten alloy. The electric field induced by a time-varying magnetic field drives eddy currents, which interact with the magnetic field to induce the Lorentz forces. In this study an external inductor is configured to provide a traveling magnetic field in a vertical, annular mold. The field is characterized by its angular frequency ω, axial phase variation (wave number) k_ϕ, and phase velocity $V_\phi = \omega/k_\phi$.

MATHEMATICAL MODEL

A continuum model for transport phenomena in binary, solid-liquid phase change systems (Prescott et al., 1994) has been extended to account for the effects of magnetic damping or electromagnetic stirring (EMS). Assuming two-dimensional (r,z) conditions in a vertical, annular mold, the model transport equations for conservation of total mass, axial and radial momentum, energy and species may be expressed as

$$\frac{\partial \rho}{\partial t} + \nabla\cdot(\rho \mathbf{V}) = 0 \tag{1}$$

$$\frac{\partial}{\partial t}(\rho u) + \nabla\cdot(\rho \mathbf{V} u) = \nabla\cdot\left[(\mu_l + \mu_t)\frac{\rho}{\rho_l}\nabla u\right] - \frac{\mu_l}{K}\frac{\rho}{\rho_l}(u - u_s) + \rho_l B_{lz} - \frac{\partial P}{\partial z} + F_{L,z} \tag{2}$$

$$\frac{\partial}{\partial t}(\rho v) + \nabla\cdot(\rho \mathbf{V} v) = \nabla\cdot\left[(\mu_l + \mu_t)\frac{\rho}{\rho_l}\nabla v\right] - (\mu_l + \mu_t)\frac{\rho}{\rho_l}\frac{(v - f_s v_s)}{r^2} - \frac{\mu_l}{K}\frac{\rho}{\rho_l}(v - v_s) - \frac{\partial P}{\partial r} + F_{L,r} \tag{3}$$

$$\frac{\partial}{\partial t}(\rho h) + \nabla\cdot(\rho \mathbf{V} h) = \nabla\cdot\left[\left(\frac{k}{c_s^*} + \frac{g_l \mu_t c_l}{Pr_t\, c_s^*}\right)\nabla h\right] + \nabla\cdot\left[\left(\frac{k}{c_s^*} + \frac{g_l \mu_t c_l}{Pr_t\, c_s^*}\right)\nabla\left(h_s^* - h\right)\right]$$
$$- \nabla\cdot[f_s \rho(\mathbf{V} - \mathbf{V}_s)(h_l - h_s)] \tag{4}$$

$$\frac{\partial}{\partial t}\left(\rho f^\alpha\right) + \nabla\cdot(\rho \mathbf{V} f^\alpha) = \nabla\cdot\left[\left(\rho D + \frac{f_l \mu_t}{Sc_t}\right)\nabla f^\alpha\right] + \nabla\cdot\left[\left(\rho D + \frac{f_l \mu_t}{Sc_t}\right)\nabla\left(f_l^\alpha - f^\alpha\right)\right]$$
$$- \nabla\cdot[f_s \rho(\mathbf{V} - \mathbf{V}_s)(f_l^\alpha - f_s^\alpha)] \tag{5}$$

where B_{lz} is the net (thermal/solutal) buoyancy force per unit mass of liquid and F_L is the Lorentz force.

For the magnetic damping conditions of this study, the Lorentz force is oriented exclusively in the radial direction ($F_{L,z} = 0$) and the corresponding force component is $F_{L,r} = -\sigma_e B_z^2 v$. Moreover, since turbulence generation is negligible, $\mu_t = 0$. In contrast, for EMS, Lorentz forces are manifested principally in the vertical direction and turbulent mixing is a likely consequence of the stirring action. The radial dependence of $F_{L,z}$ has been determined (Prescott and Incropera, 1994), and a low Reynolds number k-ε model (Launder and Spalding, 1974) has been used to evaluate the turbulent viscosity μ_t (Prescott and Incropera, 1995). Turbulence has the effect of increasing the effective viscosity, $\mu_{eff} = \mu_l + \mu_t$, and a dimensionless viscosity may be defined as $\mu^* = (\mu_l + \mu_t)/\mu_l$. Effective Prandtl and Schmidt numbers may also be defined as $Pr_{eff} = \nu_{eff}/\alpha_{eff} = Pr\,\mu^*/\left[1 + Pr(\mu^* - 1)/Pr_t\right]$ and $Sc_{eff} = \nu_{eff}/D_{eff} = Sc\mu^*/\left[1 + Sc(\mu^* - 1)/Sc_t\right]$. For the Pb-Sn system, Pr = 0.02 and Sc = 172 (Le = Sc/Pr = 8600). Hence, for representative values of $\mu^* = 100$, $Pr_t = 1.2$, and $Sc_t = 1.0$, $Pr_{eff} = 0.75$ and $Sc_{eff} = 1$, yielding an effective Lewis number of 1.33. Although the respective molecular diffusion rates of momentum, energy, and species are highly disparate, turbulence has the effect of approximately equalizing these diffusion rates. Furthermore, by increasing the effective diffusion coefficients for all field variables, turbulence reduces the influence of advection, rendering all transport rates less sensitive to velocity *vectors* and more sensitive to *gradients* in the respective field variables.

Calculations were performed for an experimental mold cavity of height H = 150 mm and inner and outer radii of $r_i = 15.9$ and $r_o = 63.5$ mm, respectively. The mold contains a molten charge of Pb-19 wt pct Sn, which is initially at 305°C, and solidification is initiated by subjecting the side wall to cooling characterized by a chill temperature of $T_c = 13$°C and an overall coefficient of $U = 35\ W/m^2{\cdot}K$. For magnetic damping, field strengths of $B_z = 0.1$ and 0.5 T are considered. For EMS a downward magnetic field characterized by $\omega = 377$ rad/s, $k_\phi = -29$ rad/m and $B_r(r_o) = 2.9$ mT (rms) is considered.

RESULTS

Magnetic Damping. Three simulations, corresponding to values of $B_z = 0$, 0.1 and 0.5 T, were performed to assess the effects of magnetic damping. For the base case, $B_z = 0$ (Fig. 1), a strong, counterclockwise thermal convection cell is established shortly after the sidewall is chilled, and within t = 120 s, crystals begin to precipitate at the bottom of the mold wall, thereby forming a two-phase (mushy) zone. As cooling continues, the mushy zone grows, with the liquidus interface moving vertically upward and radially inward. At t = 140 s, a thin mushy zone of nonuniform thickness is attached to the bottom one-third of the cooled mold wall. The precipitation of solid is accompanied by solute (Sn) enrichment of interdendritic liquid, Fig. 1i (d), which induces solutal buoyancy forces acting upward on the interdendritic liquid and opposing thermal buoyancy forces caused by the radial temperature gradient, Fig. 1i (c). Because the density of Sn is significantly less than that of Pb, solutal forces dominate within the mushy zone. Interdendritic fluid which escapes from the mushy zone at $z^* \approx 0.27$, Figs. 1i (a) and (b), is turned

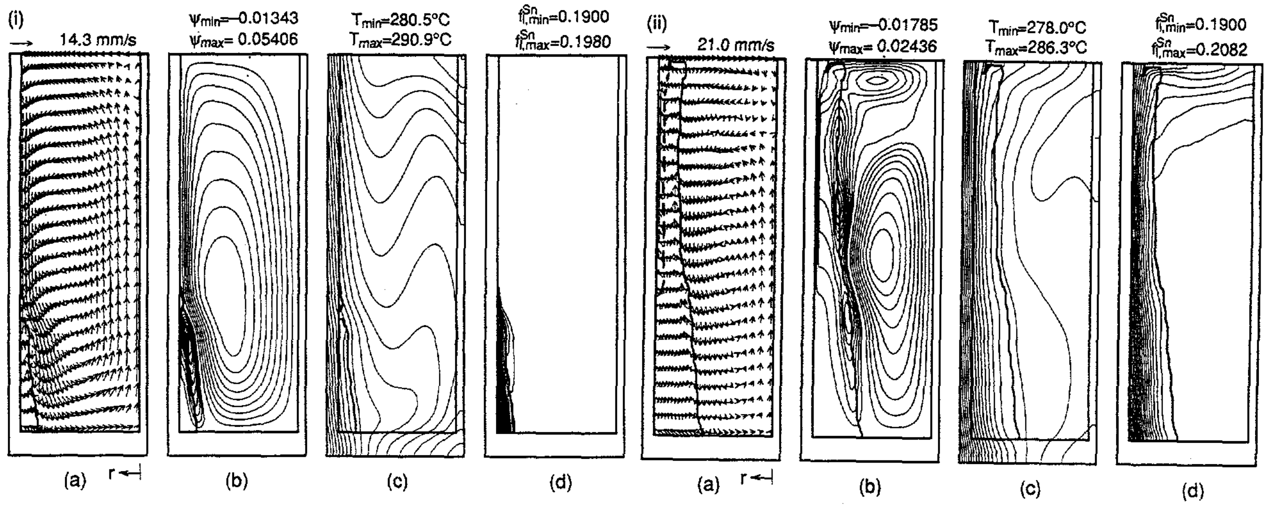

Fig. 1 Convection conditions after (i) t = 140 s and (ii) t = 175 s of cooling with no magnetic field: (a) velocity vectors, (b) streamlines, (c) isotherms, and (d) liquid isocomps.

downward along the liquidus interface by the momentum of the thermal convection cell, thereby confining the liquid composition gradient primarily within the mushy zone, Fig. 1i (d).

With time, the liquidus interface moves radially inward and vertically upward along the cooled mold wall. As this process occurs, fluid is exchanged between the mushy and melt zones in a relatively confined region near the top of the mushy zone, where a strong, solutally driven (Sn-rich) flow emerges from the mushy zone and interacts with thermally driven flow in the bulk melt, Fig. 1ii (b). Since the Pb-Sn system is characterized by a large Lewis number ($Le \approx 8600$), fluid within the solutal convection cell readily exchanges energy with the bulk liquid but largely retains its composition. As shown in Fig. 1ii (a), these conditions favor the development of a channel within the mushy zone. Since fluid ascending along the cooled mold wall is enriched with Sn, there is a depression in the local liquidus temperature, which is conducive to remelting. In addition, due to the advection of warm, Sn-rich fluid from the melt into the mushy zone, remelting is enhanced and a channel is spawned. The channel is aligned vertically along the mold wall and is delineated by a thick dashed line in Fig. 1ii (a). In addition to the exchange of liquid between the mush and melt promoted by the channel, three small recirculation cells are active along the liquidus interface at $z^* \approx 0.3, 0.6$, and 0.8, Fig. 1ii (b). Such recirculations are responsible for establishing preferred flow paths of interdendritic liquid at later times. Fluid of nominal composition enters the mushy zone at the bottom of these recirculation zones and displaces fluid of higher Sn concentration. Thus, a small Sn depleted region, with an increased solid fraction and decreased permeability, is created. At the top of a recirculation cell, there exists a Sn enriched zone with decreased solid fraction and increased permeability. The position of these interfacial recirculation cells moves as the liquidus interface advances inward and upward, thereby creating a series of channels, which manifest themselves as A-segregates in the final casting. The momentum associated with the thermal convection cell gradually decreases, as temperature gradients in the melt diminish and opposing solutal buoyancy forces increase.

For $B_z = 0.1$ T, development of the mushy zone and the solutally driven convection cell, Fig. 2i (b), is accelerated. Magnetic damping reduces the strength of the thermally driven circulation, thereby decreasing heat transfer between the melt and the cooled mold wall. Furthermore, due to the decreased momentum associated with the thermally driven downflow along the outer mold wall, Sn rich fluid from the mushy zone penetrates further into the melt, Fig. 2i (d). Since the thermal cell is weakened by the magnetic field, it is less effective at opposing the discharge of Sn rich liquid from the mushy zone, and the propensity for channel development is increased. A fully melted channel which turns radially inward from the outer mold wall, Fig. 2ii (a), provides a preferred flow path for interdendritic fluid, Fig. 2ii (b), facilitating its transfer to the top of the mold cavity, where Sn rich layers of liquid are forming, Fig. 2ii (d).

By increasing the induction field to 0.5 T, radial damping increases twenty-five fold, significantly reducing thermal convection and thermal stratification during the initial cooling period. At t = 140 s, Fig. 3i, a mushy zone covers nearly 90% of the vertical extent of the outer mold wall, the temperature gradient is primarily radial, and the positive buoyancy associated with the Sn concentration gradient in the interdendritic fluid produces an annular plume of Sn rich liquid ascending from the mushy zone. Since the magnetic field strongly dampens thermal convection during the initial cooling period, this solutal upwelling is virtually unopposed and is responsible for the channel which forms along the mold wall, where the local liquidus temperature is depressed. The strong magnetic damping causes the thermal and solutal convection cells to be sharply divided by a hypothetical cylindrical surface whose radius corresponds closely with the liquidus interface, Fig. 3i (b). With time, the mushy zone and the vertical interface between thermal and solutal convection cells move radially inward. Since vertical motion is undamped, solutal buoyancy forces continue to accelerate interdendritic fluid to relatively large velocities within the channel adjacent to the outer mold wall, while magnetic damping has the effect of minimizing radial motion. At t = 210 s, the counterclockwise thermal cell is virtually nonexistent, Fig. 3ii (b), and with the dominance of solutal buoyancy, solutal stratification eventually occurs.

Macrosegregation patterns at a time for which fluid flow is negligible and macrosegregation is essentially complete are shown in Fig. 4. The *A-segregates* of Fig. 4 (a)

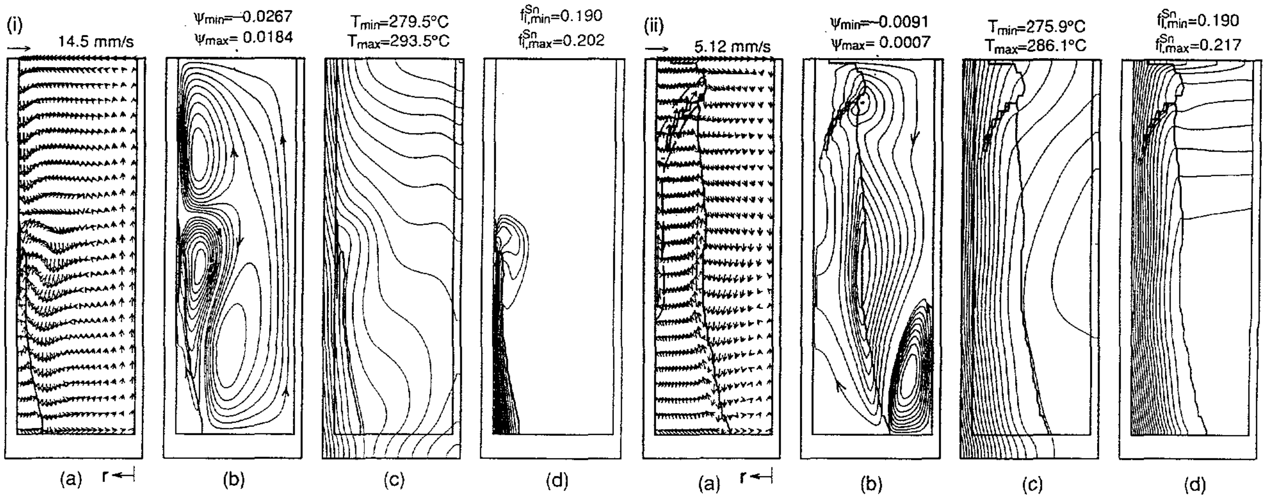

Fig. 2 Convection conditions after (i) t = 140 s and (ii) t = 210 s of cooling with $B_z = 0.1$ T: (a) velocity vectors, (b) streamlines, (c) isotherms, and (d) liquid isocomps.

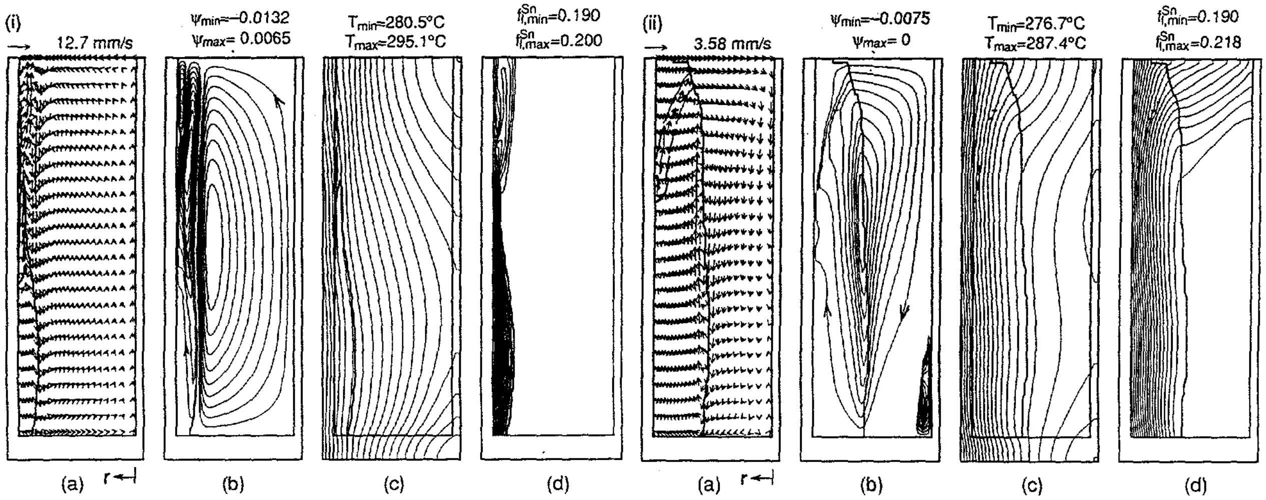

Fig. 3 Convection conditions after (i) t = 140 s and (ii) t = 210 s of cooling with $B_z = 0.5$ T: (a) velocity vectors, (b) streamlines, (c) isotherms, and (d) liquid isocomps.

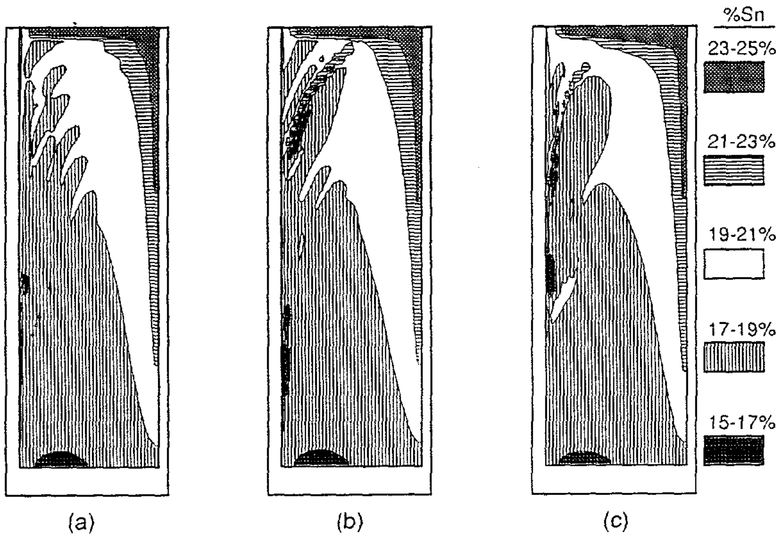

Fig. 4 Macrosegregation pattersn after 600 seconds of cooling: (a) without magnetic damping, (b) with $B_z = 0.1$ T, and (c) $B_z = 0.5$ T.

correspond to a series of Sn-rich pockets extending upward and radially inward from a Sn-depleted region. In addition to the pattern of *A-segregates*, there is a large *cone segregate* of Sn-rich material, which extends downward from the top of the ingot and results from solutally induced flow during intermediate stages of solidification. Application of the magnetic field has virtually no influence on development of the cone of positive segregation, but does affect the patter of A-segregates. For B = 0.1 T, Fig. 4 (b), the channel that existed at earlier times yielded a highly segregated zone among the array of A-segregates, which consists of adjacent extremes in positive (Sn-rich) and negative (Sn-depleted) segregation. Although the number and severity of the A-segregates are reduced for $B_z = 0.5$ T, Fig. 4 (c), overall segregation remains pronounced.

Magnetic Stirring. With application of a downward traveling magnetic field ($k_\phi < 0$), the Lorentz force acts in the downward direction and decreases with decreasing radius. Hence, the corresponding recirculation is one for which fluid ascends near the inner radius of the cavity and descends near the outer radius, thereby augmenting and opposing thermal and solutal buoyancy forces, respectively.

Predictions based on the turbulent model yielded a large convection cell and melt velocities during the early stages of solidification. However, correspondingly large values of the effective viscosity suppressed development of the velocity field, and at t = 160 s, Fig. 5i, the maximum velocity is 12.1 mm/s, with $\mu^* = 208$. Solidification has progressed for approximately 10 s, and a mushy zone of highly nonuniform thickness covers approximately 60% of the mold wall. The main convection cell, Fig. 5i (b), is driven by Lorentz forces, while a solutally driven convection cell is developing near the bottom within the confines of the mushy zone. Although $\mu^* = 1$ along the mold walls, Fig. 5i (e), large levels of turbulence exist throughout the melt. Due to the combined effects of local turbulence generation and distance from the walls, at which the turbulence kinetic energy, k_e, is zero, the maximum effective viscosity μ^*_{max} occurs at $r^* \approx 0.5$ and $z^* \approx 0.7$, Fig. 5i (e). Turbulence is damped in the mushy zone, but significant turbulent mixing still occurs near the liquidus interface within the mushy zone and is responsible for reducing gradients in the liquid Sn concentration, Fig. 5i (d,e).

With rapid growth of the mushy zone and a concomitant reduction in fluid velocities, the mushy zone occupies almost the entire mold cavity at t = 180 s, Fig. 5ii. Although the turbulence intensity has also decreased significantly, Fig. 5ii (e), it still enhances mixing in the interior of the cavity, thereby maintaining nearly uniform temperatures and concentrations in much of the mushy zone, Fig. 5ii (c,d). The turbulence intensity is a maximum for $r^* \approx 0.5$ at the top surface, Fig. 5ii (e), where damping is small due to small volume fractions of solid. The solutal convection cell is growing and eventually dominates flow conditions in the cavity. However, because Lorentz forces oppose solutal buoyancy forces, the clockwise convection cell in Fig. 5ii (b) grows more slowly than it would without electromagnetic stirring. At t = 195 s, most of the turbulence has been dissipated by damping, and its influence is confined to relatively small interior regions near the very top and bottom of the cavity, Fig. 5iii (e), where solid volume fractions are relatively small. However, under the influence of prior, turbulence-induced mixing, uniform temperatures and liquid compositions persist in much of the mushy region, Fig. 5iii (c,d).

The solutal convection cell continues to grow, while the electromagnetically driven cell and turbulence gradually decay. By t = 210 s, solutal buoyancy dominates convection, forming layers of Sn-rich liquid and causing dendrites to remelt at the top. Convection conditions representative of intermediate stages of solidification are shown in Fig. 5iv, which corresponds to t = 240 s. Turbulence is virtually fully decayed, Fig. 5iv (e), and interdendritic liquid is recirculated through the cavity in one large convection cell, Fig. 5iv (a,b). The small, counterclockwise recirculation cell at the bottom of the cavity vanishes completely shortly after t = 240 s, due to the increasing radial gradient in liquid Sn concentration. The convection pattern supplies cool Sn-rich liquid to the top interior region of the cavity, Fig. 5iv (c,d), thereby establishing vertical gradients of temperature and liquid Sn concentration. In the outer periphery of the mold cavity, gradients in temperature and liquid concentration are primarily radial and nearly uniform in the vertical direction.

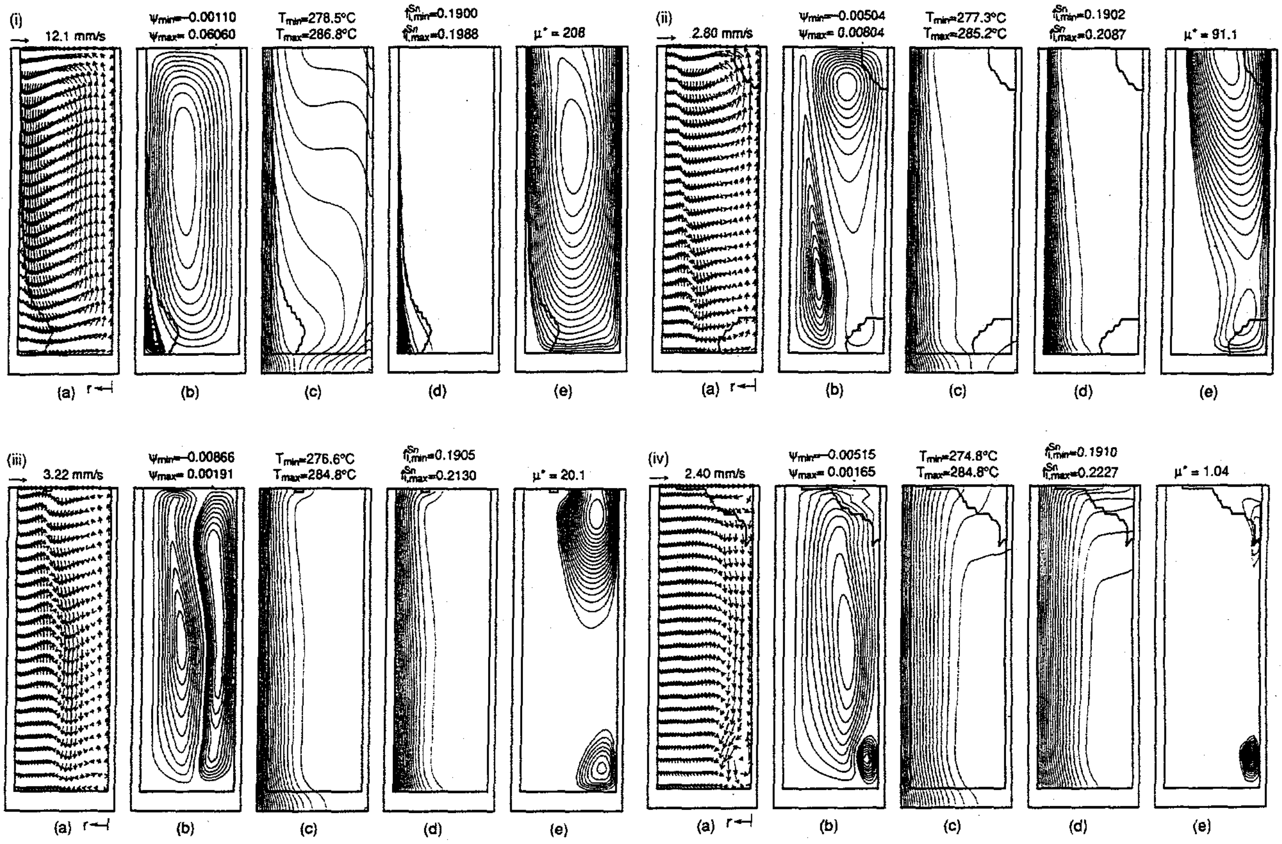

Fig. 5 Effect of EMS on conditions at (i) t = 160 s, (ii) t = 180 s, (iii) t = 195s and (iv) t = 240 s: (a) velocity vectors, (b) streamlines, (c) isotherms, (d) liquid isocomps, and (e) effective visocity (turbulence).

The subsequent development of macrosegregation patterns is shown in Fig. 6. At t = 240 s, Fig. 6 (a), macrosegregation is slight, with more than 95% of the partially solidified ingot remaining within 0.66% of the nominal composition. However, the solutal convection pattern of Fig. 5iv (b) is ultimately responsible for the formation of a cone of positive segregation at the top of the ingot, Fig. 6 (e), and although the overall rms macrosegregation is less than that predicted without electromagnetic stirring, the cone segregate of Fig. 6 (e) is only slightly smaller than that predicted without a magnetic field, Fig. 4 (a).

Turbulence has the effect of diminishing perturbations in the temperature and liquid concentration fields, thereby inhibiting the formation of channels in the mushy zone. With increased turbulent mixing, effective diffusion coefficients for momentum, energy, and species transfer are essentially equalized, decreasing the relative effect of advection and causing gradients in temperature and liquid Sn concentration to remain primarily radial and nearly uniform in the vertical direction. During early stages of solidification, counter-rotating convection cells driven by solutal buoyancy and Lorentz forces occupied the outer and inner portions of the cavity, respectively, with minimal mutual interactions and hence reduced the propensity for forming severely segregated regions associated with channels.

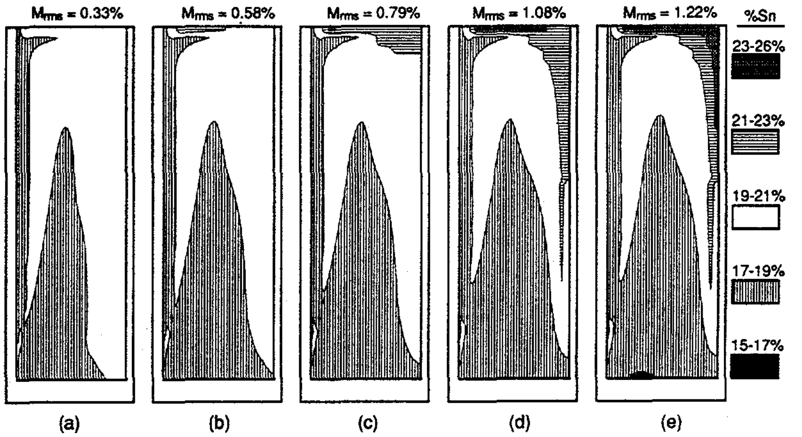

Fig. 6 Effect of EMS on macrosegregation patterns at (a) t = 240 s, (b) t = 300 s, (c) t = 360 s, (d) t = 480 s, and (e) t = 600 s.

SUMMARY

Options for suppressing the effects of natural convection on macrosegregation during the casting of molten alloys include active control of the solidification process by thermal, mechanical and/or electromagnetic means. However, results of this study indicate that, without unreasonably large field strengths, use of a *steady* magnetic field to *dampen* convection is not a viable option. In contrast, through a *stirring* action, use of a time-varying magnetic field of moderate strength has been shown to reduce the severity of macrosegregation.

ACKNOWLEDGEMENT

This work was performed under the auspices of the U.S. Department of Energy.

REFERENCES

1. Launder, B.E., and Spalding, D.B., 1974, "The Numerical Computation of Turbulent Flows," *Computer Methods in Applied Mechanics and Engineering,* Vol. 3, pp. 269-289.

2. Prescott, P.J., and Incropera, F.P., 1994, "Convective Transport Phenomena during Solidification of Binary Metal Alloys and the Effect of Magnetic Fields," TR DOE/ER/13759-7, School of Mechanical Engineering, Purdue University.

3. Prescott, P.J., and Incropera, F.P., 1995, "The Effect of Turbulence on Solidification of a Binary Metal Alloy with Electromagnetic Stirring," *J. Heat Transfer*, In Press.

THEORETICAL MODELING OF CHF FOR NEAR-SATURATED POOL BOILING AND FLOW BOILING FROM SHORT HEATERS USING THE INTERFACIAL LIFT-OFF CRITERION

Issam Mudawar†, Jesse E. Galloway‡, Christopher O. Gersey‡,
Stanley J. Reed‡, and David D. Hall‡

Boiling and Two-Phase Flow Laboratory
School of Mechanical Engineering, Purdue University
West Lafayette, IN 47907, U.S.A.

ABSTRACT

Pool boiling and flow boiling were examined for near-saturated bulk conditions in order to determine the critical heat flux (CHF) trigger mechanism for each. Photographic studies of the wall region revealed features common to both situations. At fluxes below CHF, the vapor coalesces into a wavy layer which permits wetting only in wetting fronts, the portions of the liquid-vapor interface which contact the wall as a result of the interfacial waviness. Close examination of the interfacial features revealed the waves are generated from the lower edge of the heater in pool boiling and the heater's upstream region in flow boiling. Wavelengths follow predictions based upon the Kelvin-Helmholtz instability criterion. Critical heat flux in both cases occurs when the pressure force exerted upon the interface due to interfacial curvature, which tends to preserve interfacial contact with the wall prior to CHF, is overcome by the momentum of vapor at the site of the first wetting front, causing the interface to lift away from the wall. It is shown this interfacial lift-off criterion facilitates accurate theoretical modeling of CHF in pool boiling and in flow boiling in both straight and curved channels.

---

† Professor and Director of the Purdue University Boiling and Two-Phase Flow Laboratory; author to whom correspondence should be addressed

‡ Graduate Student

1. INTRODUCTION

Predicting CHF has been the focus of a considerable body of research spanning over three decades. For pool boiling, the well known CHF model of Zuber *et al.* [1] has maintained its popularity because of its theoretical appeal and use of well-established hydrodynamic instability hypotheses in determining limits on liquid access to a horizontal surface. Many attempts have been made to alter this model in order to account for effects the original model did not address. These include finite heater size, heater geometry, and surface orientation. The latter of these effects, particularly the case of a vertical surface, is of special interest to the present study.

While the model by Zuber *et al.* [1] predicts zero CHF for vertical surfaces, experimental evidence proves CHF for this orientation and all orientations between horizontal and vertical are only slightly smaller than for a horizontal surface. Not only does this negate the suitability of this model for vertical surfaces, but it also raises questions concerning the CHF trigger mechanism on which the model is founded, even for horizontal surfaces. It is one of the key objectives of the present study to develop a new model for pool boiling CHF from vertical surfaces.

With regard to flow boiling, six main types of models have been proposed which encompass virtually all of the CHF research. These are *boundary layer separation* [2, 3, 4], *mechanical energy criterion* [5, 6], *bubble crowding* [7, 8, 9], *sublayer dryout* [10, 11, 12], and *interfacial lift-off* [13, 14, 15, 16]. The latter is the model discussed in the present paper.

Numerous, fairly reliable empirical CHF correlations also exist in the literature. However, in recent years, many researchers have refocused their efforts on determining the key physical mechanisms responsible for initiating CHF in pursuit of a universal CHF model.

The present study will first explore the trigger mechanism for CHF from a short vertical surface in near-saturated flow boiling using an apparatus which lends itself to high resolution photographic study of interfacial features. A model is proposed the validity of which will be tested for both straight and curved flow boiling. The curved flow configuration facilitates an assessment of the accuracy of the model in predicting the enhancement effects measured by many researchers due to curvature [17, 18, 19, 20]. This study will then treat pool boiling on a vertical surface simply as a limiting condition of flow boiling corresponding to zero liquid velocity. It will then be shown the proposed model reduces to a simple expression for pool boiling CHF.

2. EXPERIMENTAL METHODS

Straight and Curved Flow Boiling Visualization Facility

A CHF flow visualization apparatus was designed to maximize photographic access to interfacial features in close proximity to the heater surface in both straight and curved flows. The apparatus consisted of a curved flow channel having a 4.19-cm outer radius of curvature, which was located downstream from a straight channel. A 1.27-cm long heater was inserted in each of the straight and curved regions of the channel. As shown in Fig. 1, the flow channel was formed by milling a 0.16 cm × 0.64 cm slot into a transparent polycarbonate plastic (Lexan) plate. A second Lexan plate was clamped onto the first plate trapping an o-ring seal. The centerline of the curved heater was positioned at a 135-degree angle relative to the inlet flow. Both the straight and curved heaters were constructed from copper and heated by a thick-film electrical resistor silver soldered to the outer protruding surface. The heaters were inserted into insulating flanges made from G-10 fiberglass plastic. An o-ring was pressed between the base of each heater assembly and the flow channel plate providing a leak proof seal. FC-87, a 3M dielectric fluid, was tested at a pressure of 1.37 bars (T_{sat} = 39 °C) with 8 °C inlet subcooling. Tilting the entire flow channel module allowed all tests to be conducted in an upflow configuration with respect to the tested heater. Only one heater was operated at a time.

Pool Boiling Facility

Figure 2 shows a schematic of the pool boiling test chamber which was constructed of G-10 fiberglass plastic and fitted on the front and back with Lexan windows. The chamber was equipped with two condensers and three cartridge heaters. The condenser coiled inside the chamber effectively recovered all of the vaporized liquid. An external reflux condenser connected to the chamber's vent acted as a final barrier to any escaping vapor during both deaeration and testing. To prevent the boiling on the cartridge heaters from influencing CHF on the primary test heater, the cartridge heaters were placed at the back of the test chamber, isolated from the test heater by a baffle plate. Water and FC-72, another 3M dielectric fluid, were tested at atmospheric pressure. The FC-72 test heater consisted of a 12.7 × 12.7 mm^2 copper block which was heated by a thick-film electrical resistor silver soldered to its back. A similar configuration was used for pool boiling of water but with a heater measuring 12.0 × 62.0 mm^2. Each heater was mounted on an angular rotation platform to facilitate testing at different surface orientations.

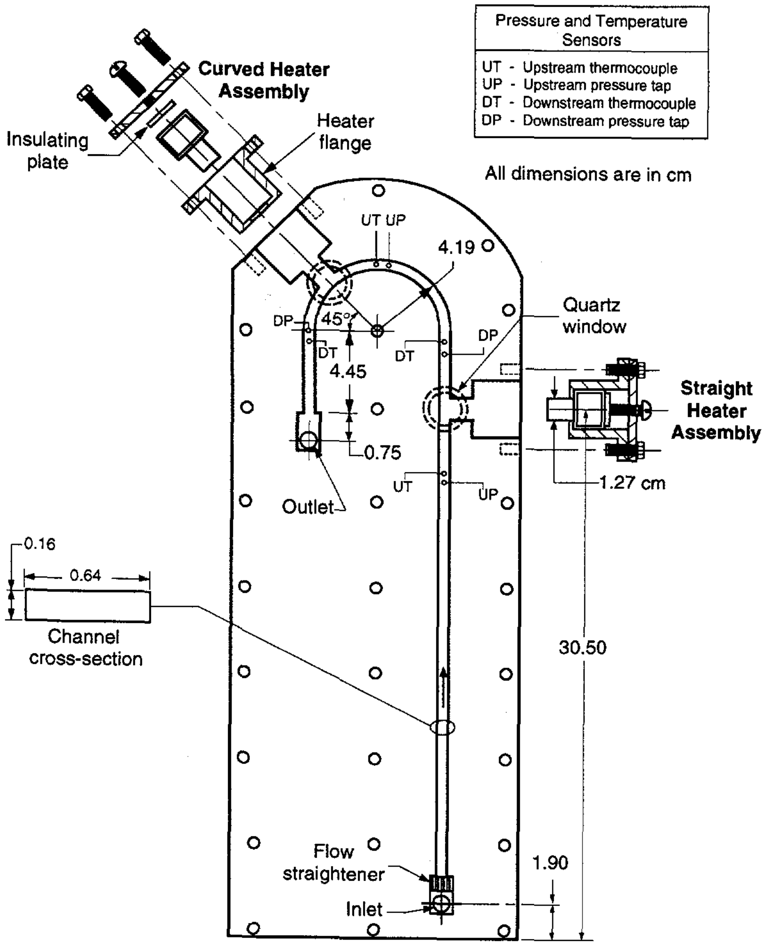

Figure 1. Flow Boiling Apparatus

3. PHOTOGRAPHIC STUDY OF VAPOR LAYER INTERFACIAL FEATURES

The flow and pool boiling facilities showed similar vapor production behavior at conditions leading to CHF. At a heat flux of about 85% of CHF, large coalescent bubbles were observed sliding over the heater surface. The length of these coalescent bubbles increased with increasing heat flux until, eventually, a fairly continuous wavy vapor layer was formed over the heater surface at heat fluxes below CHF. Boiling was sustained by liquid entrainment near the lower edge of the heater in pool boiling and the heater's upstream edge in flow boiling, as well as in *wetting fronts*, where the liquid-vapor interface made contact with the heater surface. Experimental evidence supporting this wetting front description is also available from studies by Fiori and Bergles [21], Hino and Ueda [22, 23], and Galloway and Mudawar [20]; all of whom measured fluctuations in heater surface temperature synchronous with the passage of vapor slugs.

Figure 3 shows the vapor layer formation on the curved heater in flow boiling corresponding to heat fluxes equal to 99% of CHF. Using a magnification better than 50×, no vapor jets could be seen emanating from the heater surface. Rather, a violent surge of small bubbles in the wetting fronts was observed to be feeding the vapor layer. The wavelength for both the straight and curved heaters decreased with increasing velocity. However, the curved heater exhibited significant differences in the shape of the wavy vapor layer as compared to the straight heater. For equal inlet velocities, the interfacial wavelength was greater for the straight heater than for the curved heater and, occasionally, at inlet velocities greater than 1.25 m/s, the curved heater projected vapor away from its surface in the form of vapor slugs which protruded from the wave peaks. No such behavior was observed with the straight heater.

Vapor layer mean thickness and wavelength were measured from high-speed video images captured by a 6000 partial frames per second Kodak EktaPro 1000 motion analyzer, which were later analyzed on a 55-cm wide screen; only still photography was used in the pool boiling tests. Thirty measurements were made for each inlet velocity to quantify the randomness of the interfacial features. Figure 4 shows the wavelength for the straight heater was greater than for the curved heater and the wavelengths for both heaters decreased with increasing inlet velocity. Figure 4 also compares the ratio of wavelength to mean thickness of the vapor layer for both heaters.

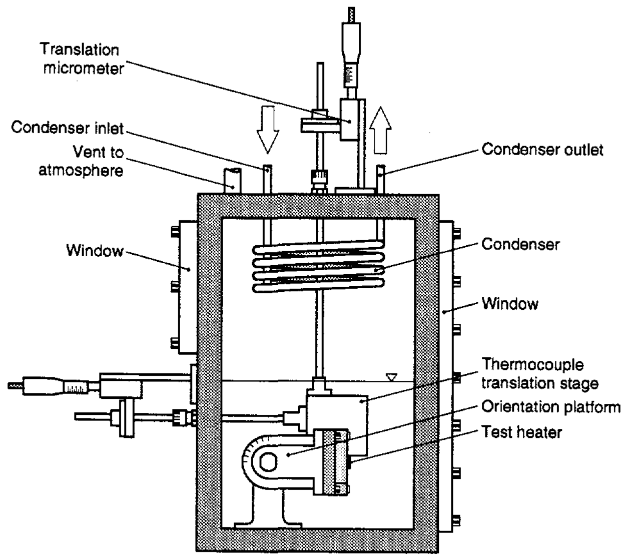

Figure 2. Pool Boiling Test Chamber

4. CHF MODEL

Model Assumptions

The proposed CHF model is built upon physical observations from extensive high speed video imaging studies as discussed in the previous section and illustrated in Fig. 5: (1) at heat fluxes approaching CHF, vapor coalesces to form a fairly continuous wavy vapor layer; (2) liquid is entrained at wetting fronts where the liquid-vapor interface contacts the heater surface; (3) vigorous boiling persists near the leading edge of the heater and in the wetting fronts while regions between neighboring wetting fronts dry out; (4) CHF commences when the liquid-vapor interface separates from the heater surface at the location of the most upstream wetting front; and (5) remaining wetting fronts are separated, in succession, after separation of the upstream wetting front.

As shown in Fig. 5, the first wetting front is established at a distance z^* from the leading edge and then propagates along the heater surface at a speed c_r. The vapor layer interfacial wavelength, $2\lambda_c$, was determined from hydrodynamic instability theory (discussed below) and observations made using the high-speed video imaging. When the liquid-vapor interface is unstable, a disturbance having a wavelength equal to λ_c is assumed to touch the heater surface at $z = z^*$ (z^* is

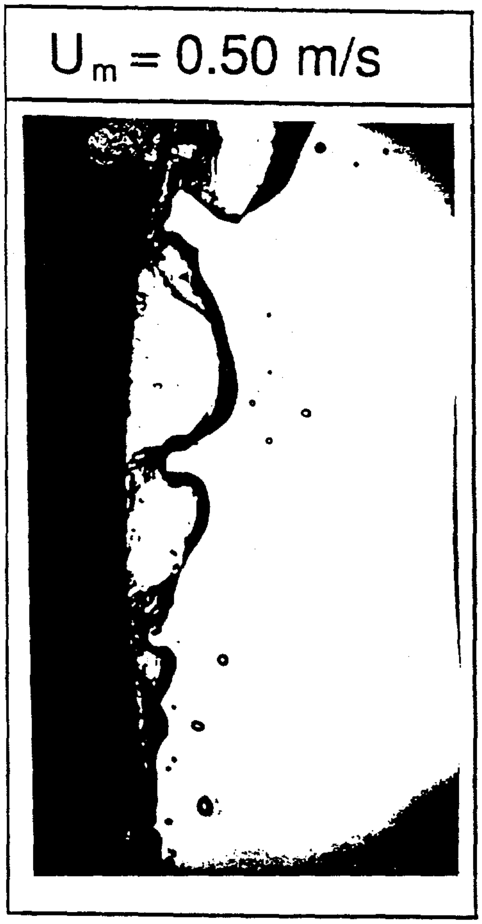

Figure 3. Wavy Vapor Layer Development on Curved Heater in Flow Boiling Just Prior to CHF

slightly greater than λ_c, the difference being a negligible distance z_0 over which the vapor velocity just exceeds the liquid velocity as discussed by Galloway and Mudawar [14]), enabling liquid to contact the heater over a localized region. A short time later, at $t = \lambda_c / c_r$, another disturbance approaching the heater surface will be forced away by the momentum of vapor emanating from residual liquid at $z = z^*$ left after the passage of the previous wetting front. Not until a later time $t = 2\lambda_c / c_r$, after the residual liquid has been consumed at the location of the first wetting front, will a new wetting front be established on the heater surface. Wetting is, therefore, skipped every other cycle and wetting fronts are separated by $2\lambda_c$ wavelengths.

Surface Energy Balance at CHF

A Lagrangian frame of reference is used to model heat transfer to the moving wetting fronts illustrated in Fig. 5. Equation (1) sums the transient energy removed from the heater by the passage of all wetting fronts in contact with the heater between the time a wetting front first forms on the heater surface and the time the next wetting front is established at the same location. Equation (1) also accounts for the steady heat removal from the continuous wetting zone, $0 < z < z^*$.

$$q_m = \frac{c_r / (2\lambda_c)}{L - z^*} \left[\int_0^{\tau} \int_{z^*}^{L} q_{s,1}\, dz\, dt + \cdots + \int_0^{\tau} \int_{z^*}^{L} q_{s,n}\, dz\, dt \right], \qquad (1)$$

where $q_{s,1}, q_{s,2}, \ldots, q_{s,n}$ are the local heat fluxes corresponding to wetting fronts 1, 2, . . , n, respectively. Where a wetting front is present, q_s is equal to some localized heat flux value, q_l, otherwise q_s is essentially zero where the heater surface is dry.

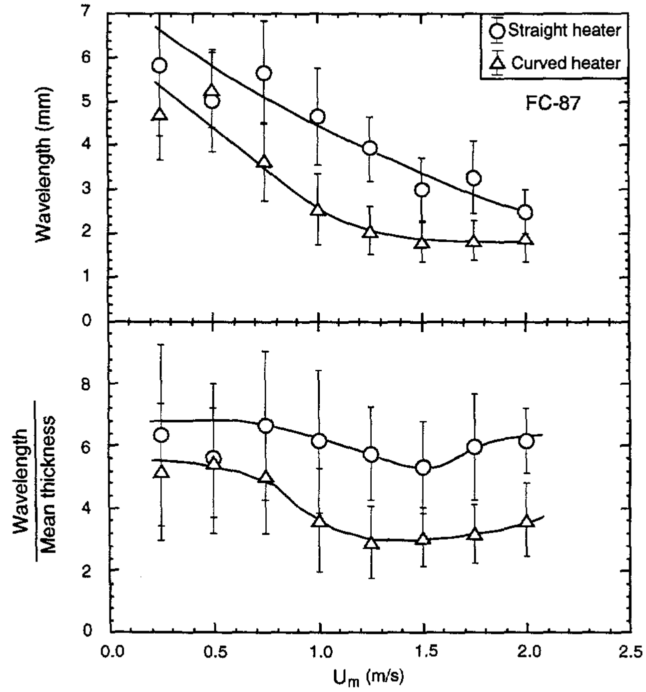

Figure 4. Vapor Layer Wavelength and Ratio of Wavelength to Mean Thickness Just Prior to CHF

The photographic study and data base revealed the span (length) of each wetting front was one-fourth the separation distance between wetting fronts; *i.e.*, CHF is about one-fourth the heat flux concentrated in the wetting fronts. A surface energy balance detailed by Galloway and Mudawar [14] reduces equation (1) to the following expression for CHF:

$$q_m = \left[1 - \frac{\lambda_c}{16\left(L - z^*\right)}\right]\frac{q_l}{4}, \tag{2}$$

where the coefficient in the brackets is close to unity for most operating conditions and accounts for continuous wetting in the region $0 < z < z^*$ and any partial wetting fronts in the downstream region, and q_l is the heat flux required to cause lifting of the most upstream wetting front.

CHF Trigger Mechanism: Lift-off Criterion

The lift-off heat flux will develop when the normal momentum of vapor generated in the wetting front just exceeds the pressure force exerted upon the interface as a result of interfacial curvature.

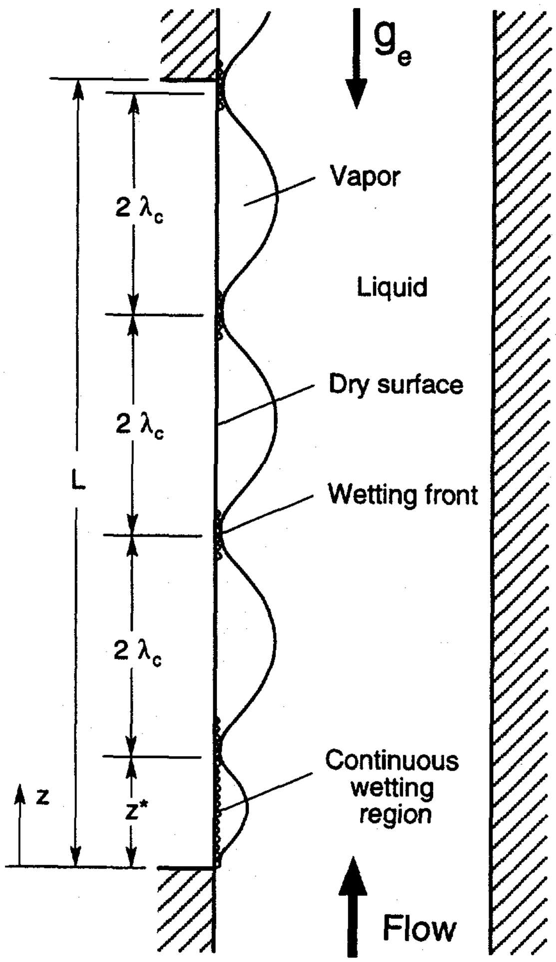

Figure 5. Wetting Front Propagation along a Vertical Surface

$$\rho_g \left[\frac{q_l}{\rho_g\, h_{fg}\left(1 + \dfrac{c_{p,f}\,\Delta T_{\mathrm{sub}}}{h_{fg}}\right)} \right]^2 = \overline{P_f - P_g}\,, \tag{3}$$

where the average pressure difference across the interface, $\overline{P_f - P_g}$, is calculated by integrating the pressure difference over the span of the most upstream wetting front.

Combining equations (2) and (3) yields an expression for CHF which is applicable to both straight and curved heaters.

$$q_m = \frac{1}{4}\,\rho_g\, h_{fg}\left(1 - \frac{\lambda_c}{16\left(L - z^*\right)}\right)\left(1 + \frac{c_{p,f}\,\Delta T_{\mathrm{sub}}}{h_{fg}}\right)\left[\frac{\overline{P_f - P_g}}{\rho_g}\right]^{1/2}. \tag{4}$$

Equation (4) shows predicting CHF requires estimation of $\overline{P_f - P_g}$. The next section will discuss an instability model which will be used to predict this key parameter for both straight and curved heaters.

The lift-off criterion alone can explain why, in flow boiling, CHF is greater for the curved, concave heater than the straight heater. For an assumed sinusoidal wave with wavelength λ and amplitude η_0, curvature at the wave peak is proportional to $(\eta_0 / \lambda)^2 / \eta_0$. Although the straight and curved heaters produced waves with fairly equal amplitudes, Fig. 4 indicates the waves acquired greater curvature over the curved heater than they did over the straight heater. This increased curvature resulted in a greater pressure force exerted upon the interface and, consequently, increases both the lift-off heat flux in the wetting fronts and CHF relative to the straight heater. As will be shown later, the curved heater produced an average enhancement of 23% compared to the straight heater.

Interfacial Instability of Vapor Layer

The interfacial waviness illustrated in Fig. 5 can be idealized as a hydrodynamic instability of an interface between a vapor layer of velocity $\bar{u}_{g,m}$ and height H_g and a liquid layer of velocity $\bar{u}_{f,m}$ and height H_f. Using classical instability theories [24, 25], the interfacial pressure difference resulting from a sinusoidal disturbance of the form $\eta(z,t) = \eta_0\, e^{ik(z-ct)}$ perpendicular to the unperturbed interface can be expressed as [14]

$$P_f - P_g = -\,\eta\, k\left[\rho_f''\left(c - \bar{u}_{f,m}\right)^2 + \rho_g''\left(\bar{u}_{g,m} - c\right)^2\right] - \left(\rho_f - \rho_g\right) g_n\, \eta = -\,\sigma k^2\, \eta\,, \tag{5}$$

where g_n is the body force per unit mass perpendicular to the unperturbed interface ($g_n = 0$ for vertical upflow over a straight heater), and the modified density terms for a straight channel are expressed as [14]

$$\rho_f'' = \rho_f \coth\left(k\, H_f\right), \tag{6a}$$

$$\rho_g'' = \rho_g \coth\left(k\, H_g\right). \tag{6b}$$

Solving equation (5) yields the following equation for *c*:

$$c=\frac{\rho_g''\bar{u}_{g,m}+\rho_f''\bar{u}_{f,m}}{\left(\rho_g''+\rho_f''\right)}\pm\sqrt{\frac{\sigma k}{\left(\rho_g''+\rho_f''\right)}-\frac{g_n\left(\rho_f-\rho_g\right)}{k\left(\rho_g''+\rho_f''\right)}-\frac{\rho_g''\rho_f''\left(\bar{u}_{g,m}-\bar{u}_{f,m}\right)^2}{\left(\rho_g''+\rho_f''\right)^2}}\ . \tag{7}$$

The critical wavelength is defined as the wavelength that produces a neutrally stable wave. This wavelength can be calculated by setting the argument of *c* in equation (7) equal to zero.

$$\frac{2\pi}{\lambda_c}=k_c=\frac{\rho_f''\rho_g''\left(\bar{u}_{g,m}-\bar{u}_{f,m}\right)^2}{2\sigma\left(\rho_f''+\rho_g''\right)}+\sqrt{\left[\frac{\rho_f''\rho_g''\left(\bar{u}_{g,m}-\bar{u}_{f,m}\right)^2}{2\sigma\left(\rho_f''+\rho_g''\right)}\right]^2+\frac{g_n\left(\rho_f-\rho_g\right)}{\sigma}}\ . \tag{8}$$

This classical hydrodynamic instability model is not applicable to curved flow. Recently, Galloway and Mudawar [26] developed a new model for hydrodynamic instability along a curved interface. Interestingly, the above instability model was proven equally valid for curved flow, provided the liquid and vapor velocities in equations (5), (7) and (8) are calculated along the interface, and the modified density terms are replaced by the following:

$$\rho_f'''=\rho_f\left[\frac{\left(\dfrac{R_0}{R_1}\right)^{2kR_0}+1}{\left(\dfrac{R_0}{R_1}\right)^{2kR_0}-1}\right], \tag{9a}$$

$$\rho_g'''=\rho_g\left[\frac{\left(\dfrac{R_0}{R_2}\right)^{2kR_0}+1}{1-\left(\dfrac{R_0}{R_2}\right)^{2kR_0}}\right]. \tag{9b}$$

CHF Model Predictions for Straight and Curved Flow Boiling

A separated flow model given by Galloway and Mudawar [14, 26] was employed to predict local mean values of vapor layer thickness and velocities of the liquid and vapor layers in terms of inlet velocity, subcooling, and heat flux. These local values are required in order to predict the interfacial wavelength and $\overline{P_f-P_g}$.

Figure 6 shows the CHF model predicts the experimental data for the straight and the curved heaters with mean absolute errors of 7% and 14%, respectively. The accuracy of the model predictions is proof of the validity of assumptions used in constructing the surface energy balance and of the lift-off criterion. The CHF enhancement obtained with the curved heater over the straight heater is a direct consequence of the increased curvature of the individual interfacial waves causing an increase in the net pressure force exerted upon the interface in the wetting fronts.

As for the limitations of the present model, several conditions exist for which the assumptions used may not be valid. They include (a) near-critical pressure, (b) highly subcooled flow, where the vapor layer development may be strongly influenced by condensation along the vapor-liquid interface, (c) high inlet velocities corresponding to $g_n = U_m^2 / R_2 > 10\, g_e$, where vapor slugs begin to detach from peaks in the wavy vapor-liquid interface, and (d) long heaters. A recent study by two of the authors [15, 16] explored the stream-wise changes in the interfacial features at CHF over long heaters. The vapor waves between wetting fronts maintained equal wavelengths over an axial distance close to the length of the heaters used in the present study, but were found to grow downstream due to merging of adjacent waves. This behavior increased the distance between wetting fronts resulting in smaller CHF for long heaters as compared to heaters close in size to the one used in the present study. These findings, while determined from straight heater experiments, clearly indicate the present model should not be applied in its present form to long straight or curved heaters.

5. THEORETICAL MODEL FOR POOL BOILING CHF FROM A VERTICAL SURFACE

Growth of Vapor Layer

Figure 7 shows pool boiling data for water for orientations ranging from horizontal ($\theta = 0$ degrees) to vertical (90 degrees), compared with predictions of the model by Zuber *et al.* [1], modified by replacing g_e by $g_e \cos\theta$. CHF decreases with increasing angle of orientation following, to some degree, the predicted trend. However, while the model predicts zero CHF for the vertical orientation, the data show an increase in CHF between 75 and 90 degrees. Obviously, the mechanism proposed by Zuber *et al.* is not suitable for near-vertical orientations.

In pool boiling on a vertical surface, the mean velocity of liquid outside the vapor layer is zero. Equations for the mean vapor velocity, $\bar{u}_{g,m}$, and vapor layer thickness, δ, can be derived by applying mass, momentum, and energy conservation for a control volume of the vapor layer of length Δz. Combining both mass and energy conservation for this control volume and integrating with respect to z gives

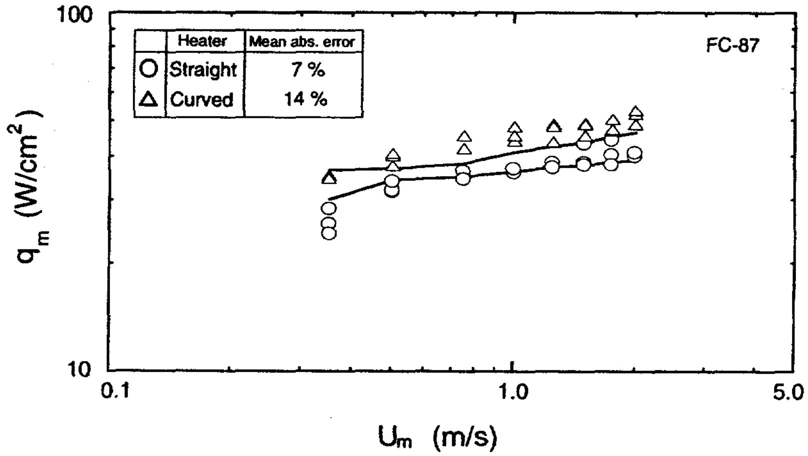

Figure 6. Comparison of Model Predictions and Flow Boiling CHF Data for Straight and Curved Heaters

$$\rho_g \bar{u}_{g,m}\,\delta = \frac{q_m z}{h_{fg}\left[1+\dfrac{c_{p,f}\Delta T_{\text{sub}}}{h_{fg}}\right]} \; . \tag{10}$$

A momentum balance on the same control volume yields

$$\frac{d}{dz}\left[\rho_g \bar{u}^{2}_{g,m}\,\delta\right] = \left(\rho_f - \rho_g\right) g_e\,\delta \, . \tag{11}$$

Combining equations (10) and (11) gives a differential equation relating $\bar{u}_{g,m}$ to z. The solution for this equation is

$$\bar{u}_{g,m} = \left[\frac{2}{3}\left(\frac{\rho_f - \rho_g}{\rho_g}\right) g_e\, z\right]^{1/2} \; . \tag{12}$$

Substituting for $\bar{u}_{g,m}$ using equation (12) in equation (10) gives the variation of δ with z.

$$\delta = \frac{q_m}{\rho_g h_{fg}\left[1+\dfrac{c_{p,f}\Delta T_{\text{sub}}}{h_{fg}}\right]} \left[\frac{2}{3}\left(\frac{\rho_f - \rho_g}{\rho_g}\right) g_e\right]^{-1/2} \sqrt{z} \; . \tag{13}$$

The critical wavelength corresponding to the onset of instability can be derived from equation (8) by setting g_n and $\bar{u}_{f,m}$ equal to zero; further simplification is also possible because, for the conditions of the pool boiling study, $\rho_g'' \cong \rho_g$.

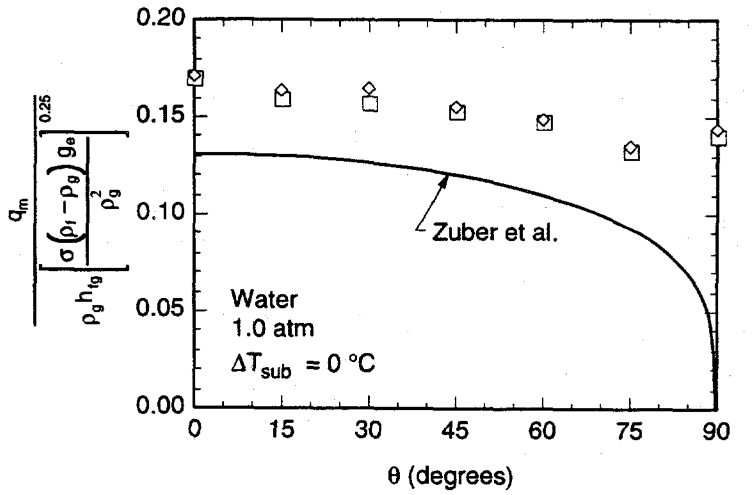

Figure 7. Comparison of Pool Boiling CHF Data for Different Orientations with Predictions of the Modified Model by Zuber *et al.* [1]

$$\lambda_c = \frac{2\pi}{k_c} = \frac{2\pi\sigma\left(\rho_f + \rho_g\right)}{\rho_f \rho_g \bar{u}_{g,m}^2} . \tag{14}$$

The mean interfacial pressure force over the wetting front for a sinusoidal wave with $k = 2\pi / (2\lambda_c)$ becomes

$$\overline{P_f - P_g} = 2\sqrt{2}\,\pi \frac{\sigma\delta}{\lambda_c^2} . \tag{15}$$

Substituting the above expression in equation (4), neglecting the coefficient due to the upstream continuous wetting zone and the downstream partial wetting front, gives

$$q_m = \frac{1}{4}\rho_g h_{fg}\left[1 + \frac{c_{p,f}\Delta T_{\text{sub}}}{h_{fg}}\right]\left[\left(2\sqrt{2}\,\pi\right)\frac{\sigma\delta}{\rho_g \lambda_c^2}\right]^{1/2} . \tag{16}$$

Since the first wetting front is centered at $z = \lambda_c$, the critical wavelength, equation (14), can be expressed in terms of $\bar{u}_{g,m}$, equation (12), corresponding to $z = \lambda_c$. This gives

$$\lambda_c = \left[3\pi\left(\frac{\rho_f + \rho_g}{\rho_f - \rho_g}\right)\frac{\sigma}{\rho_f g_e}\right]^{1/2} . \tag{17}$$

Substituting the expressions for δ (based on $z = \lambda_c$), equation (13), and λ_c, equation (17), in equation (16) yields the following CHF relation

$$q_m = \frac{1}{8}\left(\frac{\pi}{3}\right)^{1/4}\left[1 + \frac{c_{p,f}\Delta T_{\text{sub}}}{h_{fg}}\right]\left[\frac{\rho_f}{\rho_f + \rho_g}\right]^{3/4}\rho_g h_{fg}\left[\frac{\sigma\left(\rho_f - \rho_g\right)g_e}{\rho_g^2}\right]^{1/4} . \tag{18}$$

The above equation can be further simplified for saturated conditions, and pressures much smaller than critical to

$$q_m = 0.126\,\rho_g h_{fg}\left[\frac{\sigma\left(\rho_f - \rho_g\right)g_e}{\rho_g^2}\right]^{1/4} . \tag{19}$$

Interestingly, equation (19) is identical in form to the model by Zuber *et al.* [1], although the mechanisms proposed in the individual models are distinctly different. Also, while the model by Zuber *et al.* predicts zero CHF for vertical surfaces, the present model, as shown in Fig. 7, predicts a CHF value for the same orientation only 11% smaller than the data.

6. CONCLUSIONS

Experiments involving pool and flow boiling from vertical surfaces were performed to ascertain the CHF trigger mechanism for each. The flow boiling experiments included both straight and curved surfaces. Key conclusions from the study are as follows:

(1) A fairly continuous wavy vapor layer engulfs the heater surface at heat fluxes smaller than CHF in both pool and flow boiling. Boiling remains active in wetting fronts, where the interface of the vapor layer contacts the heater surface. CHF is triggered when the normal momentum of the vapor produced in the wetting front exceeds the pressure force exerted upon the interface due to interfacial curvature.

(2) A CHF model constructed from these observations predicts flow boiling CHF data for the straight and curved heaters with mean absolute errors of 7% and 14%, respectively.

(3) In flow boiling, CHF is higher for the curved heater than for the straight heater because of a greater pressure resistance to interfacial separation in the case of the curved heater.

(4) For pool boiling, the present model reduces to an expression identical in form to the model by Zuber *et al.* [1], although the mechanisms proposed in the individual models are distinctly different. However, while the model by Zuber *et al.* predicts zero CHF for vertical surfaces and is therefore unsuitable for vertical surfaces, the present model predicts a CHF value for the same orientation only 11% smaller than the data.

ACKNOWLEDGMENT

The authors are grateful for the support of the Office of Basic Energy Sciences of the U.S. Department of Energy (Grant No. DE-FE02-93ER14394).

NOMENCLATURE

c	wave speed
c_p	specific heat at constant pressure
c_r	real component of wave speed
g_e	Earth gravity
g_n	component of body force per unit mass normal to liquid-vapor interface
H	channel height, $H_f + H_g$, $R_2 - R_1$
H_f	liquid layer thickness
H_g	vapor layer thickness
h_{fg}	latent heat of vaporization
k	wave number, $2\pi/\lambda$
k_c	critical wave number, $2\pi/\lambda_c$
L	heater length
n	number of wetting fronts
P	pressure
$\overline{P_f - P_g}$	mean interfacial pressure difference in wetting front

q_l	heat flux (at CHF) corresponding to wetting front separation (lift-off)
q_m	critical heat flux (CHF)
R_0	radius of unperturbed interface in curved flow
R_1	inner radius of curved channel
R_2	outer radius of curved channel and curved heater surface
t	time
T	temperature
ΔT_{sub}	liquid subcooling
$\bar{u}_m$	mean velocity across liquid or vapor layer
U_m	mean liquid velocity upstream of heater in flow boiling
z	spatial coordinate in the stream-wise direction
z^*	distance from leading edge of heater to center of first wetting front, $z_0 + \lambda_c(z^*)$
z_0	position from leading edge where the liquid and vapor velocities become equal

Greek Symbols

δ	mean vapor layer thickness (= H_g)
η_0	interfacial displacement
η	amplitude of interfacial displacement
θ	surface angle of orientation
λ	wavelength of interfacial perturbation
λ_c	critical wavelength corresponding to onset of instability
ρ	density
ρ''	modified density defined in equations (6a) and (6b)
ρ'''	modified density defined in equations (9a) and (9b)
σ	surface tension
τ	wetting period

Subscripts

f	saturated liquid
g	saturated vapor
m	mean
sub	subcooling

REFERENCES

1. N. ZUBER, M. TRIBUS and J. M. WESTWATER, "The Hydrodynamic Crisis in Pool Boiling of Saturated and Subcooled Liquid," *International Developments in Heat Transfer*, Boulder, CO, Part II, 230-236 (1961).

2. S. S. KUTATELADZE and A. I. LEONT'EV, "Some Applications of the Asymptotic Theory of the Turbulent Boundary Layer," *Proc. 3rd Int. Heat Transfer Conf.*, Chicago, IL, Vol. 3, pp. 1-6 (1966).

3. L. S. TONG, "Boundary-Layer Analysis of the Flow Boiling Crisis," *Int. J. Heat Mass Transfer* 11, 1208-1211 (1968).

4. L. S. TONG, "A Phenomenological Study of Critical Heat Flux," ASME Paper 75-HT-68 (1975).

5. J. H. LIENHARD and R. EICHHORN, "Peak Boiling Heat Flux on Cylinders in a Cross Flow," *Int. J. Heat Mass Transfer* 19, 1135-1142 (1976).

6. J. H. LIENHARD and M. M. HASAN, "On Predicting Boiling Burnout with the Mechanical Energy Stability Criterion," *ASME J. Heat Transfer* 101, 276-279 (1979).

7. G. J. KIRBY, R. STANIFORTH and J. H. KINNEIR, "A Visual Study of Forced Convection Boiling Part 2: Flow Patterns and Burnout for a Round Test Section," Report AEEW-R 506, United Kingdom Atomic Energy Authority, Atomic Energy Establishment, Winfrith, England (1967).

8. W. HEBEL, W. DETAVERNIER and M. DECRETON, "A Contribution to the Hydrodynamics of Boiling Crisis in a Forced Flow of Water," *Nucl. Engng Des.* 64, 433-445 (1981).

9. J. WEISMAN and B. S. PEI, "Prediction of Critical Heat Flux in Flow Boiling at Low Qualities," *Int. J. Heat Mass Transfer* 26, 1463-1477 (1983).

10. C. H. LEE and I. MUDAWAR, "A Mechanistic Critical Heat Flux Model for Subcooled Flow Boiling based on Local Bulk Flow Conditions," *Int. J. Multiphase Flow* 14, 711-728 (1988).

11. Y. KATTO, "A Physical Approach to Critical Heat Flux of Subcooled Flow Boiling in Round Tubes," *Int. J. Heat Mass Transfer* 33, 611-620 (1990).

12. Y. KATTO, "Prediction of Critical Heat Flux of Subcooled Flow Boiling in Round Tubes," *Int. J. Heat Mass Transfer* 33, 1921-1928 (1990).

13. J. E. GALLOWAY and I. MUDAWAR, "CHF Mechanism in Flow Boiling from a Short Heated Wall - Part 1. Examination of Near-Wall Conditions with the aid of Photomicrography and High-Speed Video Imaging," *Int. J. Heat Mass Transfer* 36, 2511-2526 (1993).

14. J. E. GALLOWAY and I. MUDAWAR, "CHF Mechanism in Flow Boiling from a Short Heated Wall - Part 2. Theoretical CHF Model," *Int. J. Heat and Mass Transfer* 36, 2527-2540 (1993).

15. C. O. GERSEY and I. MUDAWAR, "Effects of Heater Length and Orientation on the Trigger Mechanism for Near-Saturated Flow Boiling CHF - Part 1. Photographic and Statistical Characterization of the Near-Wall Interfacial Features," *Int. J. Heat Mass Transfer* 38, 629-642 (1995).

16. C. O. GERSEY and I. MUDAWAR, "Effects of Heater Length and Orientation on the Trigger Mechanism for Near-Saturated Flow Boiling CHF - Part 2. CHF Model," *Int. J. Heat Mass Transfer* 38, 643-654 (1995).

17. W. R. GAMBILL and N. D. GREENE, "Boiling Burnout with Water in Vortex Flow," *Chem. Engng Prog.* 54(10), 68-76 (1958).

18. Z. L. MIROPOL'SKIY and V. Y. PIKUS, "Critical Boiling Heat Fluxes in Curved Channels," *Heat Transfer-Soviet Research* 1, 74-79 (1969).

19. T. G. HUGHES and D. R. OLSON, "Critical Heat Fluxes for Curved Surface during Subcooled Flow Boiling," *Trans. Canadian Soc. Mech. Eng.* 3, 122-130 (1975).

20. J. E. GALLOWAY and I. MUDAWAR, "Critical Heat Flux Enhancement by means of Liquid Subcooling and Centrifugal Force Induced by Flow Curvature," *Int. J. Heat Mass Transfer* 35, 1247-1260 (1992).

21. M. P. FIORI and A. E. BERGLES, "Model of Critical Heat Flux in Subcooled Flow Boiling," *Proc. 4th Int. Heat Transfer Conf.*, Versailles, France, Vol. 6, pp. 354-355 (1970).

22. R. HINO and T. UEDA, "Studies on Heat Transfer and Flow Characteristics in Subcooled Flow Boiling-Part 1. Boiling Characteristics," *Int. J. Multiphase Flow* 11, 269-281 (1985).

23. R. HINO and T. UEDA, "Studies on Heat Transfer and Flow Characteristics in Subcooled Flow Boiling-Part 2. Flow Characteristics," *Int. J. Multiphase Flow* 11, 283-297 (1985).

24. H. LAMB, *Hydrodynamics* (6th Edn), p. 371. Dover Publications, New York (1945).

25. L. M. MILNE-THOMPSON, *Theoretical Hydrodynamics* (4th Edn), p. 409. Macmillan, New York (1960).

26. J. E. GALLOWAY and I. MUDAWAR, "A Theoretical Model for Flow Boiling CHF from Short Concave Heaters," *ASME J. Heat Transfer*, in press.

SHORT-PULSE LASER INTERACTIONS WITH DISORDERED MATERIALS AND LIQUIDS

Leslie M. Phinney, Cynthia H. Goldman, Jon P. Longtin, and Chang-Lin Tien

Department of Mechanical Engineering
University of California at Berkeley
Berkeley, California 94720

ABSTRACT

High-power, short-pulse lasers in the picosecond and subpicosecond range are utilized in an increasing number of technologies, including materials processing and diagnostics, micro-electronics and devices, and medicine. In these applications, the short-pulse radiation interacts with a wide range of media encompassing disordered materials and liquids. Examples of disordered materials include porous media, polymers, organic tissues, and amorphous forms of silicon, silicon nitride, and silicon dioxide. In order to accurately model, efficiently control, and optimize short-pulse, laser-material interactions, a thorough understanding of the energy transport mechanisms is necessary. Thus, fractals and percolation theory are used to analyze the anomalous diffusion regime in random media. In liquids, the thermal aspects of saturable and multiphoton absorption are examined. Finally, a novel application of short-pulse laser radiation to reduce surface adhesion forces in microstructures through short-pulse laser-induced water desorption is presented.

INTRODUCTION

Since their invention thirty years ago, lasers have altered the direction and rate of the development of science and technology. Laser applications have fundamentally influenced modern technology in the areas of measurement, materials, manufacturing, information, and communication [1]. Short-pulse lasers are being applied to materials processing and diagnostics, electronic device fabrication and maintenance, and medical procedures. In these varied applications, short-pulse laser radiation interacts with a multitude of different materials, including, but not limited to, metals, semiconductors, polymers, porous media, liquids, and biological tissue.

Examples of short-pulse laser applications in materials processing and diagnostics include annealing of radiation damage in ion-implanted semiconductors, recrystallization of amorphous (noncrystalline) and polycrystalline silicon, rapid thermal cleaning, deposition of thin films, creation of metastable alloys, and thin-film and atomic-level diagnostics [2]. The increased temporal resolution of optical observations in diagnostics allows detailed "stop action" observations of previously inaccessible phenomena. In addition, the ultrashort laser-material interaction time permits highly localized observation and processing due to the short-range of diffusion during the interaction time.

In these applications, laser interactions with random media such as amorphous materials, porous media, and composites are often required. Amorphous forms of materials such as silicon dioxide, silicon nitride, and silicon are widely used in microelectronics and micro-sensor/actuator fabrication. Many nanostructured and metastable materials formed by laser processing are also amorphous [3]. Also, porous silicon, porous metal "black" coatings, polymers, and composites are becoming increasingly important. Nanosecond and picosecond laser pulses have also been used to ablate atherosclerotic tissue [4], a biological tissue which is random in nature.

Additionally, the interaction of high-power, pulsed laser radiation with liquids is fundamental to applications in many contemporary technologies, including ophthalmic microsurgery and gall-stone fragmentation [5], laser-induced desorption of thin films [6], laser particle removal [7], photothermal spectroscopy, and laser pulse generation and modification [8,9]. The liquid phase is also present in both laser melting and vaporization processes. Moisture induced device failure is a significant and persistent problem in the microelectronics industry [10,11], with incomplete moisture removal from electronic devices being a cause of leakage current, oxidation, and contamination [11]. Microelectromechanical systems are also subject to liquid related problems during fabrication and operation. Sticking and the accompanying high static friction between a tiny movable part and an underlying substrate, termed *stiction*, is a major problem for microstructures and is mainly due to capillary forces from residual water [12,13].

In laser-assisted processes and laser design, temperature control is a major consideration necessitating the accurate characterization and modeling of energy transport during laser-material interactions. As the pulse width of lasers used in many applications has decreased into the picosecond and subpicosecond range, the applicability of conventional models of energy transport is questionable [1,14]. Short-pulse laser heating of metals has been recently researched for both single- and multi-layer metal films [15,16,17], but the interaction between short-pulse laser radiation and random media or liquids is not fully understood and will be discussed in this paper. An application of short-pulse laser radiation to reduce the surface adhesion of silicon microstructures is also presented.

TRANSPORT IN AMORPHOUS AND NANOSTRUCTURED MATERIALS

In short time-scale applications involving random media, a regime of anomalous diffusion is observed, where the thermal diffusivity is time dependent. In this anomalous regime, transport is slowed compared to that which occurs during normal diffusion. Fournier and Boccara [18] observed anomalous diffusion in an assembly of weakly-bonded, copper spheres (~ 100 μm in diameter) heated by a short-pulse (~ 1 ns) laser. By measuring the transient surface temperature, they were able to distinguish the anomalous diffusion region from those in which normal diffusion occurred. Gefen et al. [19] predicted that anomalous diffusion will have an important effect on the AC electrical conductivity of a percolating network in high frequency (short time-scale) applications. Similarly, Goldman et al. [20] predicted that anomalous diffusion will have a significant effect on thermal transport in amorphous materials on short time scales such as short-pulse laser-material interactions.

The range and impact of anomalous diffusion in transient thermal transport in random media was studied using fractals and percolation theory. A fractal is a shape that is made up of parts similar to the whole in some way [21]. A percolation network is characterized by its correlation length, ξ, a length scale below which the network exhibits fractal behavior and above which it appears homogeneous. Figure 1 shows the temporal behavior of surface temperature of a random medium heated by an instantaneous plane source. Three distinct regimes are present. In the first regime, the heat is absorbed by the basic unit of the percolating network which is Euclidean, so the temperature follows that predicted for normal diffusion. An example of a basic unit of a percolating network is a porous silica particle in a silica aerogel [22,23]. Next, the energy is transmitted from one site to another in the fractal cluster and diffusion is anomalous. Finally, the energy carriers have traveled a distance greater than the correlation length in the material, the material appears homogeneous, and diffusion is once again normal.

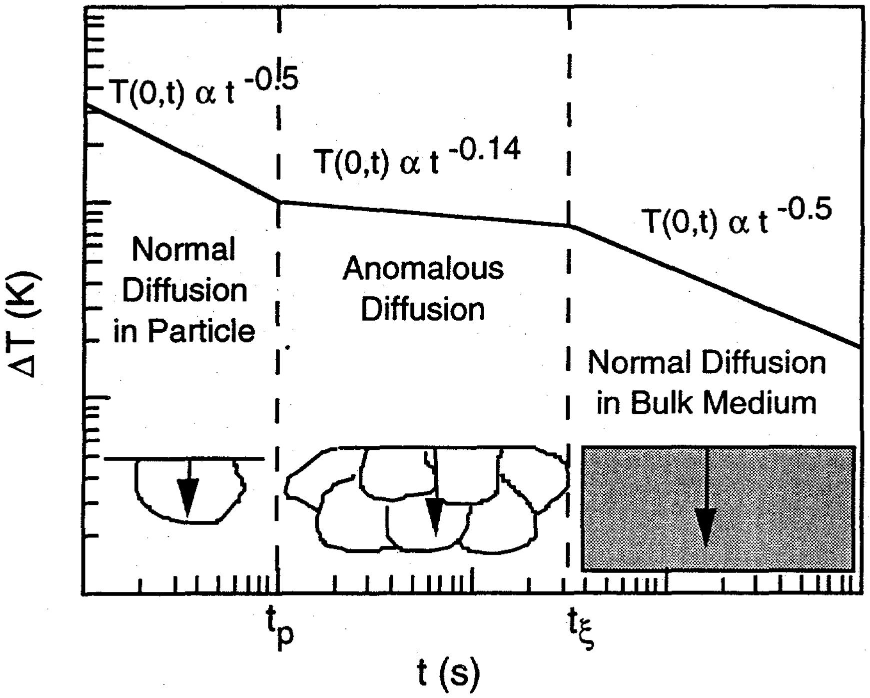

Figure 1. Regimes of Diffusion in Random Media [24]

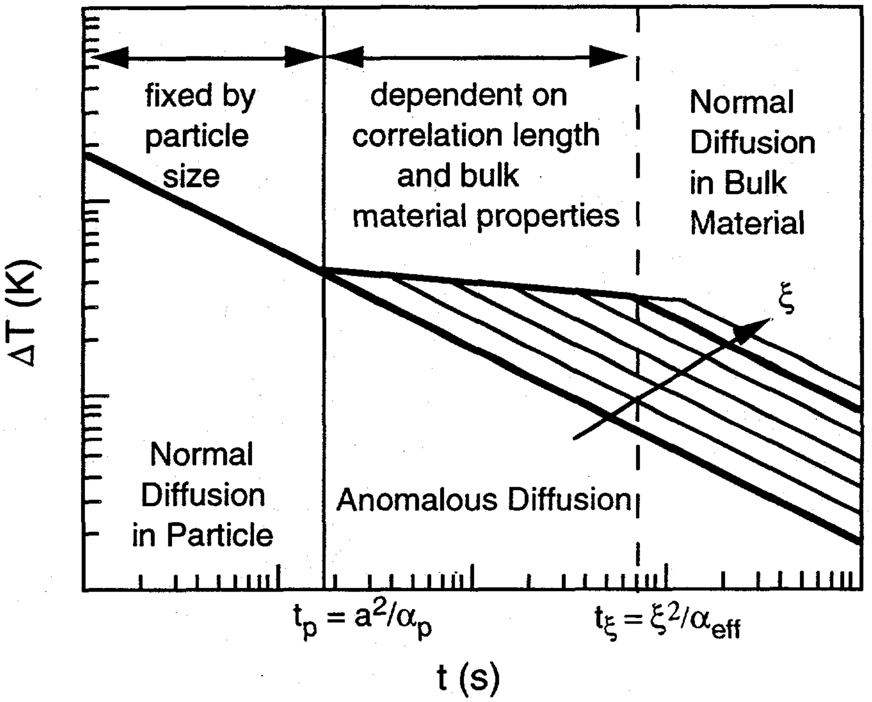

Figure 2. Scaling of Anomalous Diffusion Regime [24]

The impact of anomalous diffusion can be determined by considering the characteristic time and length-scales of heating and other transport mechanisms relative to the time and length-scales of anomalous diffusion[24]. Anomalous diffusion is expected to occur when the length-scale of transport is on the order of the correlation length. The characteristic crossover times, t_p and t_ξ, depend on the particle size, a, and correlation length, ξ, respectively, as well as the diffusivities, α_p and α_{eff}. Figure 2 illustrates the dependence of the anomalous diffusion regimes on particle size, correlation length, and diffusivity of the particle or random medium.

SHORT-PULSE, HIGH-INTENSITY LASER-LIQUID INTERACTIONS

When exposed to laser irradiation, liquid molecules absorb photons and transition to excited states, which usually have different absorption characteristics than the initial (ground) state. After a characteristic relaxation time, τ_p, $\sim 10^{-12}$-10^{-10} s, the molecule will relax back to the ground state. At low intensities, relaxation occurs fast enough to keep the majority of the molecules in the ground state; the absorption is then linear, obeying an exponential decay with distance into the liquid (Beer's law). At high laser intensities, however, enough molecules can be promoted to excited states to alter the bulk transmission and heating effects [25]. This is called *saturable absorption,* and occurs in both pure liquids and solutions, including organic dyes, alcohols, and water. In Figure 3, plots of the temperature rise as a function of distance x into a common saturable absorber (Eastman dye # 9470) are shown. One-hundred 35 ps laser pulses with wavelength of 1064 nm and pulse energy of 70 mJ pass through a 1 cm dye cell. The dye concentration is $8.1 \cdot 10^{-6}$ mol/liter in a 1,2 dichloroethane solvent. The threshold intensity I_s represents the onset of saturation, and the intensity is increased by an order of magnitude in each frame. The dashed lines are classical, low-intensity model results; the solid lines represent the microscopic model. The deviation from low-intensity models (Beer's law) is seen to be very significant at high intensities.

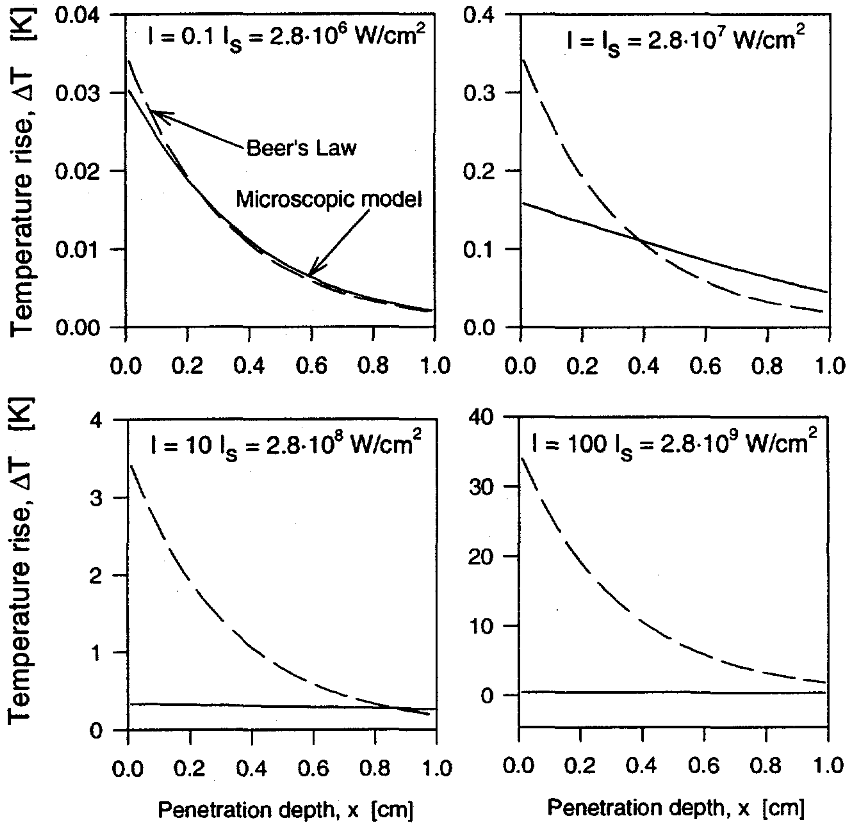

Figure 3. Intensity-dependent temperature during saturable absorption [25]

At even higher intensities the molecule can absorb enough photons to either ionize, which removes an electron completely, or dissociate into simpler constituent products. This process, called *multiphoton absorption and photolysis*, results in a combination of free electrons, ionized cations, and dissociation products that can interact strongly with the incident laser pulse, strongly altering the absorption and heating properties of the liquid [26]. Figure 4 shows the temperature profiles in 1 cm of water irradiated by a combination of 532 nm and 266 nm laser pulses of 1 ns duration at intensities of $1 \cdot 10^9$ and $1 \cdot 10^{10}$ W/cm^2. For the high-intensity pulse, the temperature rise varies over one to two orders of magnitude from the front to the back of the liquid. The total temperature rise due to the 266 nm and 532 nm laser pulses can exceed 40 K, which is three to four orders of magnitude greater than that predicted by classical models [26]. Also, the temperature rise is a strong function of intensity, thus precise control of heating in the liquid can be accomplished by varying the intensity.

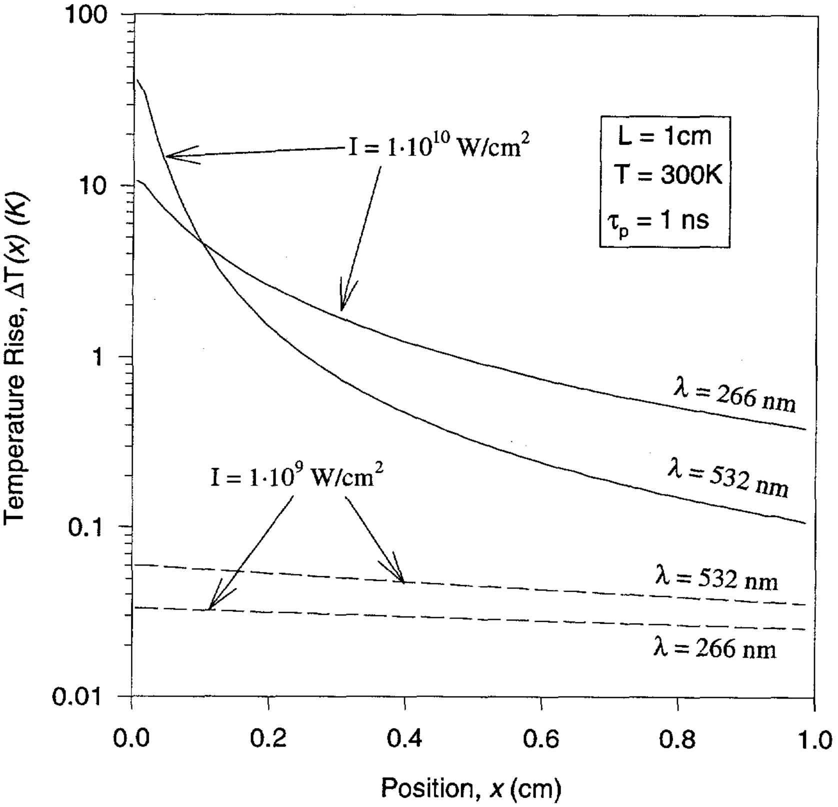

Figure 4. Temperature profiles in water during multiphoton absorption [26]

REDUCTION OF STICTION USING SHORT-PULSE LASER RADIATION

Stiction, the high surface adhesion between microelectromechanical surfaces, is often the result of forces from capillary liquids during the microdevice release process. Residual water molecules can be present underneath the silicon microstructures stuck on the underlying substrate. The desorption of trapped liquid molecules should reduce the adhesion force on the structures. Desorption induced by ultrashort-pulse laser radiation for metals and resulting electronic excitations was first reported by Prybyla et al. [27]. After irradiating a Pd surface with 200 femtoseconds (fs), 620 nm laser pulses, they measured the desorption rate of NO molecules from the Pd surface and showed that the total desorption yield varies superlinearly with the absorbed laser fluence. Since the desorption yield is proportional to the fluence at pulse durations longer than nanoseconds [28], a desorption mechanism other than thermal desorption due to lattice vibrations was involved. The role of the extremely high electron temperature was later confirmed by Prybyla et al. [29], and a model of desorption yield was proposed by Kao et al. [30].

Calculations for silicon microstructures (~ 2 μm thick) irradiated by short-pulse lasers (< 5 ps) indicate that high electron temperatures would exist at short times at both the front and rear surfaces (where the front surface is the surface irradiated by the laser) [31]. At the same time, the lattice temperature does not significantly increase. Therefore, the possibility for short-pulse laser-induced water desorption and a subsequent reduction in stiction is possible. If the adhesion force is reduced below the value of the restoring force of the microstructures, structures stuck to underlying surfaces will be freed as shown in the schematic in Figure 5.

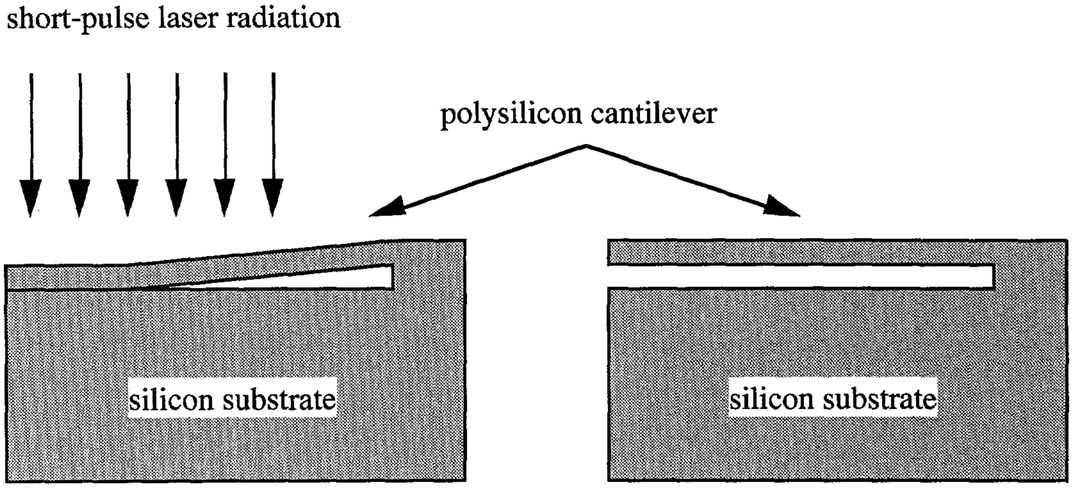

Figure 5. Schematic of the Stiction Reduction Experiment

Experiments to determine the feasibility of using short-pulse laser radiation to reduce the surface adhesion in silicon microstructures were conducted using a 790-nm-wavelength Ti:Sapphire laser [32]. The pulse duration and repetition rate were 150 fs and 1 kHz, respectively. The laser fluence had maximum value of 17 mJ/cm^2. A stiction test structure consisting of cantilevers ranging in length from 60 μm to 1 mm at 20 μm increments was fabricated on an undoped polysilicon substrate. All of the cantilevers have same width (5 μm) and thickness (2 μm), and the free separation between a cantilever and the substrate is 1.5 μm. After the drying process, cantilevers longer than 100 μm on the test structure were stuck to the substrate. An image of the test structure after five seconds of irradiation by the laser beam showed the release of two cantilevers of length 100 μm and 120 μm from the substrate due to the ultrashort-pulse laser irradiation. Thus, the experiments indicated the feasibility of using short-pulse laser radiation to reduce stiction by the possible mechanism of water desorption induced by electronic excitations.

CONCLUSIONS

Short-pulse laser-material interactions are examined for disordered or random materials. Using fractals and percolation theory, an analysis of short time-scale energy transport in random media delineates three regimes of heat transport. The three regimes correspond to transport over the basic percolation unit (particle), the fractal cluster, and the homogeneous medium. Scaling shows that the anomalous diffusion regime is bounded by characteristic times depending on the material properties and structure.

In high-power, laser-liquid interactions, the saturable and multiphoton absorption mechanisms of energy deposition are investigated. Saturable absorption occurs when a sufficient number of molecules have been promoted to excited states by incoming laser radiation, thus affecting bulk transmission and absorption. In multiphoton absorption and photolysis, molecules absorb a sufficient number of photons to ionize or dissociate. This results in a combination of free electrons, ionized cations, and dissociation products which can interact strongly with the incident laser pulse, altering the absorption and heating properties of the liquid. Temperature profiles calculated considering the effects of saturable absorption or multiphoton absorption and photolysis differ considerably from those predicted by classical heating models.

An application of short-pulse laser radiation is the reduction of surface adhesion in microstructures. Through short-pulse laser-induced desorption of liquid molecules present below a microstructure stuck to an underlying substrate, the adhesion forces on the structures can be reduced and device recovery achieved. This process could be used to both increase device yield during fabrication and extend the operation of microelectromechanical systems.

ACKNOWLEDGEMENT

This work was supported by the U.S. Department of Energy, under grant number DE-FG03-92ER14287.

REFERENCES

1. C. L. TIEN, T. Q. QIU, and P. M. NORRIS, "Microscale Thermal Phenomena in Contemporary Technology," *J. Thermal Science and Engineering* 2, 1 (1994).
2. VON DER LINDE, D., "Ultrashort Interactions in Solids," *Ultrashort Laser Pulses: Generation and Applications,* 2nd ed., W. Kaiser, ed., Springer-Verlag, New York, pp. 113-182 (1993).
3. G. C. HADJIPANYAYIS and R. W. SIEGEL, *Nanophase Materials: Synthesis, Properties, and Applications,* Kluwer Academic Publishers, Boston (1994).
4. A. A. ORAEVSKY, R. O. ESENALIEV, and V. S. LETOKHOV, "Temporal Characteristics and Mechanism of Atherosclerotic Tissue Ablation by Nanosecond and Picosecond Laser Pulses", *Lasers in the Life Sciences* 5, 75 (1992).
5. C. A. SACCHI, "Laser-Induced Electric Breakdown in Water", *J. Optical Society America B* 8, 337 (1991).
6. S. D. ALLEN, J. O. PORTEUS, W. N. FAITH, and J. B. FRANCK, "Contaminant and Defect Analysis of Optical Surfaces by Infrared Laser Induced Desorption", *Appl. Phys. Lett.* 45, 997 (1984).
7. S. J. LEE, K. IMEN, and S. D. ALLEN, "Laser-Assisted Particle Removal from Silicon Surfaces", *Microelectronic Engineering* 20, 145 (1993).
8. Y. B. BAND and B. SCHARF, "Engineering Reverse Saturable Absorbers for Desired Wavelengths", *Chemical Phys. Lett.* 127, 381 (1986).
9. M. STUKE, *Dye Lasers: 25 Years,* Springer-Verlag, Berlin (1992).
10. W. C. SHUMAY, "Corrosion in Electronics", *Advanced Materials and Processes* 132, 73 (1987).
11. C. S. LEECH, "Removing Moisture from Electronic Components and Assemblies", *Circuits Assembly* 5, 34 (1994).
12. R. L. ALLEY, G. J. CUAN, R. T. HOWE, and K. KOMVOPOULOS, "The Effect of Release-Etch Processing on Surface Microstructure Stiction", *Technical Digest, IEEE Solid-State Sensor and Actuator Workshop*, Hilton Head Island, South Carolina, pp. 202 (1992).
13. R. LEGTENBERG, H. A. C. TILMANS, J. ELDERS, and M. ELWENSPOEK, "Stiction of Surface Micromachined Structures after Rinsing and Drying: Model and Investigation of Adhesion Mechanisms", *Sensors and Actuators A* A43, 230 (1994).
14. T. Q. QIU and C. L. TIEN, "Heat Transfer Mechanisms During Short-Pulse Laser Heating of Metals," *J. Heat Transfer* 115, 835 (1993).
15. T. Q. QIU and C. L. TIEN, "Short-Pulse Laser Heating on Metals," *Int. J. Heat Mass Transfer* 35, 719 (1992).

16. T. Q. QIU and C. L. TIEN, "Femtosecond Laser Heating of Multi-Layer Metals–I. Analysis," *Int. J. Heat Mass Transfer* 37, 2789 (1994).
17. T. Q. QIU, T. JUHASZ, C. SUAREZ, W. E. BRON, and C. L. TIEN, "Femtosecond Laser Heating of Multi-Layer Metals–II. Experiments," *Int. J. Heat Mass Transfer* 37, 2799 (1994).
18. D. FOURNIER and A. C. BOCCARA, "Heterogeneous Media and Rough Surfaces: A Fractal Approach for Heat Diffusion Studies," *Physica A* 157, 587 (1989).
19. Y. GEFEN, A. AHARONY, and S. ALEXANDER, "Anomalous Diffusion on Percolating Clusters," *Phys. Rev. Lett.* 50, 77 (1983).
20. C. H. GOLDMAN, P. M. NORRIS, and C. L. TIEN, "Picosecond Energy Transport in Amorphous Materials," *Proceedings of the 1995 ASME/JSME Joint Thermal Engineering Conference* 1, 467 (1995).
21. B. B. MANDELBROT, *Fractals: Form, Chance, and Dimension,* Freeman, San Francisco (1977).
22. K. RICHTER, and C. L. TIEN, "Structure Simulation of Sparse Silica Aerogels," *Fractals* 2, 535 (1994).
23. K. RICHTER, P. M. NORRIS, and C. L. TIEN, "Aerogels: Applications, Structure, and Heat Transfer Phenomena," *Ann. Rev. Heat Transfer* 6, in press (1995).
24. C. H. GOLDMAN and C. L. TIEN, "Anomalous Diffusion in Short-Pulse Laser Interactions with Random Media," to be presented at the 1995 National Heat Transfer Conference, Portland, Oregon, August 5-9, 1995.
25. J. P. LONGTIN and C. L. TIEN, "Saturable Absorption during High-Intensity Laser Heating of Liquids," to be presented at the 1995 International Mechanical Engineering Congress and Exposition, San Francisco, California, November 12-17, 1995.
26. J. P. LONGTIN and C. L. TIEN, "High-Intensity Laser Heating in Liquids: Multiphoton Absorption," to be presented at the 1995 National Heat Transfer Conference, Portland, Oregon, August 5-9, 1995.
27. J. A. PRYBYLA, T. F. HEINZ, J. A. MISEWICH, M. M. T. LOY, and J. H. GLOWNIA, "Desorption Induced by Femtosecond Laser Pulses," *Phys. Rev. Lett.* 64, 1537 (1990).
28. F.-J. KAO, D. G. BUSCH, D. GOMES DA COSTA, and W. HO, "Femtosecond versus Nanosecond Surface Photochemistry: O_2 + CO on Pt(111) at 80 K," *Phys. Rev. Lett.* 70, 4098 (1993).
29. J. A. PRYBYLA, H. W. K. TOM, and G. D. AUMILLER, "Femtosecond Time-Resolved Surface Reaction: Desorption of CO from Cu(111) in < 325 fsec," *Phys. Rev. Lett.* 68, 503 (1992).
30. F.-J. KAO, D. G. BUSCH, D. COHEN, D. GOMES DA COSTA, and W. HO, "Femtosecond Laser Desorption of Molecularly Adsorbed Oxygen from Pt(111)," *Phys. Rev. Lett.* 71, 2094 (1993).
31. K. FUSHINOBU, L. M. PHINNEY, and N. C. TIEN, "Ultrashort-Pulse Laser-Induced Water Desorption from Silicon Surfaces," to be submitted to *Int. J. Heat Mass Transfer* (1995).
32. N. C. TIEN, S. JEONG, K. FUSHINOBU, L. M. PHINNEY, and J. BOKOR, "Reduction of Surface Adhesion in Silicon Microstructures Using Ultrashort-Pulse Laser Irradiation," private communication (1995).

STUDIES ON THE FORMULATION OF THERMODYNAMICS AND STOCHASTIC THEORY FOR SYSTEMS FAR FROM EQUILIBRIUM

John Ross
Department of Chemistry
Stanford University
Stanford, California 94305

ABSTRACT

We have been working for some time on the formulation of thermodynamics and the theory of fluctuations in systems far from equilibrium and progress in several aspects of that development are reported here.

THEORY

The theory is based on the concept of an excess work, ϕ, that is the work necessary for a differential displacement of a system in an arbitrary state, further away from a stationary state, minus the work of the same displacement away from the stationary state (or at a specified reference state). This excess work, ϕ, has the following properties: 1. the excess work, ϕ, provides necessary and sufficient conditions of global stability for systems with one or more stable stationary states. 2. ϕ is the thermodynamic driving force towards the stationary states and is a species-specific affinity. 3. ϕ is a Liapunov function with ϕ in the form of Boltzman's H theorem. 4. ϕ is a measurable excess work attainable from the spontaneous relaxation in a differential displacement along the deterministic trajectory minus the work of that same displacement from the stationary state. 5. ϕ provides a criterion of relative stability of two stable stationary states. 6. With proper reference states ϕ yields the stationary probability distribution of stochastic equations describing the given processes.

The structure of the theory is analogous to that at equilibrium and revolves into that theory as the system approaches an equilibrium point, rather than a stationary state.

We have established a new fluctuation-dissipation relation for one-variable nonlinear processes which connects the macroscopic deterministic net reaction rate, the probability diffusion coefficient, and the species-specific affinity. This fluctuation-dissipation relation may also be viewed as a force-flux relation. The main feature of this development is the symmetry with respect to the contributions of the forward and backward chemical processes to fluctuations and relaxation. Two new physical interpretations of the probability diffusion coefficient are given: one corresponds to a measure of the strength of fluctuations at a steady state, and the other to a measure of the instability of a given fluctuation state. The dispersion of the number q of reaction events in a given time interval is given by a generalized Einstein relation: $\{\Delta q^2\}=2VD(x)t$, where V is the volume of the system. Further, the diffusion coefficient D(x) is proportional to the reciprocal value of the mean age $\{\tau(x)\}$ of a fluctuation state characterized by the concentration x: $D(x)=1/[2V\{\tau(x)\}]$. These interpretations are not related to the use of a Fokker-Planck approximation of the chemical master equation.

For single variable systems the excess work, ϕ, is a state function which, however, is not the case for multi-variable systems. Hence in the evaluation of the excess work for multi-variable systems a path of integration through the concentration space for chemical systems must be chosen. If the process to be described follows the deterministic equations of motion then that path is also the most probable path in a stochastic investigation and the excess work must then be evaluated along that path. If, however, we investigate fluctuations away from a stationary state then the excess work for such fluctuations must be evaluated along the most probable path of a fluctuation from a stationary state to a given nonstationary state. We have shown that, in general, deterministic paths of relaxation to stationary states are not the same as most probable fluctuational paths away from stationary states. We have investigated these issues by means of the eikonal (WKB type) solution of the master equation for two-variable chemical systems with multiple stationary states. If we suppose there to be two stable stationary states then these are separated by a deterministic separatrix and as well by a different fluctuational separatrix. Caustics occur in the system and require careful analysis. We have checked the validity of the eikonal approximation against a Monte Carol solution of the master equation and find the results accurate.

We have conducted extensive calculations and experiments to test our theory in regard to relative stability of two stable stationary states. Consider a volume such as a tube filled with the system, subject to given constraints, in one of the two stable stationary states. Next consider a similar volume for the same external constraints filled with the system in the other of the two stable stationary states. On connection of the two tubes there occurs a motion of the front between the two different stationary states such that the more stable stationary state eliminates the less stable stationary state. At equistability of the two stable stationary states the front velocity is zero. We have shown that the excess work for creating the front between the two stable stationary states from either of the two stable stationary states provide the necessary criterion of relative stability. Thus if the excess work calculated from one of the stable stationary states to the stable front of the interface between the two stationary states exceeds that of the excess work from the other stable stationary state to that stable front then the interface moves in the direction of annihilating the region with the larger excess work. Experiments in relative stability in the bistable multi-variable bromate-ferroin reaction confirm this result of the theory.

We have attempted an application of our theory to a thermodynamic theory of hydrodynamics. The thermodynamic potential (state) functions for irreversible processes approaching equilibrium are known: for example, the Gibbs free energy change for the processes at constant temperature and pressure. Changes in this Gibbs free energy yield the maximum work available from the changes. Then, by analogy, the goals of thermodynamics for hydrodynamic processes are the establishment of macroscopic evolution criteria (Liapunov functions) with physical significance, such as the connection with excess work; the work (and power) available from a transient decay to a stationary state; macroscopic necessary and sufficient criteria of stability; thermodynamic criteria for bifurcations; a thermodynamic criterion of relative stability of stable attractors in systems with more than one attractor, that is, a thermodynamic criterion of state selection; and finally a connection of the thermodynamic formulation to fluctuations.

We start with the Navier-Stokes equations and the Boussinesq approximation and then proceed according to the studies of Saltzmann, who reduces these equations to a set of ordinary differential equations by means of a spectrum expansion. In lowest order one then arrives at the Lorenz equations and we investigate the steady states of those equations. We construct the excess work and show that it has the following properties. 1. The differential of ϕ is expressed in terms of thermodynamic functions: the energy for viscous flow and the entropy for thermal conduction when taken separately. 2. ϕ is an extremum at all stationary states, a minimum (maximum) at stable (unstable) stationary states, and thus yields necessary and sufficient criteria for stability; 3. ϕ describes the bifurcation from homogeneous to inhomogeneous stationary states; 4. ϕ is a Liapunov function with physical significance parallel to that of the Gibbs free energy change (maximum work) on relaxation to an equilibrium state; 5. ϕ is the thermodynamic "driving force" (potential) towards stable stationary states; 6. ϕ is a component of the total dissipation during the relaxation towards a stable stationary state; 7. for constraints leading to equilibrium ϕ reduces to the known thermodynamic function, which is the work of displacing the system from the equilibrium for those given constraints; and 8. ϕ qualitatively explains the positive energy release in both the destruction and formation of a convective structure in a Rayleigh-Bénard experiment.

References marked with a * denote accreditation to The Department of Energy/Basic Engineering Sciences Program.

302. "Experiments on relative stability in the bistable multivariable bromate-ferroin reaction", J. Phys. Chem. 97, 4708 (1993) Petra Foerster, Yi-Xue Zhang and John Ross.

* 303. "Tests of thermodynamic theory of relative stability in one-variable systems", J. Chem. Phys. 99, 3455 (1993), A. N. Wolff, A. Hjelmfelt, John Ross and P. M. Hunt.

304. "Thermodynamic and stochastic theory of reaction-diffusion systems with multiple stationary states", J. Chem Phys. 99, 3444 (1993) Xiaolin Chu, P. M. Hunt, K. L. C. Hunt and John Ross.

* 306. "Stationary probability distribution near stable limit cycles far from Hopf bifurcation points", Phys. Rev. E 48, 1646 (1993) Mark Dykman, Xiaolin Chu and John Ross.

* 307. "Towards a thermodynamic theory of hydrodynamics: The Lorenz equations", J. Phys. Fluids 6, 550 (1994) Manuel G. Velarde, Xiao-Xiaolin Chu, and John Ross.

* 310. "Large fluctuations and optimal paths in chemical kinetics", J. Chem. Phys. 100 5735, (1994) Mark I. Dykman, Eugenia Moria, and John Ross.

* 312. "H-theorem for telegrapher-type master equations", Phys. Let. A 184, 403 (1994) Marcel O. Vlad and John Ross.

314. "Fluctuation-dissipation relations for chemical systems far from equilibrium", J. Chem. Phys. 100 7268 (1994) Marcel O. Vlad and John Ross.

* 315. "Random paths and fluctuation-dissipation dynamics for one-variable chemical systems far from equilibrium", J. Chem. Phys. 100, 7279 (1994), Marcel O. Vlad and John Ross.

* 316. "Thermodynamic approach to nonequilibrium chemical fluctuations", J. Chem. Phys. 100, 7295 (1994) Marcel O. Vlad and John Ross.

* 318. "Generating functional approach to space-and time-dependent colored noise", Physical Review E 50, 798 (1994) Marcel O. Vlad, Michael C. Mackey, John Ross.

* 319. "Electro-chemical experiments on Thermodynamics at nonequilibrium steady states", J. Phys. Chem. 98, 9900 (1994) Allen Hjelmfelt and John Ross.

321. "Thermodynamic and stochastic theory of nonequilibrium systems: Fluctuation probabilities and excess work", J. Chem. Phys., Bo Peng, Katherine L. C. Hunt, Paul M. Hunt, Alberto Suàrez, and John Ross.

322. "Thermodynamic and stochastic theory of nonequilibrium systems: A Lagrangian approach to fluctuations and relation to excess work", J. Chem. Phys., Alberto Suàrez, John Ross, Bo Peng, Katherine L. C. Hunt, and Paul M. Hunt.

* 323. "A model of excitation and adaptation in bacterial chemotaxis", Biophys. Journal 68, 708 (1995), David C. Hauri and John Ross.

LINEAR KINETIC THEORY AND PARTICLE TRANSPORT IN STOCHASTIC MIXTURES

G. C. Pomraning

School of Engineering and Applied Science
University of California, Los Angeles
Los Angeles, CA 90095-1597

Abstract

We consider the formulation of linear transport and kinetic theory describing energy and particle flow in a random mixture of two or more immiscible materials . Following an introduction, we summarize early and fundamental work in this area, and we conclude with a brief discussion of recent results.

INTRODUCTION

In the last decade these has been considerable interest in the problem of describing linear particle transport in a stochastic medium consisting of two (or more) randomly mixed immiscible materials. The goal in this research has been to develop a relatively simple and accurate description for the ensemble-averaged solution of the stochastic transport problem. In this brief report, we will attempt to summarize the salient features of this work and present an overall view of the status of this research, with particular emphasis on the work of the present author.

The generic linear transport equation we will concerned with is written

$$\frac{1}{v}\frac{\partial \psi}{\partial t} + \mathbf{\Omega}\cdot\nabla\psi + \sigma\psi = \frac{\sigma_s}{4\pi}\varphi + S, \tag{1}$$

where

$$\varphi = \int_{4\pi} d\mathbf{\Omega}\psi(\mathbf{\Omega}). \tag{2}$$

In writing Eqs. (1) and (2) we have used the notation of neutron transport theory, but our considerations are equally applicable in any linear transport setting. The dependent variable in Eq. (1) is the angular flux $\psi(\mathbf{r},\mathbf{\Omega},t)$, with $\mathbf{r},\mathbf{\Omega}$, and t denoting the spatial, angular (neutron flight direction), and time variables, respectively. The quantity $\varphi(\mathbf{r},t)$ is the scalar flux, v is the neutron speed, $\sigma(\mathbf{r},t)$ is the macroscopic total cross section, $\sigma_s(\mathbf{r},t)$ is the macroscopic scattering cross section, and $S(\mathbf{r},\mathbf{\Omega},t)$ denotes any internal source of neutrons. We have assumed isotropic and coherent (no energy exchange) scattering in Eq. (1), but this simplification is not necessary for the essentials of the considerations to follow. Thus Eq. (1) is a monoenergetic (one group) transport equation, and there is no need to display the independent energy variable which is simply a parameter.

To treat the case of a binary statistical mixture, the quantities σ, σ_s, and S in Eq. (1) are considered as discrete random variables, each of which assumes, at any $\mathbf{r}, \mathbf{\Omega}, t$, one of two sets of values characteristic of the two materials constituting the mixture. We denote the two materials by an index i, with $i = 0$, 1, and in the ith material these three quantities are denoted by $\sigma_i(\mathbf{r},t), \sigma_{si}(\mathbf{r},t)$ and $S_i(\mathbf{r},\mathbf{\Omega},t)$. That is, as a neutron traverses the mixture along any path, it encounters alternating segments of the two materials, each of which has known deterministic values of σ, σ_s, and S. The statistical nature of the problem enters through the statistics of the material mixing, i.e., through the probabilistic knowledge as to which material is present in the mixture at space point $\mathbf{r}$ and time t. Since σ, σ_s and S in Eq. (1) are (two state, discrete) random variables, the solution of Eqs. (1) and (2) for ψ and φ is stochastic, and we let $\langle\psi\rangle$ and $\langle\varphi\rangle$ denote the ensemble-averaged angular and scalar fluxes, respectively. The goal is to develop accurate and , hopefully, simple models for these ensemble-averages.

To discuss this problem in a qualitative way, it is convenient to consider the simple case of time-independent transport in a purely absorbing ($\sigma_s = 0$) medium. Then Eq. (1) reduces to

$$\frac{d\psi}{ds} + \sigma\psi = S, \tag{3}$$

where s denotes the spatial variable in the direction of propagation. If we write any random variable Q as the sum of its ensemble average $\langle Q\rangle$ and the deviation from this average $\tilde{Q}$, an ensemble averaging of Eq. (3) gives

$$\frac{d\langle\psi\rangle}{ds} + \langle\sigma\rangle\langle\psi\rangle + \langle\tilde{\sigma}\tilde{\psi}\rangle = \langle S\rangle. \tag{4}$$

It is clear from Eq. (4) that one needs to calculate (or approximate) the cross correlation term involving the ensemble average of the product of $\tilde{\sigma}$ and $\tilde{\psi}$ to obtain a formulation for the quantity of interest, namely $\langle\psi\rangle$.

On physical grounds, and it can also be shown mathematically by using asymptotics, it is clear that this term is very small and can be neglected when $\sigma_i l_i \ll 1$, where l_i is a characteristic chord length for the material packets of material i. However, when this inequality is not satisfied, the neglect of the cross correlation term in Eq. (4) can lead to large errors in $\langle\psi\rangle$. In particular, the attenuation of a beam of particles can be grossly overestimated by using Eq. (4) without the cross correlation term. Simply stated then, the challenge is to compute the cross correlation term in Eq. (4). To do this, one must specify the statistics of the material mixing, and we discuss both Markovian and non-Markovian mixtures.

FUNDAMENTAL RESULTS

References to the original works for the material discussed in this section can be found in the recent book by the present author.[1]

We initially consider the simple transport equation given by Eq. (3), under the assumption of Markovian mixing. These mixing statistics are defined by a no-memory statement. Given that point s is in material i, the probability of point $s + ds$ being in material $j \neq i$ is given by

$$Prob(i \rightarrow j) = \frac{ds}{\lambda_i(s)}, \qquad j \neq i, \tag{5}$$

where the $\lambda_i(s)$ are the prescribed Markovian transition probabilities. The probability $p_i(s)$ of finding material i at position s, and the correlation length $\lambda_c(s)$ for the Markov mixture are uniquely and simply related to the $\lambda_i(s)$. With the mixing statistics defined by Eq. (5), one can obtain an exact description for $\langle\psi\rangle$ corresponding to the transport problem given by Eq. (3). This is given by the two coupled equations

$$\frac{d}{ds}\begin{bmatrix}\langle\psi\rangle \\ \chi\end{bmatrix} + \begin{bmatrix}\langle\sigma\rangle & \nu \\ \nu & \hat{\sigma}\end{bmatrix}\begin{bmatrix}\langle\psi\rangle \\ \chi\end{bmatrix} = \begin{bmatrix}\langle S\rangle \\ T\end{bmatrix}, \tag{6}$$

where

$$\nu\chi = \langle\tilde{\sigma}\tilde{\psi}\rangle, \qquad \nu = (p_0p_1)^{1/2}(\sigma_0 - \sigma_1), \tag{7}$$

$$\langle\sigma\rangle = p_0\sigma_0 + p_1\sigma_1, \qquad \hat{\sigma} = p_1\sigma_0 + p_0\sigma_1 + \frac{1}{\lambda_c}, \tag{8}$$

$$\langle S\rangle = p_0S_0 + p_1S_1, \qquad T = (p_0p_1)^{1/2}(S_0 - S_1). \tag{9}$$

Two derivations of Eq. (6) can be given. The first is based upon the so-called method of smoothing. Subtraction of Eq. (4) from Eq. (3) gives

$$\frac{d\tilde{\psi}}{ds} + \langle\sigma\rangle\tilde{\psi} + \left[\tilde{\sigma}\tilde{\psi} - \langle\tilde{\sigma}\tilde{\psi}\rangle\right] = \tilde{S} - \tilde{\sigma}\langle\psi\rangle. \tag{10}$$

Inserting a smallness parameter in front of the bracketted term in Eq. (10) and seeking a solution as a power series in this smallness parameter gives the Neumann series

$$\tilde{\psi} = \sum_{n=0}^{\infty}(-1)^n[G(I-P)\tilde{\sigma}]^nG(\tilde{S} - \tilde{\sigma}\langle\psi\rangle), \tag{11}$$

where I is the identity and G and P are Green's and projection operators defined by

$$Gf = \int_0^s ds' \left[exp - \int_{s'}^s d\xi \langle \sigma(\xi) \rangle \right] f(s'), \qquad Pf = \langle f \rangle. \tag{12}$$

For Markovian statistics, all of the terms in the sum of Eq. (11) can be evaluated and the infinite summation performed. The result of the these algebraic manipulations is just Eq. (6).

The second derivation of Eq. (6) is based upon the observation that the transport problem given by Eq. (3) describes a Markov process; it is an initial value problem with the spatial variable s playing the role of time. Thus, together with the assumed Markovian mixing, we have a joint Markov process and we can write a Liouville master equation for the joint probability $P_i(s, \psi)$, defined such that $P_i d\psi$ is the probability of finding material i and intensity ψ lying between ψ and $\psi + d\psi$ at position s. This master equation is given by

$$\frac{\partial P_i}{\partial s} - \frac{\partial}{\partial \psi}(\psi \sigma_i P_i - S_i P_i) = \frac{P_j}{\lambda_j} - \frac{P_i}{\lambda_i}, \quad j \neq i. \tag{13}$$

The probability $p_i(s)$ is just the integral of $P_i(s, \psi)$ over ψ, and the conditional ensemble-averaged intensity given that position s is in material i, $\psi_i(s)$, is the integral of $\psi P_i(s, \psi)$ over ψ, divided by p_i. Multiplying Eq. (13) by ψ and integrating over ψ gives two coupled equations for the ψ_i. Making the change of variables

$$\langle \psi \rangle = p_0 \psi_0 + p_1 \psi_1, \qquad \chi = (p_0 p_1)^{1/2} (\psi_0 - \psi_1) \tag{14}$$

once again leads to Eq. (6).

No such exact results are available when time-dependence and scattering are present in the transport problem, i.e., when Eq. (1) is the underlying stochastic transport equation. In this case, the algebra of the method of smoothing cannot be carried through. Further, with scattering the transport problem is not a Markov process (it is a boundary value problem) and hence the master equation approach cannot rigorously be used. Nevertheless, it has been suggested that the use of the master equation might lead to a useful, albeit approximate, model. This model is

$$\left(\frac{1}{v} \frac{\partial}{\partial t} + \mathbf{\Omega} \cdot \nabla + \mathbf{\Sigma} \right) \begin{bmatrix} \langle \psi \rangle \\ \chi \end{bmatrix} = \frac{1}{4\pi} \mathbf{\Sigma}_s \begin{bmatrix} \langle \varphi \rangle \\ \eta \end{bmatrix} + \begin{bmatrix} \langle S \rangle \\ T \end{bmatrix}, \tag{15}$$

where

$$\mathbf{\Sigma} = \begin{bmatrix} \langle \sigma \rangle & \nu \\ \nu & \hat{\sigma} \end{bmatrix}, \qquad \mathbf{\Sigma}_s = \begin{bmatrix} \langle \sigma_s \rangle & \nu_s \\ \nu_s & \hat{\sigma}_s \end{bmatrix}, \tag{16}$$

where, in addition to Eqs. (7) through (9), we have

$$\langle \varphi \rangle = \int_{4\pi} d\mathbf{\Omega} \langle \psi \rangle, \quad \eta = \int_{4\pi} d\mathbf{\Omega} \chi, \quad \nu_s = (p_0 p_1)^{1/2} (\sigma_{s0} - \sigma_{s1}), \tag{17}$$

$$\langle \sigma_s \rangle = p_0 \sigma_{s0} + p_1 \sigma_{s1}, \qquad \hat{\sigma}_s = p_1 \sigma_{s0} + p_0 \sigma_{s1}. \tag{18}$$

Several other derivations of this model are available. Sahni has shown that the assumption of independent particle flight paths leads to Eq. (15), and he has also shown that nuclear reactor noise techniques can be used to obtain this model. It has also been demonstrated that one can derive exact particle balance equations in this stochastic transport setting, but involving two ensemble averages conditioned upon being in material i, namely a volumetric average ψ_i and a surface (interface between materials) average $\bar{\psi}_i$. Making the approximation that these two ensemble averages are equal again yields the model given by Eq. (15). Numerical comparisons with exact Monte Carlo results shows the accuracy of this model to be of the order of ten percent or so, with the error being the largest, as expected, for problems with multiple scattering interactions.

Although no exact transport-like equation(s) formulation is available in general for $\langle\psi\rangle$ in the presence of time dependence and scattering, a few exact results have been reported for certain time-independent problems including the scattering interaction in rod (particles are restricted to move along a line) and planar geometry. Vanderhaegen and Deutsch considered the sourcefree purely scattering rod problem and used a Riccati transformation to convert the boundary value transport problem for the intensity to an initial value problem for the rod transmission. They then applied the master equation approach to this initial value problem. Their results were confirmed in a paper devoted to numerical and analytical solution methods for the Liouville master equation applicable to a large class of initial value problems. An exact formalism in rod and planar geometry has been developed for a restricted class of problems, in which σ_s/σ and S/σ are nonstochastic; the only stochasticity is the optical depth variable. The results of Vanderhaegen and Deutsch were again confirmed, and results for several classical halfspace and infinite medium transport problems were developed.

If one accepts Eq. (15) as a reasonable model of particle transport in a binary Markovian mixture, two simplifications involving certain asymptotic limits have been reported. The first of these corresponds to a small amount, of $O(\epsilon^2)$, of one material admixed with an $O(1)$ amount of the second material. Further, the first material has large, of $O(1/\epsilon^2)$, source and cross sections compared to $O(1)$ quantities for the second material. In this asymptotic limit, one finds a renormalized transport equation of the standard form given by

$$\left(\frac{1}{v}\frac{\partial}{\partial t} + \mathbf{\Omega}\cdot\nabla + \sigma_{eff}\right)\langle\psi\rangle = \frac{\sigma_{s,eff}}{4\pi}\langle\varphi\rangle + S_{eff} + O(\epsilon^2), \tag{19}$$

with

$$\sigma_{eff} = \langle\sigma\rangle - \frac{\nu^2}{\hat{\sigma}}, \qquad \sigma_{s,eff} = \sigma_{eff} - \sigma_{a,eff}, \tag{20}$$

and

$$\sigma_{a,eff} = (\langle\sigma\rangle - \langle\sigma_s\rangle) - \frac{(\nu-\nu_s)^2}{(\hat{\sigma}-\hat{\sigma}_s)}, \qquad S_{eff} = \langle S\rangle - \frac{(\nu-\nu_s)}{(\hat{\sigma}-\hat{\sigma}_s)}T. \tag{21}$$

Equation (21) for S_{eff} assumes that the sources are isotropic, i.e., $S_i \neq S_i(\mathbf{\Omega})$. The corresponding expression for anisotropic sources is more complex. The result given by Eqs. (19) through (21) is robust in that all of these effective cross sections and source are always nonnegative, even when one is far from the asymptotic limit under consideration. This derivation of a renormalized transport equation as an asymptotic limit has been generalized to a mixture containing an arbitrary number of the material components, and leads to an entire class of reduced (in complexity) transport descriptions.

The second asymptotic limit of Eq. (15) is one in which the scattering interaction is dominant, of $O(1)$. Absorption, sources, and all derivatives are assumed small, of $O(\epsilon^2)$, except for the spatial derivative which is scaled to be $O(\epsilon)$. This scaling eliminates the angular variable in the transport problem, and is analogous to the Hilbert expansion which gives the Euler material equations from the Boltzmann equation. If we restrict ourselves to isotropic sources as well as an isotropic correlation length, one finds in this asymptotic limit two coupled diffusion equations given by

$$\left(\frac{1}{v}\frac{\partial}{\partial t} - \nabla \cdot \mathbf{D}\nabla + \mathbf{\Sigma}_a\right)\begin{bmatrix} \langle\varphi\rangle \\ \eta \end{bmatrix} = 4\pi \begin{bmatrix} \langle S\rangle \\ T \end{bmatrix} + O(\epsilon^2), \tag{22}$$

where $\mathbf{\Sigma}_a = \mathbf{\Sigma} - \mathbf{\Sigma}_s$ and

$$\mathbf{D} = \frac{1}{3}\mathbf{\Sigma}^{-1} = \frac{1}{3(\langle\sigma\rangle\hat{\sigma} - \nu^2)}\begin{bmatrix} \hat{\sigma} & -\nu \\ -\nu & \langle\sigma\rangle \end{bmatrix}. \tag{23}$$

It can easily be shown that the diffusion coefficient matrix $\mathbf{D}$ is positive definite under all choices of the physical parameters, thus assuring robustness in this diffusion approximation. Since the scaling which lead to Eq. (22) corresponds to a singular perturbation problem, both boundary and temporal layers exist. Performing the appropriate asymptotic matching analyses, one obtains boundary and initial conditions for Eq. (22). The boundary condition is of the mixed (Robbin) type, involving the number 0.710446... , the classic linear extrapolation distance for the Milne problem.

We note the suggestion that non-Markovian statistics of the renewal type can be treated by modifying the correlation length λ_c in Eq. (8). Specifically, if $Q_i(z)$ is the probability that a segment length in material i exceeds length z, then it has been proposed that Eq. (15) approximately describes this statistical situation, if λ_c in $\hat{\sigma}$ [see Eq. (8)] is replaced with $q\lambda_c$, where

$$q = \frac{1}{\sigma_0}\left(\frac{1}{\tilde{Q}_0(\sigma_0)} - \frac{1}{\lambda_0}\right) + \frac{1}{\sigma_1}\left(\frac{1}{\tilde{Q}(\sigma_1)} - \frac{1}{\lambda_1}\right) - 1. \tag{24}$$

Here $\tilde{Q}_i(\sigma_i)$ is the Laplace transform of $Q_i(z)$, evaluated at the transform variable σ_i. For Markovian statistics, $Q_i(z)$ is exponential with decay length λ_i, and in this case $q = 1$. Finally, most of these binary mixture considerations have been generalized to a mixture with more than two components.

RECENT RESULTS

We close this report with a very brief discussion of results obtained in the last few years.[2-18] Space limitations allow simply a listing of such results, and references where more detail can be found. One group of papers[3,12-14,18] deals with the generic problem of attempting to construct a more accurate model than that given by Eq. (15). One such model[14] retains the simplicity of two equations in two unknowns as in Eq. (15), but it incorporates small correlation length physics into these two equations.[13] Two other models[3,18] involve additional equations, yielding four equations in four unknowns. These models are obviously more complex, but are more accurate. An independent variational approach to stochastic transport has also been attempted,[12] with limited success. A paper has been published[6] which compares the accuracy of several models against Monte Carlo benchmark results. Such benchmark results are available for both Markovian and non-Markovian statistics.[10]

Another group of papers[4,5,7,8,16,17] deals with diffusive approximations to the two equation model given by Eq. (15). Two of these papers[4,17] develop flux-limited diffusion equations, a third deals with the P_2 approximation,[16] and the remaining three[5,7,8] develop various asymptotic diffusive limits which result from different scalings of the Markovian transition lengths.

Finally, four papers have been published concerned with applications of this stochastic transport formalism. Two of these[9,11] deal with the cloud-radiation interaction problem within the context of general circulation models of the atmosphere, one addresses a random heterogeneity problem in fission reactor fuels,[2] and one is concerned with beam transport and energy deposition as might be encountered in medical applications.[15]

Under continuing DOE support, we expect to report additional results from this line of research in the near future.

ACKNOWLEDGMENT

The work reported here was partially supported by the U.S. Department of Energy under grant DE-FG03-93ER14355.

REFERENCES

1. G. C. Pomraning, *Linear Kinetic Theory and Particle Transport in Stochastic Mixtures*, World Scientific Publishing, Singapore (1991).

2. R. Sanchez and G. C. Pomraning, *Ann. Nucl. Energy* **18**, 371 (1991).

3. G. C. Pomraning, *J. Quant. Spectrosc. Radiat. Transfer* **46**, 221 (1991).

4. M. Sammartino and G. C. Pomraning, *J. Quant. Spectrosc. Radiat. Transfer* **46**, 237 (1991).

5. M. Sammartino, F. Malvagi, and G. C. Pomraning, *J. Math. Phys.* **33**, 1480 (1992).

6. F. Malvagi and G. C. Pomraning, *Nucl. Sci. Eng.* **111**, 215 (1992).

7. F. Malvagi, G. C. Pomraning, and M. Sammartino, *Nucl. Sci. Eng.* **112**, 199 (1992).

8. G. C. Pomraning, *Ann. Nucl. Energy* **19**, 737 (1992).

9. F. Malvagi, R. N. Byrne, G. C. Pomraning, and R. C. J. Somerville, *J. Atmos. Sci.* **50**, 2146 (1993).

10. B. Su and G. C. Pomraning, *J. Quant. Spectrosc. Radiat. Transfer* **50**, 211 (1993).

11. F. Malvagi and G. C. Pomraning, *Atmospheric and Oceanic Optics* **6**, 610 (1993). Russian translation in same journal: **6**, 1064 (1993).

12. B. Su and G. C. Pomraning, *J. Quant. Spectrosc. Radiat. Transfer* **51**, 467 (1994).

13. B. Su and G. C. Pomraning, *J. Quant. Spectrosc. Radiat. Transfer* **51**, 893 (1994).

14. G. C. Pomraning and B. Su, "A Closure for Stochastic Transport Equations," *Proc. International Conference on Reactor Physics and Reactor Computations*, Ben-Gurion University of the Negev-Press, pp. 672-679 (1994).

15. G. C. Pomraning and A. K. Prinja, *Transport Th. Statis. Phys.* **24**, 565 (1995).

16. B. Su and G. C. Pomraning, "P_1, P_2, and Asymptotic Approximations for Stochastic Transport," *Nucl. Sci. Eng.*, accepted for publication.

17. G. C. Pomraning, "Flux-Limting in Three-Dimensional Stochastic Radiative Transfer," *J. Quant. Spectrosc. Radiat. Transfer*, accepted for publication.

18. B. Su and G. C. Pomraning, "Modification to a Previous Higher Order Model for Particle Transport in Binary Stochastic Media," *J. Quant. Spectrosc. Radiat. Transfer*, accepted for publication.

DYNAMICS OF MISCIBLE DISPLACEMENTS IN ROUND TUBES

E. Meiburg, T. Maxworthy, P. Petitjeans*, and C.-Y. Chen

Dept. of Aerospace Engineering
University of Southern California
Los Angeles, CA 90089-1191

*permanent address: Laboratoire de Physique et Mécanique des Milieux Hétérogenes
Ecole Supérieure de Physique et de Chimie Industrielles
10, rue Vauquelin, F-75231 Paris cedex 05, France

ABSTRACT

A combined experimental and numerical investigation of miscible two-phase flow in a capillary tube is reported. The fraction of fluid left behind on the wall is obtained as a function of the Peclet, Atwood, and Froude numbers. Scaling arguments are presented for two distinct flow regimes, dominated by diffusion and convection, respectively. In the latter one, an effective surface tension value can be estimated.

INTRODUCTION

An improved understanding of the dynamics of multiphase porous media flows remains an essential prerequisite for progress in the fields of enhanced oil recovery, fixed bed regeneration, hydrology, and filtration. From basic stability theory we know that, if the displacing fluid is less viscous than the displaced fluid, the unfavorable mobility profile is likely to lead to the well-known fingering instability, a topic that has been reviewed by Saffman [1] and Homsy [2]. Depending on whether the fluids are immiscible or miscible, one can distinguish two fundamentally different problems: In the *immiscible* case, where surface tension acts at the interface between the two fluids, the capillary number, which represents the ratio of viscous to surface tension forces, is a dynamically important parameter. It determines the most unstable wavelength of the fingering instability, as well as the dynamics of the evolving fingers. For *miscible* displacements, it is conventionally assumed that the dynamics are governed by the relative importance of convective and diffusive effects, as expressed by the Peclet number. However, the proper and accurate form of the governing equations and related boundary conditions in the area of contact between the miscible fluids is not known. Past investigations relied on ad hoc approaches that cannot be rigorously justified. Zimmermann and Homsy [3] have taken a first step towards more realistic conditions by assuming an anisotropic, velocity dependent Taylor dispersion approach. Within the present investigation, we address this issue by conducting physical as well as numerical experiments within capillary tubes, which can be considered a simple model of the miscible displacement process within a single pore of a porous medium. In particular, we carry out Taylor's [4] experiment (cf. also the numerical investigation by Reinelt and Saffman [5]) in capillary tubes using miscible fluids. We discuss the possibility to define an "effective" surface tension and capillary number, on the basis of both computational and experimental results.

GOVERNING EQUATIONS

Our investigation concerns the displacement of a more viscous phase '2' by a less viscous one '1' in a capillary tube of diameter d. To this end, we consider the incompressible Stokes equations in axisymmetric form. The concentration field is governed by a convection-diffusion equation, in which the diffusion coefficient D is taken to be constant. This represents a simplifying assumption, as the experimental measurements to be discussed below reveal a concentration dependence of the diffusion coefficient. Density is assumed to vary linearly with the concentration, while the viscosity is taken to depend exponentially on it. After rendering the governing equations dimensionless by means of characteristic scales, we identify as the governing dimensionless parameters a Peclet, an Atwood, and a Froude number

$$Pe = \frac{Ud}{D} \quad , \quad At = \frac{\mu_2 - \mu_1}{\mu_2 + \mu_1} \quad , \quad F = \frac{gd^2}{\nu_2 U}\frac{\rho_2 - \rho_1}{\rho_2}$$

Here U represents the of the unperturbed Poiseuille flow far away from the mixing region, while g denotes the gravitational acceleration, which is assumed to act in or against the direction of the displacement. ρ indicates density.

NUMERICAL APPROACH

We solve the incompressible Stokes equations in axisymmetric form, employing streamfunction and vorticity variables. In this way, the pressure is eliminated, and the continuity equation is satisfied identically. At the tube wall and the centerline, we employ standard boundary conditions for the velocity components and the normal derivative of the concentration. At the in- and outflow boundaries, we set the second derivatives in the streamwise direction to zero. Test calculations for computational domains of different sizes confirm that these conditions are appropriate. The convective terms in the concentration equation are represented by four point upwind biased finite difference stencils, whereas the diffusive terms are discretized by five point central differences. The elliptic vorticity equation is solved by means of a standard multigrid technique.

COMPUTATIONAL RESULTS

$Pe \geq O(10^3)$

The evolution of the flow in this parameter regime is exemplified by the case $Pe = 1,600$ and $At = 0.9866$, shown in figure 1 in a moving reference frame. Gravity is absent for this flow.

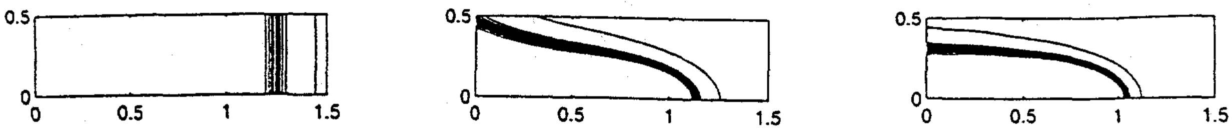

Fig. 1: Concentration contours at times 0, 1, and 3.

The initial condition specifies a one-dimensional error-function profile for the concentration, along with axisymmetric Poiseuille flow for the velocity components. The velocity field results in an immediate strong deformation of the concentration distribution in the interior of the tube, while at the wall concentration changes are the result of diffusion only. The transient evolution of the concentration distribution, in turn, causes corresponding changes in the viscosity field, thereby modifying the velocity field. This effect distinguishes the present situation from the one analyzed by Taylor [6], in which there is no feedback by the concentration distribution onto the velocity field. For the present parameters, we observe the development of a well-defined finger of the less viscous fluid in the center of the tube. The finger tip consists of a steep concentration front, while its sides are formed by diffusively spreading layers over which the concentration varies. The figure indicates that the mixed inflow/outflow boundary to the left is handled well by the present set of numerical boundary conditions, as there are no detectable disturbances propagating from the boundary towards the finger tip.

By time $t = 2$, the finger tip shape and the associated concentration field have reached a quasisteady state. This is confirmed by the propagation velocity V_{tip} of the finger tip, which is defined as the velocity with which the $c = 0.5$ contour moves along the tube's axis. The steepness of the concentration front at the finger tip is determined by the local balance of strain and diffusion. The strength α of the local strain field is governed by the difference of the streamwise velocities ahead of and behind the finger tip. By assuming that this velocity difference of approximately $2(V_{tip} - 1)$ is achieved over a distance comparable to the tube radius, we obtain

$$\alpha \approx \frac{4(V_{tip} - 1)}{d}$$

A straightforward one-dimensional balance of strain and diffusion then yields for the front thickness δ_0 at the finger tip

$$\frac{\delta_0}{d} \approx \sqrt{\frac{D}{2(V_{tip} - 1)d}}$$

indicating that the front thickness scales with the square root of the inverse of the Peclet number formed with the velocity difference across the finger tip. For the present case, this results in $\delta_0/d \approx 1/30$, which is in good agreement with fig. 1. The one-dimensional analysis furthermore gives

$$\left.\frac{\partial c}{\partial x}\right|_{max} \approx \sqrt{\frac{2}{\pi}}\sqrt{\frac{(V_{tip} - 1)d}{D}}$$

which for the present parameters yields approximately 17. Considering the rough estimate of the strain intensity, this value is in reasonable agreement with the computational results of approximately 28, confirming that the concentration field near the finger tip is indeed determined by a nearly one-dimensional balance of strain and diffusion.

On the sides of the finger, the concentration layers grow diffusively with increasing distance from the finger tip. These layers will merge when $\delta/d \approx 0.5$. Straightforward scaling yields

$$\frac{\delta}{d} \approx \sqrt{\frac{Dt}{d^2}} \qquad , \qquad t \approx \frac{L_f}{V_{tip}}$$

where L_f represents the length of the finger as a function of time. Consequently, the diffusion layers will merge when the finger has reached a length $L_f = Ped/4$. Once the finger has grown to this length, the supply of uncontaminated fluid to the tip region will gradually be cut off, and eventually the quasisteady state will begin to decay. The above scaling laws indicate that we can neither employ a sufficiently large computational domain, nor can we carry the simulation to sufficiently long times, in order to capture these effects for the present set of parameters.

For practical considerations, a relevant quantity is the fraction of more viscous fluid left behind on the walls of the tube once the quasi-steady state has developed. Taylor [4] calculates an effective film thickness of this fluid from the tip velocity of the finger as $m = 1 - 0.5/V_{tip}$ In particular, it will be of interest to record $m = m(At)$ in the limit of infinitely large Pe. Since grid based numerical simulations will not provide accurate results for this limit, we resort to an extrapolation procedure for $V_{tip} = f(Pe^{-1})$. These calculations demonstrate that the tip velocity for $Pe = 1,600$ is within less than one per cent of the extrapolated value for $Pe \to \infty$. In view of the considerable computational cost associated with carrying out several simulations at different large Pe for each value of At in order to perform the extrapolation, we will in the following present the simulation results for $Pe = 1,600$ in lieu of $Pe \to \infty$. In this way, we arrive at the (m, At)-relationship depicted in fig. 2. Notice that for $At = 0.5$ we obtain $m < 0.5$ as a result of the finite Pe-effects. These lead to a diffusive slowing of the finger tip, and thereby to a reduced film thickness. The agreement with the experimental results, also shown in fig. 2 and to be discussed below, is resonable, although not perfect. A possible reason for the observed discrepancy includes non-axisymmetric flow features in the experiment, due to density differences between the two phases. We remark that the value $m \approx 0.61$ for the film thickness in the limit $At \to 1, Pe \to \infty$ agrees well with the observations by Cox [7] for immiscible flow in the limit $At \to 1, Ca \to \infty$, where Ca denotes the capillary number. Taylor [4] previously found a maximum value of 0.56, but he suggested that higher values might be reached. This indicates that as diffusion or surface tension, respectively, become very small, their dynamical significance decays to zero in a smooth fashion, so that the shape of the finger tip is determined by the viscosity contrast alone.

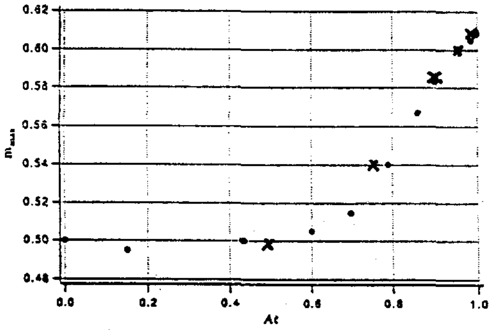

Fig. 2

× computational results
● experimental results

<u>$Pe \leq O(10^3)$</u>

For this range of lower Pe-numbers, the formation of a quasi-steady finger shape is not observed. Instead, as exemplified by the case of $Pe = 100, At = 0.9866$ (fig. 3), diffusion soon causes the concentration front to decay, thereby resulting in a progressively more spread out finger tip. As discussed above, at higher values of Pe a balance between strain and diffusion is in effect,

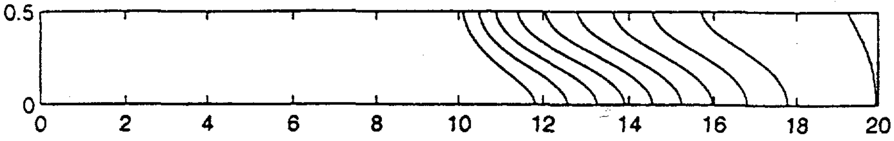

Fig.3

which maintains a steep concentration front. This quasi-one-dimensional balance can only exist if the front thickness at the tip, δ_0, is significantly smaller than the tube diameter. Consequently, there will be a critical level of diffusion beyond which the strain can no longer maintain a sufficiently steep front. In other words, below a critical value of Pe, the strain field will not be strong enough to counter the tendency of diffusion to smear out the finger front. The condition $\delta_0/d < const$ leads to an estimate for this critical value of Pe. With the above relationship for the ratio of front thickness and tube diameter, and with $V_{tip} \approx 1.25$, we obtain

$$\frac{\delta_0}{d} \approx \sqrt{\frac{2}{Pe}} < const$$

For $const = 1/10$ and $1/20$, this criterion yields $Pe_{crit} = 200$ and 800, respectively. Since the finger velocity, and consequently the strength of the strain field, depend on At, we expect Pe_{crit} to vary with At as well, although only weakly. Our numerical simulations for $At = 0.9866$ show the development of a quasi-steady finger with a steep front for $Pe \geq 800$, and a diffusing finger tip for $Pe \leq 400$. For lower values of At, we obtain diffusing fingers even for $Pe = 800$. These Pe-values are in reasonable agreement with the critical values estimated above.

The computational results of fig. 3 indicate that with increasing time the concentration field becomes progressively smoother. It is interesting to note that for $c \neq c(r)$, Poiseuille flow represents an exact solution to the Navier-Stokes equations, independent of the x-dependence of the concentration. As a result, we expect Taylor's [6] work on passive dispersion in Poiseuille flow to provide some guidance for the analysis of the flow development in the low Pe regime. In particular, under the assumption that axial diffusion is much less significant than radial diffusion, Taylor shows that convective effects on the concentration field will be small compared to diffusive effects if $\delta/d \gg Pe/58$, where δ is a measure of the thickness of the smeared out front. Consequently, we would expect to see Poiseuille flow under this condition. If we take δ as the distance along the centerline between the 0.1 and 0.9 concentration contours, then fig. 3 indicates that for $Pe = 100$ and $t = 10$ we have $\delta/d \approx 6$, while $Pe/58 \approx 1.7$. An examination of the fluid velocity confirms that by this time the velocity field has indeed decayed to near Poiseuille flow. The same observation can be made for $Pe = 200$ and $t = 22$, and for $Pe = 400$ and $t = 38$, when $\delta/d \approx 12.6$ and 23 for $Pe/58 \approx 3.4$ and 6.9, respectively. These results confirm the above scaling considerations, and we can conclude that Poiseuille flow will be reached approximately when $\delta/d \approx Pe/16$. Taylor furthermore observes that δ is related to time and the Taylor dispersion coefficient k as $\delta = 3.62\sqrt{kt}$. Here k depends on the tube diameter, the centerline velocity U of the Poiseuille flow, and the diffusion coefficient as $k = d^2U^2/768D$ With the above estimate for δ/d by the time Poiseuille flow is reached, we can now estimate the *time* it takes to approach Poiseuille flow as $t = 0.23Pe$. Consequently, after this time the cross-section-averaged concentration profile $c_m(x)$ should approach the shape of an error function. Equivalently, dc_m/dx should take the form of a Gaussian. This is confirmed by the numerical results, validating the above scaling arguments.

EXPERIMENTS

Apparatus

Two separate pieces of equipment were used in this study. The first, while not directly involved in the study of miscible displacements, was nontheless critical to its success. An extensive survey of the literature on the properties of the glycerine-water system, which was used in this study, failed to find any useful information on the molecular diffusivity D between the two species. Since the major control parameter Pe involves this property, it was essential to measure it independently. This was accomplished by introducing a glycerine-water mixture on top of a pure glycerine layer in a thin cell. A thin laser beam was projected through the interface and its deflection related to the local refractive index n gradient. The distribution of ∇n was measured at various times and the resultant growth of the interface thickness used to calculate the coefficients of species diffusivity. Due to the differences in mobility between glycerine and water, the diffusivity of the mixture into glycerine is less than that of glycerine into the mixture. The results are shown in figure 4. The value used in the calculation of Pe is the sum of the two individual diffusivities, which is dominated by the latter value except for values of c_G (glycerine concentration by weight) close to 100%.

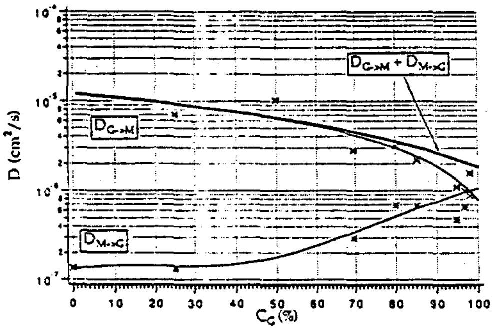

Fig. 4

The main piece of apparatus is shown in Figure 5. It is a minor adaptation of that due to Taylor [4]. It consists of two plastic manifolds connected by a precision bore capillary tube. Four different tube diameters d were used: 1,2,3 and $4mm$. For each experiment, the tube was first filled with pure glycerine from the right-hand reservoir. The desired mixture, dyed to improve its visibility, was then introduced at the left-hand end, the flow rate being controlled by a very precise compound needle valve. The motion of the nose of the intruding "finger" was timed between $10cm$ marks, and the amount of glycerine expelled from the tube during that time measured by an electronic balance to $1mg$. From these two measurements the effective film thickness m could

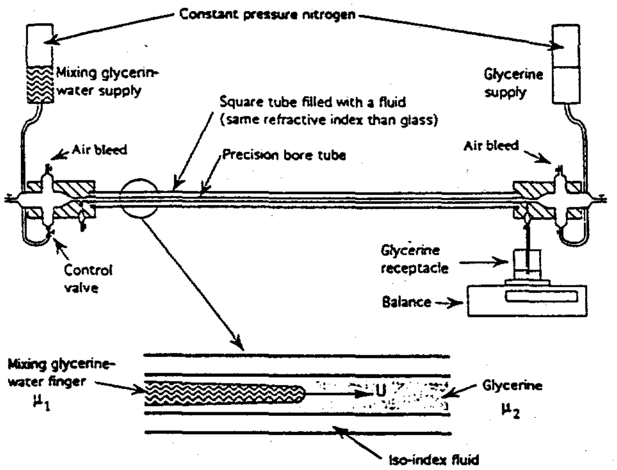

Fig. 5

be calculated.

Results

A large number of experiments were performed for all four tubes, for several values of At and various tube orientations, i.e., horizontal, vertical with the heavier glycerine on the bottom, and vertical with glycerine on top. The former orientation introduced interesting, non-axisymmetric, gravitational distortions of the finger that need to be discussed in more detail than possible here. On the other hand, the vertical cases introduced distortions that were axisymmetric so that these could be used to determine the state of the finger when gravity was not present, i.e., by plotting m as a function of F and interpolating to $F = 0$. Thus we concentrate on some aspects of the vertical cases that appear to be of widest interest. Notice that for the experimental results the measured velocity of the finger tip was used for the calculation of the dimensionless governing parameters. In figure 6 we show curves of m vs. Pe for $At = 0.79$ and for the two vertical orientations of a $3mm$ tube. Both curves asymptote $m = 0.54$ at large Pe. In fact, the curves for all values of At and all tube diameters asymptote a value of m that depends only on At (figure 2). At smaller values of Pe the curves diverge with one appearing to approach zero and the other unity. Repeating these measurements for other values of tube diameter, but the same value of At, allows us to construct curves of m or alternatively V_{tip} vs. F at a fixed value of Pe (figure 7). Interpolating to $F = 0$ gives the value of m for no gravitational effect, with the results for various values of Pe and for $At = 0.79$ given in figure 6. It appears that in this case $m \rightarrow 0.5$ as $Pe \rightarrow 0$,

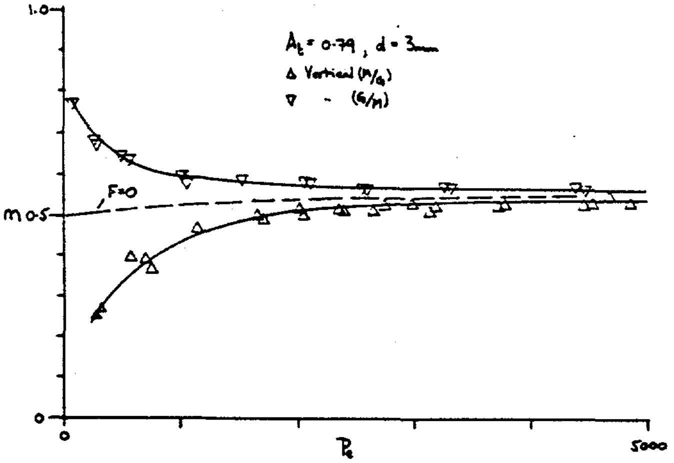

Fig. 6

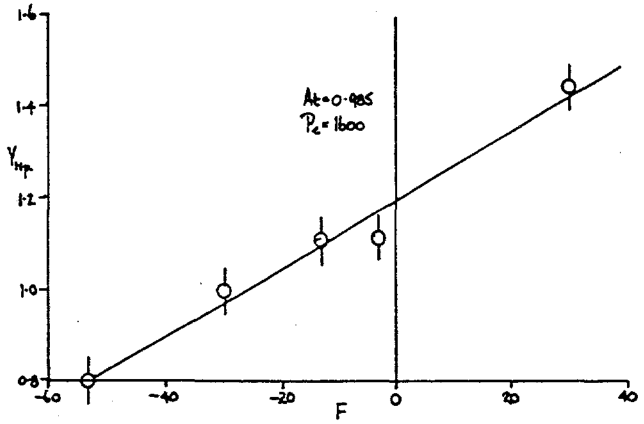

Fig. 7

as discussed in the previous section.

Two further observations are of interest. Firstly we note that when m is less than 0.5, Taylor [4] gives two possible streamline patterns for the flow relative to the moving nose. We have found that in such cases a thin needle of fluid is continuously ejected from the tip of the finger in a way that makes it clear that of the two flow pictures the one with a single stagnation ring on the finger surface is the one found in these experiments. Secondly, by matching Taylor's results of m vs. $Ca = \mu U/\sigma$ (where μ is the dynamic viscosity of the displaced fluid) for immiscible fluids, with the present measurements it is possible estimate an effective surface tension σ for the miscible interface for values of Pe greater than approximately 250, i.e., when a thin interface exists. Such a match is shown in figure 8 and results in an estimate for σ of

$$\sigma \approx \frac{1000}{3}\frac{\mu D}{d}$$

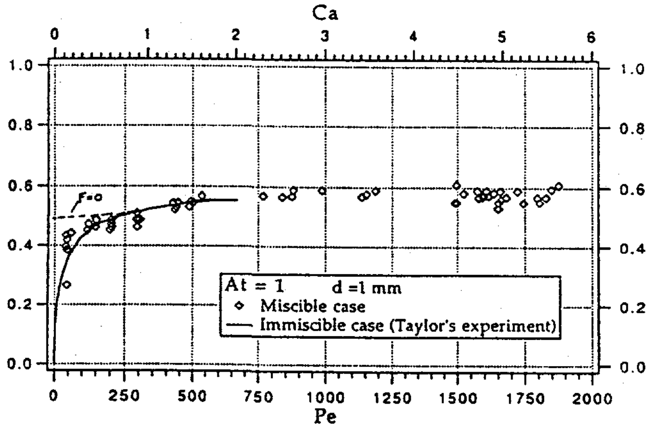

Fig. 8

ACKNOWLEDGMENTS

This work is being supported by the Department of Energy, Office of Basic Energy Sciences.

REFERENCES

1. P.G. SAFFMAN Viscous fingering in Hele-Shaw cells. J. Fluid Mech. 173, 73 (1986).
2. G.M. HOMSY Viscous fingering in porous media. Ann. Rev. Fluid Mech. 19, 271 (1987).
3. W. ZIMMERMANN and G.M. HOMSY Nonlinear viscous fingering in miscible displacement with anisotropic dispersion. Phys. Fluids A 3, 1859 (1991).
4. G.I. TAYLOR Deposition of a viscous fluid on the wall of a tube. J. Fluid Mech. 10, 161 (1961).
5. D.A. REINELT and P.G. SAFFMAN The penetration of a finger into a viscous fluid in a channel and tube. SIAM J. Sci. Stat. Comput. 6, 542 (1985).
6. G.I. TAYLOR Dispersion of soluble matter in solvent flowing slowly through a tube. Proc. R. Soc. A219, 186 (1953).
7. B.G. COX On driving a viscous fluid out of a tube. J. Fluid Mech. 14, 81 (1962).

SUPERCONDUCTING COHERENCE IN A VORTEX LINE LIQUID

Tao Chen and S. Teitel

Department of Physics and Astronomy
University of Rochester, Rochester, New York 14627

ABSTRACT

We carry out simulations of the anisotropic uniformly frustrated 3d XY model, as a model for vortex line fluctuations in high T_c superconductors. We compute the phase diagram as a function of temperature and anisotropy, for a fixed applied magnetic field B. We find two distinct phase transitions. Upon heating, there is first a lower $T_{c\perp}$ where the vortex line lattice melts and superconducting coherence perpendicular to the applied magnetic field vanishes. At a higher T_{cz}, within the vortex line liquid, superconducting coherence parallel to the applied magnetic field vanishes. For finite anisotropy, both $T_{c\perp}$ and T_{cz} lie well below the crossover from the vortex line liquid to the normal state.

INTRODUCTION

In the presence of an applied magnetic field, the low temperature state of a clean type II superconductor is the Abrikosov vortex line lattice, consisting of a triangular lattice of perfectly straight lines of vorticity in the phase of the complex superconducting wavefunction ψ. The lines are parallel to the magnetic field, with a density given by B/ϕ_0; B is the magnetic field that penetrates the sample ($B < H$), and $\phi_0 = hc/2e$ is the flux quantum. For a conventional "low temperature" superconductor, this vortex lattice persists up to a critical temperature $T_{c2}(H)$, where the amplitude of the spatially varying superconducting wavefunction vanishes, superconductivity is lost, and the normal metallic state is entered [1]. Experimentally, $T_{c2}(H)$ is signalled upon cooling, by the onset of a strong diamagnetism as well as by the vanishing of electrical resistance.

From a phenomenological point of view, the "high T_c" copper-oxide superconductors differ from conventional low T_c superconductors due to the dramatically enhanced role that thermal fluctuations play [2]. This is due to the high values of T_c, the very strong anisotropy arising from the layered nature of the materials, and the large ratio of magnetic penetration length $\lambda_\perp$ to coherence length ξ_0. For a magnetic field oriented perpendicular to the copper-oxide planes, theoretical models have predicted [2–5] that thermal fluctuations will cause the vortex line lattice to melt at a T well below the T_{c2} where the amplitude of the locally fluctuating ψ vanishes. Between these two temperatures is a new vortex line liquid state. Experimentally, this picture has been supported by the observation that, in high T_c materials, the onset of reversible diamagnetism occurs at a temperature well above that where resistance vanishes [6]; the separation between these temperatures increases with increasing B. According to this picture, the onset of diamagnetism at $T_{c2}(H)$ is associated with a growth in superconducting correlations, giving rise on short length scales to a finite superconducting wavefunction $\psi(\mathbf{r})$ in terms of which vortex lines can be defined. This T_{c2} marks a strong cross-over region, rather than a sharp thermodynamic transition. In the resulting vortex line liquid, free diffusion of vortex lines gives rise to "flux flow" electrical resistance [1]. The vanishing of resistance only occurs at a lower T when the line liquid freezes into a lattice.

MODEL

To investigate the above scenario we have carried out Monte Carlo simulations using the uniformly frustrated XY model as a model for a fluctuating superconductor [7]. Making the London approximation that the amplitude of the superconducting wavefunction is constant outside of a vortex core, $\psi(\mathbf{r}) = |\psi|e^{i\theta(\mathbf{r})}$, and discretizing the continuum to a cubic mesh of points, the Hamiltonian for our system is

$$\mathcal{H}[\theta_i] = -\sum_{\langle ij\rangle} J_{ij}\cos(\theta_i - \theta_j - A_{ij}) \tag{1}$$

where θ_i is the phase of the wavefunction at site i of the cubic mesh, the sum is over nearest neighbor bonds, $A_{ij} = (2\pi/\phi_0)\int_i^j \mathbf{A}\cdot d\mathbf{l}$ is the integral of the magnetic vector potential across the bond, and $J_{ij} = J_z$ or $J_\perp$ is the anisotropic coupling in the direction of the bond. The argument of the cosine is the gauge invariant phase difference across the bond, and is thus proportional to the supercurrent flowing along the bond. Since cosine is quadratic for small arguments, Eq.(1) represents the kinetic energy of the flowing supercurrents. If we identify the discrete spacing along $\hat{\mathbf{z}}$ as the distance d between copper-oxide planes, and the discrete spacing in the xy plane as representing the short length cutoff for a vortex core of radius ξ_0, we have

$$J_\perp \equiv \frac{\phi_0^2 d}{16\pi^3\lambda_\perp^2}, \qquad J_z = \frac{\phi_0^2\xi_0^2}{16\pi^3\lambda_z^2 d}, \tag{2}$$

where $\lambda_\perp$ and λ_z are the magnetic penetration lengths within and normal to the copper-oxide planes, respectively. We define an anisotropy parameter η as

$$\eta \equiv \sqrt{\frac{J_\perp}{J_z}} = \frac{\lambda_z}{\lambda_\perp}\frac{d}{\xi_0}. \tag{3}$$

In our model of Eq.(1) we ignore spatial variations and fluctuations in the internal magnetic field, taking $\nabla \times \mathbf{A} = B\hat{\mathbf{z}}$ a uniform constant. This should be valid provided

[7] that B is so large that the spacing between vortex lines $a_v = \sqrt{\phi_0/B} \ll \lambda_\perp$ (so the magnetic fields associated with each vortex line strongly overlap), yet B is small enough that $a_v \gg \xi_0$ (so details of the vortex cores are not important). The anisotropy must also be such that $d < \lambda_\perp^2/\lambda_z$, so that Josephson coupling between the planes dominates over magnetic coupling [5,8]. For our simulations, we thus take the A_{ij} as fixed constants, chosen to give a particular fractional density $f \equiv B\xi_0^2/\phi_0$ of vortex lines penetrating the xy plane [9].

To model a particular material, we would like to map out the phase diagram as a function of T and magnetic field B, for a fixed value of anisotropy η. However, due to commensurability difficulties between the triangular vortex lattice preferred in a continuum and the discrete sites permitted by our numerical mesh, different vortex line densities would form lattice structures of differing symmetry in the ground state. Since we are computationally limited to a fairly coarse mesh, this would make direct comparison of systems with different B difficult. We therefore choose to map out the phase diagram as a function of T and anisotropy η, for fixed B. We can see however, using dimensional arguments, that increasing η at fixed B, is similar to increasing B at fixed η. If we measure any transition temperature T_c in units of $J_\perp$, then the dimensionless $T_c/J_\perp$ can only depend on the other dimensionless parameters of the model, the anisotropy $\eta = \lambda_z d/\lambda_\perp\xi_0$, and the vortex line density $f = B\xi_0^2/\phi_0 = (\xi_0/a_v)^2$. Since our London approximation ignores details of the vortex cores, if we consider the continuum limit of our model, $a_v \gg \xi_0$, we expect that $T_c/J_\perp$ should be at most weakly dependent [10] on the core radius ξ_0. The only combination of η and f that is independent of ξ_0 is $\eta^2 f$. Thus, the dominant dependence of $T_c/J_\perp$ on η and f can only be through some function of $\eta^2 f \sim \eta^2 B$.

We can further argue how transition temperatures should depend on the quantity $\eta^2 f$. In the limit of extreme anisotropy, $\eta \to \infty$, we have completely decoupled planes, and the transition temperature should be independent of η; thus we expect $T_c \sim J_\perp$. In the limit of a nearly isotropic system, $\eta \sim 1$, we expect that T_c should be independent of the spacing between planes d; thus we expect $T_c \sim J_\perp/\eta\sqrt{f} = (\phi_0^2/16\pi^3\lambda_\perp^2)(\lambda_\perp/\lambda_z)(\phi_0/B)^{1/2}$. These are in fact the predictions for the melting temperature based on Lindemann criterion calculations [2].

RESULTS

We now simulate the Hamiltonian (1), using periodic boundary conditions in all directions, on mesh sizes $L_\perp^2 \times L_z$. To test for superconducting coherence, we compute the helicity moduli $\Upsilon_\perp(T)$ and $\Upsilon_z(T)$ which measure the stiffness with respect to applying a net gradient ("twist") in the phase of the wavefunction along directions perpendicular and parallel to the applied magnetic field [7]. The helicity modulus in direction $\hat{\mu}$ is given by the phase correlation

$$\Upsilon_\mu(T) = \left\langle \frac{1}{L_\perp^2 L_z} \sum_{\langle ij\rangle} J_{ij}\cos(\theta_i - \theta_j - A_{ij})(\hat{\mathrm{e}}_{ij}\cdot\hat{\mu})^2 \right\rangle - \frac{1}{TL_\perp^2 L_z}\left\langle \left[\sum_{\langle ij\rangle} J_{ij}\sin(\theta_i - \theta_j - A_{ij})(\hat{\mathrm{e}}_{ij}\cdot\hat{\mu})\right]^2 \right\rangle, \qquad (4)$$

where $\hat{e}_{ij}$ is the unit vector from site i to j. $Y_\perp$ and Y_z are proportional to the density of superconducting electron pairs for currents flowing perpendicular and parallel to B. When Y_μ is positive, there is superconducting coherence in direction $\hat{\mu}$. When Y_μ vanishes, superconducting coherence is lost.

We also measure the specific heat of the system using the usual energy fluctuation formula. A peak in the specific heat locates the temperature at which, upon cooling, there is a dramatic freezing out of thermal fluctuations and the system looses the bulk of its entropy. We will take the location of the specific heat peak as indicating the cross-over temperature T_{c2} [11].

We carry out our simulations with a B yielding a fractional density of vortex lines $f = 1/15$. The ground state, shown in Fig. 1, is a nearly triangular vortex line lattice. Our runs are typically 10,000 sweeps through the mesh to equilibrate, followed by 128,000 sweeps to compute averages. These simulations are about 9 times longer than in our previous work [7].

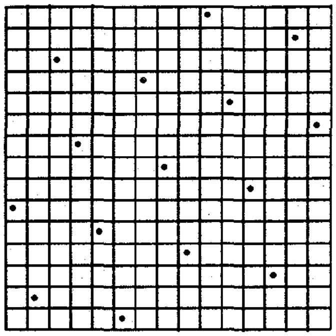

FIG. 1. Ground state locations of vortex lines in the xy plane for line density $f = 1/15$ on a cubic mesh. Vortices form a nearly triangular lattice with sides $\sqrt{18} \times \sqrt{18} \times \sqrt{17}$.

A sample of our results, for the case of $\eta = \sqrt{10}$ is shown in Fig. 2. We see that $Y_\perp$ vanishes at a $T_{c\perp}$ significantly lower than the T_{cz} where Y_z vanishes. We show data for heating and cooling, for three different mesh sizes, 15^3, 30^3, and $15^2 \times 120$. We see no appreciable hysteresis comparing heating and cooling, nor is there any apparent finite size effect as $L_\perp$ and L_z are varied. By computing the density-density correlation function of vortices in the xy plane, we identify $T_{c\perp}$ as locating the melting of the vortex line lattice [7].

For $T < T_{c\perp}$ we have an ordered vortex lattice which is commensurably pinned to the discrete mesh, resulting in a finite $Y_\perp$. For $T > T_{c\perp}$ we have a vortex line liquid of unpinned diffusing vortex lines; the resulting "flux flow" resistance drives $Y_\perp \to 0$. Between $T_{c\perp}$ and T_{cz} we have a vortex line liquid which retains superconducting coherence in the direction parallel to the applied magnetic field. These results are in complete agreement with our earlier simulations [7] on a similar *isotropic* model. In contrast to these earlier simulations however, we now see that, in agreement with experiment, both $T_{c\perp}$ and T_{cz} lie noticeably below the cross-over T_{c2} as determined by the specific heat peak.

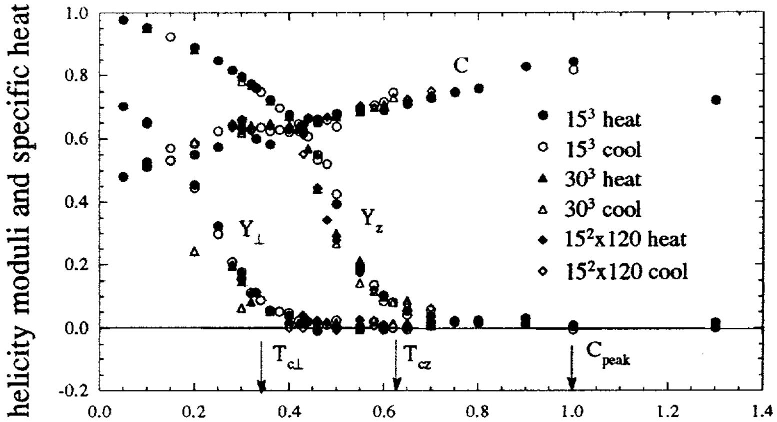

FIG. 2. Helicity moduli $Y_\perp$ and Y_z and specific heat C versus temperature T for anisotropy $\eta = \sqrt{10}$ and vortex line density $f = 1/15$. Heating and cooling for three different system sizes are shown. $Y_\perp$, Y_z, C, and T are all measured in units of $J_\perp$.

Carrying out simulations at other values η on a 15^3 size mesh, we show in Fig. 3 the resulting phase diagram in the $\eta - T$ plane. The $T_{c\perp}$ line locates the melting of the vortex line lattice. The T_{cz} line locates the loss of coherence parallel to the magnetic field. The line "C_{peak}" locates the peak of the specific heat, which we take as the cross-over temperature T_{c2}. For $T > T_{c2}$ we have the normal metal. For $T_{c2} > T > T_{cz}$ we have a vortex line liquid, with resistive behavior in all directions. For $T_{cz} > T > T_{c\perp}$ we have a vortex line liquid with superconducting coherence parallel to B. For $T_{c\perp} > T$ we have a pinned Abrikosov vortex line lattice.

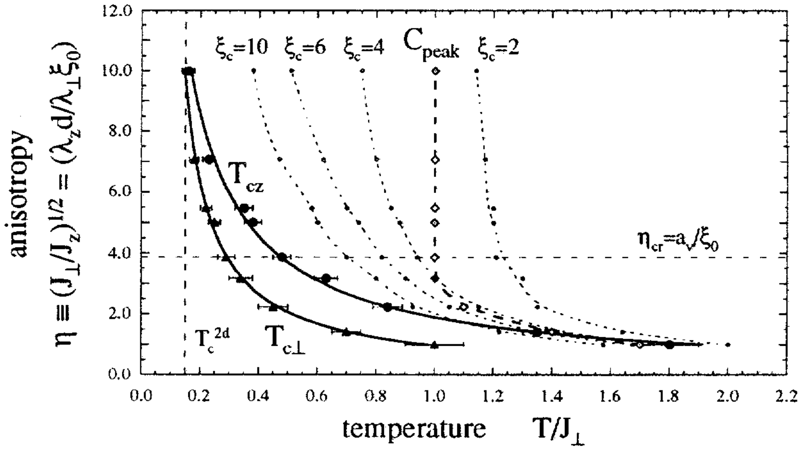

FIG. 3. Phase diagram in the anisotropy–temperature plane for vortex line density $f = 1/15$. T is measured in units of $J_\perp$ and ξ_c in units of d.

The solid phase boundary lines for $T_{c\perp}$ and T_{cz} are fits to a simple form $T = a + b/\eta$, as motivated by our discussion at the end of the preceding section. If we fit the lowest five data points (those for $\eta \leq \eta_{cr}$) to a power law, we find $T_{c\perp} \sim 1/\eta^{0.914}$ and $T_{cz} \sim 1/\eta^{0.966}$, in excellent agreement with our dimensional argument that characteristic temperatures at small η should scale as $T \sim 1/\eta$. We can also fit the melting temperature at these low η to the form predicted by a Lindemann criterion [2], $T_{c\perp} = 4c_L^2(\phi_0^2/16\pi^2\lambda_\perp^2)(\lambda_\perp/\lambda_z)(\phi_0/B)^{1/2} = 4\pi c_L^2 J_\perp/\eta\sqrt{f}$, where the Lindemann parameter $c_L^2 \equiv \langle u^2\rangle/a_v^2$ gives the average displacement of a vortex line from its equilibrium lattice position, at melting. We find $c_L = 0.14$. At large η, we see that $T_{c\perp}$ approaches a constant value T_c^{2d}, which we have found from independent simulations to be the melting temperature for an isolated two dimensional plane.

The cross-over from small to large η, where the discreteness of the layering along $\hat{\mathbf{z}}$ becomes important and one approaches the two dimensional limit, can be estimated, following our discussion at the end of the previous section, by the criterion $\eta_{cr}^2 f \simeq 1$, or, using $f = B\xi_0^2/\phi_0 = (\xi_0/a_v)^2$, as $\eta_{cr} = a_v/\xi_0$. Using an effective elastic medium approximation to describe vortex line fluctuations in the line lattice, one can show [2] that for $\eta < \eta_{cr}$, the dominant wavenumber q_z of fluctuations at melting satisfies the condition $d < \pi/q_z$, and hence the layering of the material is averaged over. For $\eta > \eta_{cr}$ however, the dominant wavenumber is at $d = \pi/q_z$, and layering is important. Some theoretical models [5] have predicted that η_{cr} will mark a dramatic change in behavior, reflecting a three dimensional to two dimensional cross-over. In Fig. 3 we indicate the cross-over η_{cr}. We see that the specific heat peak for $\eta > \eta_{cr}$ is independent of η. Thus at these high temperatures and anisotropies, our three dimensional system is behaving as effectively decoupled layers. However we see no dramatic change in behavior for $T_{c\perp}$ and T_{cz} as η_{cr} is crossed. In particular we continue to find $T_{cz} > T_{c\perp}$ for all $\eta > \eta_{cr}$.

An intriguing question concerning behavior in the vortex line liquid is how easily lines can cut through each other. This has important consequences for line diffusion. If lines cannot cut, they can be effectively pinned by their mutual entanglements [3,12]. To investigate this we have computed the average number of vortex line intersections, N_c, present in any instantaneous configuration of the system. An intersection is defined when two vortex lines enter and leave the same unit cell of the mesh, and corresponds to vortex lines with overlapping cores. Once two lines intersect, they are free to cut through each other, or even to detach and reconnect different ingoing and outgoing segments. We define the "cutting length" $\xi_c \equiv fL_\perp^2 L_z/N_c$ as the average distance (in units of d) along $\hat{\mathbf{z}}$ between cuts of the magnetic field induced vortex lines. ξ_c gives a crude measure of the average length over which a vortex line remains a well defined string, or equivalently a measure of the number of planes which remain correlated. In Fig. 3 we show contours of constant $\xi_c = 2$, 4, 6, and 10 in the $\eta - T$ plane. We see that planes are essentially uncorrelated at temperatures above the specific heat peak. Correlations grow as one starts to cool below the specific heat peak towards T_{cz}, but cutting remains relatively frequent throughout most of the vortex line liquid.

DISCUSSION

We have computed the phase diagram of a fluctuating type II superconductor in the anisotropy temperature plane. Our results are consistent with general experimental observations, that vortex lattice melting occurs well below the cross-over T_{c2} associated with the formation of local superconducting order. Our melting curve agrees well with that predicted by the Lindemann criterion. No dramatic change in critical behavior is seen at the so-called 3d-2d cross-over anisotropy η_{cr}. We find that vortex line cutting can occur over most of the vortex line liquid region. From our earlier isotropic simulations [7] we believe that cutting can be frozen out on long time scales only for $T < T_{cz}$.

We find a new distinct transition T_{cz}, inside the vortex line liquid [13]. For $T_{c\perp} < T < T_{cz}$ we have a vortex line liquid with superconducting coherence parallel to the applied magnetic field. Recent "flux transformer" experiments [14,15] on YBCO single crystals show that there is a temperature "T_{th}" below which vortex line correlations parallel to B become comparable to the thickness of the sample. "T_{th}" is clearly found to be above the "T_{irr}" where resistivity transverse to B vanishes. Resistivity parallel to B however appears to vanish at "T_{th}". A phenomenological fit [14] shows that the region over which correlations parallel to B grow, extends over the entire region between T_{c2} and "T_{th}". If we identify "T_{th}" with our T_{cz}, T_{irr} with our $T_{c\perp}$, and T_{c2} with our specific heat peak, our results are in complete accord with these experimental finding. These experiments on YBCO are carried out in the "3d" region corresponding to $\eta^2 f < 1$. Similar results in the "2d" region $\eta^2 f > 1$ have been reported in artificial MoGe/Ge multilayers [16].

By consideration of other properties of the vortex line system, such as vortex density-density correlation function, density of thermally activated vortex rings, and vortex winding, the picture we have formed of transitions in the anisotropic vortex line system is as follows [7]. Upon heating, the vortex line lattice melts into a vortex line liquid, in which vortex lines maintain a well defined identity in passing down the thickness of the system. As T increases, transverse fluctuations increase, and thermally excited vortex rings appear between adjacent xy planes. At T_{cz} these rings have so proliferated that they link up all the magnetic field induced vortex lines into a percolating tangle; one can find a connected path of vortex line segments that travels completely around the system in the direction transverse to the applied magnetic field. As T increases, the correlations between planes decreases, and each plane behaves more like an uncoupled two dimensional liquid of point vortices. Finally, as T_{c2} is reached, thermally excited vortex rings may now pierce the xy planes, creating the analog of vortex-antivortex pairs in a 2d layer. The proliferation of these rings leads to an explosion of vorticity in the planes, destroys the local fluctuating superconducting wavefunction in the plane, and results in the cross-over to the normal metallic state.

ACKNOWLEDGMENT

This work has been supported by the U.S. Department of Energy under grant DE-FG02-89ER14017.

REFERENCES

[1] M. Tinkham, *Introduction to Superconductivity*, (R.E. Krieger Co., Malabar, FL, 1980).

[2] D. S. Fisher, M. P. A. Fisher, and D. A. Huse, Phys. Rev. B **43**, 130 (1991).

[3] D. R. Nelson and H. S. Seung, Phys. Rev. B **39**, 9153 (1989).

[4] A. Houghton, R. A. Pelcovits and A. Sudbø, Phys. Rev. B **40**, 6763 (1989); E. H. Brandt, Phys. Rev. Lett. **63**, 1106 (1989).

[5] L. I. Glazman and A. E. Koshelev, Phys. Rev. B **43**, 2835 (1991).

[6] T. K. Worthington, F. H. Holtzberg and C. A. Field, Cryogenics **30**, 417 (1990); U. Welp, W. K. Kwok, G. W. Crabtree, K. G. Vandervoort and J. Z. Liu, Phys. Rev. Lett. **62**, 1908 (1989).

[7] Y.-H. Li and S. Teitel, Phys. Rev. B **47**, 359 (1993) and *ibid.* **49**, 4136 (1994).

[8] D. S. Fisher in *Phenomenology and Applications of High Temperature Superconductors*, edited by K. Bedell *et al.* (Addison-Wesley, Reading, MA, 1992), p.287.

[9] Recently we have suggested that differences between the uniform B model and a more exact treatment may also appear once the sample thickness is large compared to the length $\phi_0^2/8\pi T_m \simeq 1400\mu m$ (T_m is the vortex lattice melting temperature). Experimental samples however are typically thinner than this. See, T. Chen and S. Teitel, Phys. Rev. Lett. **74**, 2792 (1995).

[10] The interactions between different vortex lines are independent of the core size ξ_0. However the self interaction of a bending vortex line can depend on ξ_0. This may lead to weak logarithmic dependencies on ξ_0. See E. H. Brandt, J. Low Temp. Phys. **26**, 735 (1977).

[11] Because B is kept uniform and constant in our model, equivalent to a $\lambda_\perp \to \infty$ approximation, we cannot directly measure the magnetization in our system.

[12] M. C. Marchetti and D. R. Nelson, Phys. Rev. B **42**, 9938 (1990) and Physica C **174**, 40 (1991); S. P. Obukhov and M. Rubinstein, Phys. Rev. Lett. **65**, 1279 (1990) and *ibid.* **66**, 2279 (1991).

[13] M. V. Feigelman, Physica A **168**, 319 (1990); M. V. Feigelman, V. B. Geshkenbein and V. M. Vinokur, JETP Lett. **52**, 546 (1990); M. V. Feigelman, V. B. Geshkenbein, L. B. Ioffe, and A. I. Larkin, Phys. Rev. B **48**, 16641(1993).

[14] H. Safar, P. L. Gammel, D. A. Huse, S. N. Majumdar, L. F. Schneemeyer, D. J. Bishop, D. López, G. Nieva, and F. de la Cruz, Phys. Rev. Lett. **72**, 1272 (1994).

[15] F. de la Cruz, D. López, and G. Nieva, Phil. Mag. B **70**, 773 (1994); D. López, G. Nieva, and F. de la Cruz, Phys. Rev. B **50**, 7219 (1994).

[16] D. G. Steel, W. R. White and J. M. Graybeal, Phys. Rev. Lett. **71**, 161 (1993).

SYSTEMATIC PROCESS SYNTHESIS AND DESIGN METHODS FOR COST EFFECTIVE WASTE MINIMIZATION

Lorenz T. Biegler
Ignacio E. Grossmann
Arthur W. Westerberg

Dept. of Chemical Engineering
and the Engineering Design Research Center
Carnegie Mellon University
Pittsburgh, PA 15213

ABSTRACT

We present progress on our work to develop synthesis methods to aid in the design of cost effective approaches to waste minimization. Work continues to combine the approaches of Douglas and coworkers and of Grossmann and coworkers on a hierarchical approach where bounding information allows it to fit within a mixed integer programming approach. We continue work on the synthesis of reactors and of flexible separation processes. In the first instance, we strive for methods we can use to reduce the production of potential pollutants, while in the second we look for ways to recover and recycle solvents.

INTRODUCTION

We summarize progress made on the following topics which we are pursuing in this work.

1. Integration among design levels for process synthesis in order to develop cost effective waste minimizing processes.
2. Quantitative targeting approaches for the synthesis of reactor networks
3. Synthesis of nonideal separation sequences for byproduct recovery and reuse.

MULTILEVEL SYNTHESIS OF PROCESS FLOWSHEETS

The main objective of this project has been to develop a new framework for the synthesis of total processing systems that can address the issue of generation of superstructures and optimization under a methodology that combines preliminary screening and MINLP optimization. This challenge was in fact proposed by the late David Rippin at the session on process synthesis at the FOCAPD Meeting in 1989.

The basic question that we have addressed over the past year is how to develop a search procedure that avoids solving a single flat MINLP that contains all the alternatives of interest for a process flowsheet, and that in principle is capable of producing the same result as if the single MINLP had been solved at once. The emphasis in this work has been on the development of a design methodology that integrates thermodynamic analysis (mostly second law analysis), the hierarchical decomposition by Douglas and the MINLP optimization developed by our group at Carnegie Mellon.

To provide a conceptual basis for our work we had developed in our previous work an abstract mathematical model for characterizing aggregated models. These models are higher level representations that are given in terms of algebraic relations for equations and variables that guarantee bounding properties with respect to the original problem. These aggregated models must be derived for each problem at hand, but one particularly useful framework is the one that relies on thermodynamic analysis as described below. Given aggregated models at various level of abstraction and that obey bounding properties, the question that arises is how to integrate these within a multilevel strategy for flowsheet synthesis.

We have developed a multilevel synthesis strategy that can be viewed as a hierarchically driven tree enumeration in which simultaneous optimization models at increasing levels of detail are considered for predicting bounds on the profit. The basic idea for the enumeration consists of applying a hierarchical decomposition that involves four major levels: input/output, reaction, separation and heat integration.

Rather than relying directly on Douglas' procedure, our approach consists of a branch and bound search coupled with aggregated or "black box" models that through their predicted bounds allow us to eliminate many alternatives in the search. The aggregated models consist of higher level representations that are physically based and that make use of stoichiometry and thermodynamic analysis. The basic idea is to combine high level or black box models with superstructure optimization models. In particular, at the input/output level thermodynamic availability is considered to estimate a lower bound for the energy requirements in addition to minimum material flows. At the reaction level, a superstructure model is considered together with thermodynamic models for separation and heat integration. At the separation level the reactor network is fixed while the heat integration is treated as a "black box" using the Duran and Grossmann model. Finally, at the heat integration level a fixed flowsheet is considered with a superstructure for a heat exchanger network. Note that each level gives rise to a simultaneous optimization model at different levels of complexity. Normally at the input/output level the optimization problem corresponds to an NLP subproblem, while at the heat integration level it corresponds to an MINLP problem.

The search of the optimal flowsheet involves the multiple levels within a rigorous tree search whose terminal nodes correspond to feasible NLP solutions of the flowsheet. One advantage of this strategy is that it involves the solution of NLP and MINLP subproblems which are much smaller than the original MINLP problem. The potential drawback is that the number of subproblems to be solved can be rather large. We tested this strategy with the HDA process by Douglas. In a restricted version of this problem, our proposed method required the enumeration of only few nodes. Furthermore, the predicted upper bounds on the profit were rather tight. This is due to the anticipation of energy requirements at the higher levels of decision (e.g. input-output structure). Shown in the figure below is the flowsheet obtained from the proposed method.

Mark Daichendt, the student working on this project is finalizing the writing of his Ph.D. thesis. The manuscript of this work [1] is currently under preparation. The next major step in this project is the integration of operational considerations as part of this design methodology.

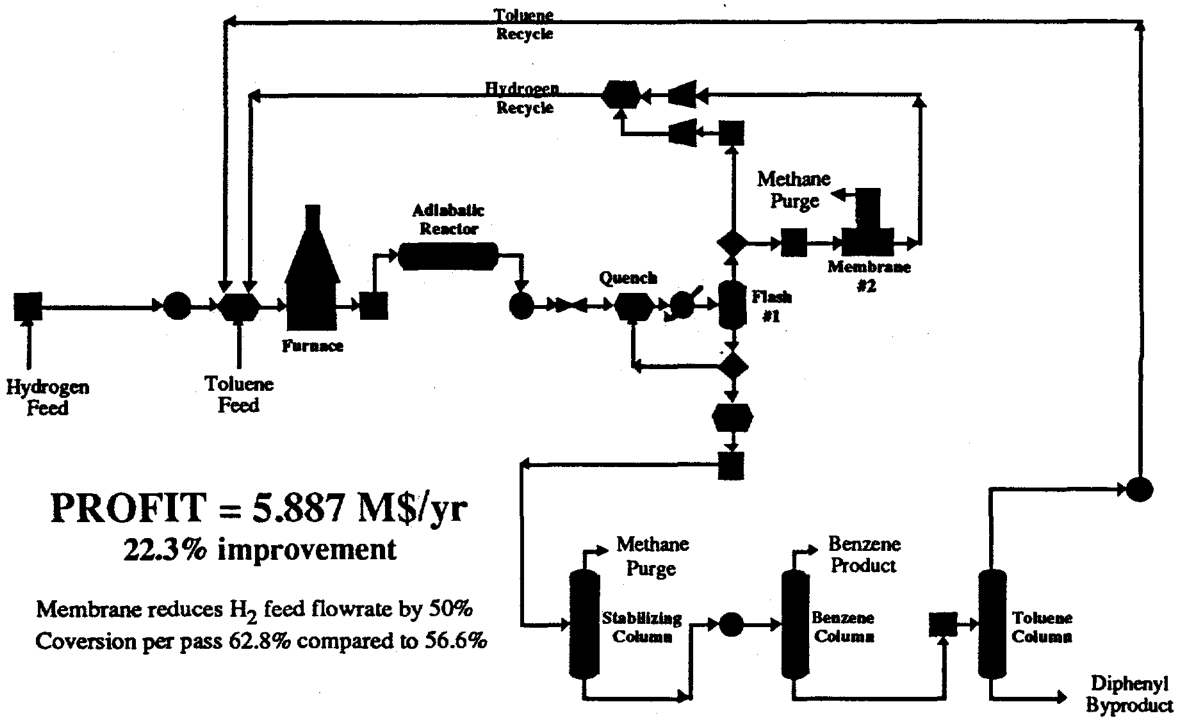

PROFIT = 5.887 M$/yr
22.3% improvement

Membrane reduces H_2 feed flowrate by 50%
Coversion per pass 62.8% compared to 56.6%

Figure 1. HDA process synthesized using proposed method

REACTOR NETWORK SYNTHESIS FOR WASTE MINIMIZING PROCESSES

The public is demanding processes that are environmentally benign. One of the most efficient approaches to designing such processes is to increase raw material conversion to product rather than wasteful byproducts. In this work we consider the development and application of optimization-based process synthesis tools to improve reactor and separation process performance to improve the environmental characteristics of processes.

We apply systematic process synthesis approaches to the design of the reactor network to maximize the overall conversion to useful product and thus minimize harmful byproducts. This approach is based on concepts of attainable regions in concentration space and is supported by powerful, large-scale optimization tools. Examples that can benefit from this approach are processes for the manufacture of chlorinated hydrocarbons especially allyl chloride and vinyl chloride, two high volume polymer intermediates. The improvements made by this approach can also validated by rigorous process simulation models.

We use these approaches to improve both economic and environmental performance. Specifically we describe recently developed techniques for process synthesis and extend them to consideration of reactor networks and their interaction with other process subsystems.

The nature of the reaction mechanism and the resulting reactor design frequently determines the entire character of a chemical process. Once a kinetic route is chosen and a quantitative (not necessarily a mechanistic) rate law has been established, the flow pattern, mixing characteristics and rates of heat addition or removal have a strong influence on product yield and selectivity. The reactor effluent then determines the downstream separation sequence which then impacts on the energy network. More importantly, the generation of hazardous waste is almost always the result of the characteristics of the reactor network.

Over the past three decades process synthesis methodologies for heat exchanger and separation systems have seen considerable research activity. Many of the resulting synthesis methods are either rule-based or graphical techniques driven by physical insights; others can be formulated as well-characterized optimization problems. For example, efficient synthesis methods based on pinch technology have been established for heat exchanger networks [2]; design of simple separation networks has been formulated as a structural optimization problem and azeotropic separation sequences can be synthesized through phase plane analysis (see next section). However, relatively little research has been done for reactor network synthesis. Here well-known heuristics for single reactions or series-parallel systems [3, 4] may yield inconsistent or conflicting results when dealing with more complex systems. On the other hand, quantitative optimization approaches lead to difficulties as a result of nonlinear reactor models (frequently described by partial differential equations) and in solving large, nonconvex optimization problems.

A much more efficient approach was recently developed, based on the construction of an attainable region [5]. This approach uses geometric properties to find a region in concentration space that cannot be extended by further reaction or mixing. Once known, the determination of the optimum point is greatly simplified. Construction of the attainable region is accomplished by analyzing the rate vector field and determining a surface that is a) convex (all points can be mixed),, b) has no rate vectors pointing out of the region (cannot be extended by further reaction), and c) no rate vectors external to the region can be reversed back into the region (cannot be extended by a mixed reactor). Thus, a simple graphical approach can been used to derive superior reactor networks; this approach has been demonstrated for numerous reaction mechanisms.

The attainable region can be constructed efficiently in two and even in three dimensions [6], but, for larger reaction systems, a graphical approach has clear limitations. As a result, Balakrisnan and Biegler [7] adapted these attainable region concepts so that they can be formulated as small nonlinear optimization problems for reaction mechanisms of any dimension. Consequently, optimal reactor networks can now be synthesized for arbitrarily complicated reaction mechanisms, through small and inexpensive optimization problems. This approach has also been extended to nonisothermal systems [8] with only slightly more complicated optimization problems. Finally, Lakshmanan and Biegler [9] recently considered this approach for the synthesis of waste minimizing processes. In addition, refinements of this optimization-based approach using a compact MINLP strategy have been presented recently by Lakshmanan and Biegler [10].

While construction of the reactor network is not difficult from the boundary of the attainable region, the attainable region itself also provides information on the performance of the reactor network without explicitly constructing it. Instead, compact optimization formulations can be used to target reactor performance, and these can be embedded into larger process systems. For instance, an attainable region formulation can be substituted for a complex reactor model, and this can be coupled to the recycle and separation network as well as a heat exchanger network. By combining these systems, a resulting optimization formulation can exploit the interactions and the synergy among these subsystems, and far better processes can result. Balakrishna and Biegler [8, 11] have shown how this approach can be coupled to heat exchanger network and separation synthesis formulations with the result that very complex flowsheets can be synthesized and optimized simultaneously.

The waste minimization problem also forms an important component to be addressed by reactor targeting and here we also include the waste treatment step into the synthesis procedure. In our research we apply these synthesis techniques to processes for reaction mechanisms and rate laws that are well-known. As an example we consider a simple (allyl chloride) Van de Vusse process to illustrate the reactor targeting approach and demonstrate its potential.

Example Problem

Consider the simplified allyl chloride process shown in Figure 2. Propylene and chlorine are mixed and reacted at high temperature to allyl chloride, hydrogen chloride and dichlorinated byproducts. The reactor effluent is flashed to separate the unreacted propylene and chlorine and hydrogen chloride from the reaction products. This mixture is sent to a scrubber to recover the hydrogen chloride and recycle the reactants. On the other hand, the reaction products, allyl chloride, dichloropropene and dichloropropane, are further separated downstream and the dichlorinated compounds are discarded. The reaction can be described by rate expressions from Groll and Hearne [12] and, if chlorine is assumed in excess, the system follows van de Vusse kinetics: A --> B --> C, A --> D where A, B, C, and D are propylene, allyl chloride, dichloropropene and dichloropropane, respectively. This process is well-characterized and has been the subject of numerous studies [13, 14].

This process was modeled in GAMS, an optimization/modeling platform, using the targeting concepts explained above along with simplified separation models. The resulting formulation consists of 542 constraints and 523 variables and was solved in 3.0 CPU sec's on an HP 9000/720 workstation. Here it turns out that the optimal reactor network is a tubular reactor (as in practice) but with the falling temperature profile shown in Figure 3 (as opposed to the adiabatic profile used in practice). This falling profile can also be used to exploit the heat of reaction elsewhere in the process. While this is frequently done, the heat recovery network is usually constructed sequentially, without changing process conditions to its advantage. In fact, if we are able to synthesize the heat exchanger network simultaneously with the reactor system, the overall profit can be increased by over 90%. A comparison of the sequential and simultaneous optimization is given in Table 1. Note that the overall conversion of propylene to allyl chloride increases from 49.6% to 61.5%. This results from a higher selectivity to main product vs. waste, lower conversion per pass, higher recycle and lower feed requirements.

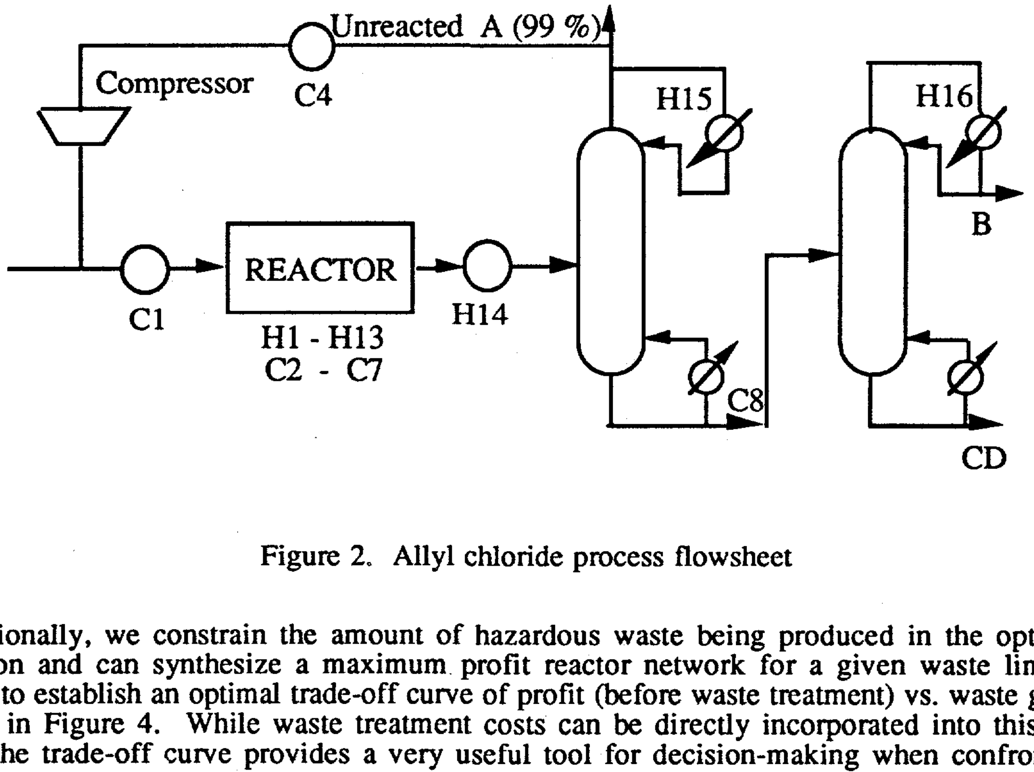

Figure 2. Allyl chloride process flowsheet

Additionally, we constrain the amount of hazardous waste being produced in the optimization formulation and can synthesize a maximum profit reactor network for a given waste limit. This allows us to establish an optimal trade-off curve of profit (before waste treatment) vs. waste generated, as shown in Figure 4. While waste treatment costs can be directly incorporated into this problem directly, the trade-off curve provides a very useful tool for decision-making when confronted with uncertain waste treatment costs and changing regulations.

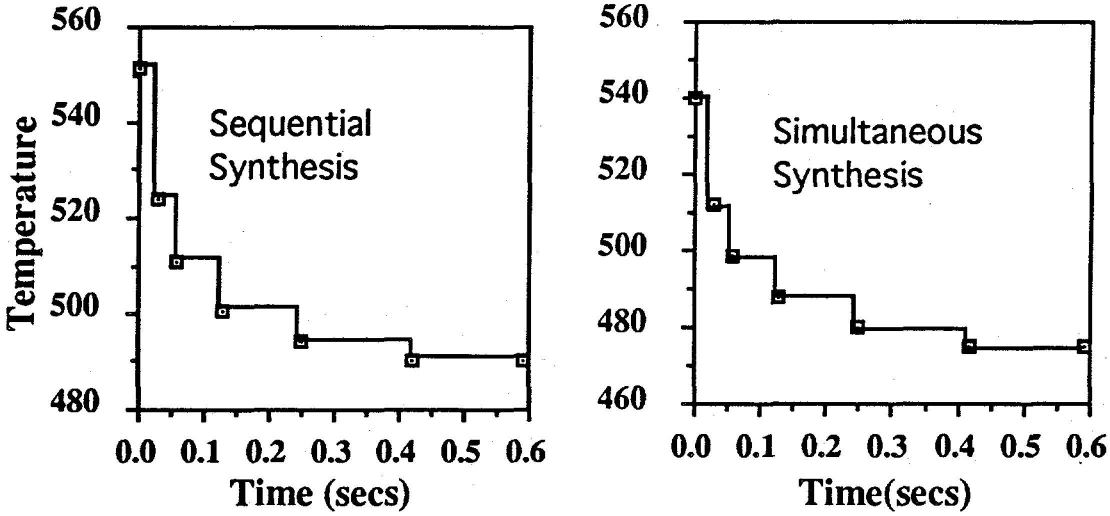

Figure 3: Reactor temperature profiles

Table 1. Comparison between sequential and simultaneous optimizations

	Sequential	Simultaneous
Overall Profit	$38.98 * 10^5$ \$/yr	$74.02 * 10^5$ \$/yr
Overall Conversion	49.6 %	61.55 %
Hot utility load	$3.101 * 10^5$ BTU/hr	$2.801 * 10^5$ BTU/hr
Cold utility load	$252.2 * 10^6$ BTU/hr	$168.5 * 10^6$ BTU/hr
Fresh Feed A	$8.057 * 10^4$ lb/hr	$6.466 * 10^4$ lb/hr
Degraded Product C	$3.112 * 10^4$ lb/hr	$1.44 * 10^4$ lb/hr
By-Product D	$0.933 * 10^4$ lb/hr	$1.00 * 10^4$ lb/hr
(Recycled) A	$1.22 * 10^4$ lb/hr	$1.963 * 10^4$ lb/hr

As future work we plan to consider and further develop the following topics:

- development of large-scale nonlinear programming tools for optimization formulations based on differential-algebraic models.
- advanced software environments for the rapid development and prototyping of reactor and process models
- development and enhancement of fundamental concepts for reactor targeting and extension to separation and waste treatment systems
- access to rigorous process models embedded within the ASPEN simulator as well as the CRDT reactor design program.

A major goal of our research will be the demonstration and refinement of an optimization-based process synthesis methodology for waste minimization of important chemical processes. Process models developed in ASPEN and CRDT along with the optimization formulations for reactor targeting can then be developed for more rigorous process evaluation.

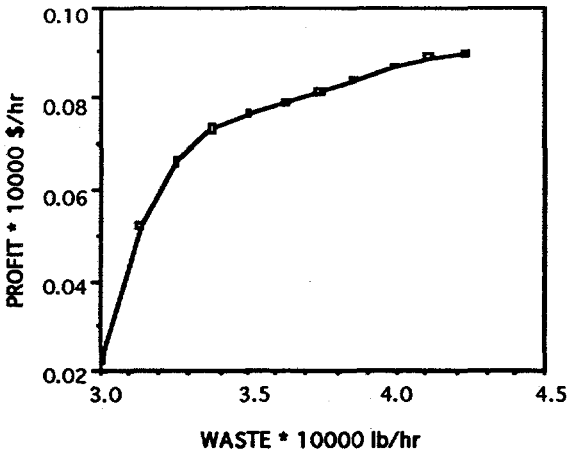

Figure 4: Allyl Chloride trade-off curve (noninferior curve)

SYNTHESIS OF NONIDEAL SEPARATION SEQUENCES FOR BYPRODUCT RECOVERY AND REUSE.

We have been working on methods to synthesize separation processes for liquid mixtures displaying azeotropic and liquid/liquid behavior since 1989. In this work we developed SPLIT, an expert system for the synthesis of such processes [15, 16, 17, 18]. We also developed many insights for separating mixtures that allowed, for example, the prediction of the all the reachable products that a conventional and an extractive three component distillation column can produce, where the operation of the column ranged from total reflux to reversible [19, 20, 21]. The pinch trajectories corresponding to reversible operation allowed the computation of how far column operation can cross the so-called residue and distillation curve boundaries. These trajectories can be very rich -- having multiple branches.

The computations to support each decision in the synthesis of separation processes for azeotropic mixtures are very extensive, causing us to term this approach "analysis-driven synthesis."

Synthesis of batch separation processes for azeotropic mixtures

We have recently extended the insights for continuous distillation processes to batch distillation-based processes [22]. In the course of developing these insights, we investigated unconventional batch column configurations such as those shown in Figure 5. The leftmost is a conventional batch still with a pot at the bottom. The second is a top pot column where the condenser has large holdup and one draws off a bottom product. The third is the most interesting and is a batch column with a center stage holdup. It has both a stripping and an enriching set of trays. It can be run with either heating or cooling of the pot. As Morari and coworkers [23] reported, this configuration cuts utility use in half (generally not economically significant, but interesting). It also allows one to double the throughput, making essentially two cuts in the time a conventional column can make one (more significant economically), but, of coure, it will be more expensive to purchase. We also show an optional extractive agent feed in the top section of the column. The fourth is a conventional batch column with an extractive agent fed continuously as one carries out the separation. We can break azeotropes with the last two configurations.

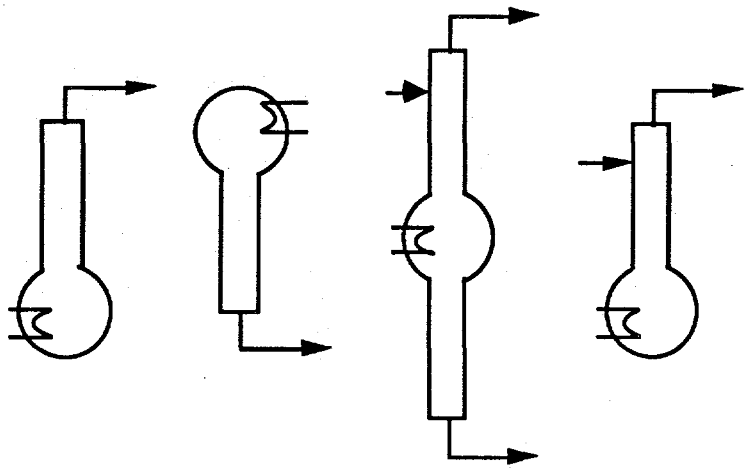

Figure 5. Conventional and unconventional batch columns

We are working on comparing the optimal operation as found using optimal control to how we would predict one should operate such a column using the above insights, where the insights give bounds on the solvent flow vs. reflux ratio vs. the amount of material separated [24].

Flexible separation processes

The recovery of solvents from processes is an important environmental problem. If several processes at a single site share a single solvent recovery system, then we find the need to design such a system to operate with a variety of potential feed compositions and flow rates.

Collocation models: To carry out the synthesis of flexible separation systems, we identified the need to reduce the analysis burden, especially to determine the detailed behavior of a column. We often needed to solve tray-by-tray models. Unfortunately these computations involve fixing the number of trays in each of the column sections and guessing the reflux ratio to use to effect a desired separation. It is difficult to know the number of trays and a suitable reflux a priori.

Based on work by others [25, 26, 27], we [28] developed a collocation model for distillation. Such models have had difficulty in producing accurate composition profiles when portions of the profiles flattened out, as in a column where there are too many trays or where one seeks high purity. We introduced two variable transformations to our collocation model. The first maps trays ranging in number from zero to infinity onto the range zero to one:

$$z = 1 - e^{-as}$$

where z is the transformed stage location and s is the original tray number. The second transformation mapped composition from the range zero to one into the range minus infinity to plus infinity:

$$-1 \leq 2(x - 0.5) = \tanh(\xi) = \frac{e^{\xi} - e^{-\xi}}{e^{\xi} + e^{-\xi}} \leq 1$$

where x is composition and ξ is the transformed composition. Both change the shape of the column profiles to those more easily characterized by low order polynomials.

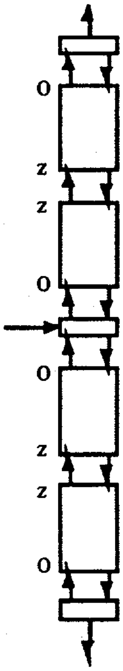

Figure 6. Reduced order column model

Our collocation model involves a feed tray, a condenser, a reboiler and two tray stacks, as shown in Fig. 6. We models the tray stacks as two opposing collocation sections, where the transformed tray number z is zero at the opposing ends of each section and nonzero where they merge. Testing of this model on several example problems, where the components range from displaying ideal to azeotropic behavior, shows it compares very favorably to that obtained using tray-by-tray computations, even for cases for sharp separation and too many trays. We have developed a robust computation method that creeps up on the solution (continuation for degree of separation and model refinement to move from ideal to nonideal equilibrium models).

Flexible design: We have used this model for column design and optimization. Our latest use is for the design of a single flexible column. We defined flexible operation as being able to operate at steady-state with any one of a given set of alternative feeds to the column. The designer sets the fraction of time each feed will exist for the column so we can compute appropriate operating costs relative to capital costs.

A conventional optimization code fails to simultaneously converge a column model and move to an optimum solution. We therefore use a grid of nine column designs -- using our robust procedure to creep up on the solutions for each column, one for each feed. For each feed we fit a quadratic polynomial to characterize a column's reflux ratio vs. total trays and feed tray location. The optimization code has no difficulty with this very reduced model in finding the optimal diameter and total number of trays for the column. It also picks which tray to feed and what reflux rate to use to operate the column for each feed.

If the optimal design is at the edge of the nine grid points used to characterize the model, we compute more column designs to place that point interior to the grid and repeat Tests include both nearly ideal and azeotropic mixtures.

Future work on flexible separation process synthesis: To design flexible complete processes comprising several columns, we are examining setting up a superstructure model for separating feeds from anywhere in a composition diagram using the ideas presented recently by Sargent [29]. He treats each azeotrope as a new species. For each distillation region, he puts the bounding components (pure and azeotropic) into an order that corresponds to their volatility and develops a superstructure for separating them. Curvature of the distillation boundary influences possible products. His rules also suggest where recycling should be allowed. We shall attempt to optimize this superstructure using the design approach we developed earlier for a single flexible column. We are also examining the potential of using A-teams [30] as an approach to carrying out the optimization. Our concern is that the optimization of superstructures is likely to have multiple local optima, a problem that A-teams may address effectively.

REFERENCES

1. Daichendt, M. and I.E. Grossmann, "Combined Hierarchical Decomposition and Mathematical Programming for the Synthesis of Process Flowsheets", manuscript under preparation (1995).
2. Linnhoff, B. and E. Hindmarsh, "The Pinch Design Method for Heat Exchanger Networks", Chem. Eng. Sci., 38, 745 (1983)
3. Levenspiel, O. Chemical Reaction Engineering, John Wiley, New York (1962)
4. Fogler, H. S., Elements of Chemical Reaction Engineering, Prentice-Hall, Englewood Cliffs, NJ (1992)
5. Glasser, D., C. Crowe, and D. Hildebrandt, "A Geometric Approach to Steady Flow Reactors: The Attainable Region and Optimization in Concentration Space," I&EC Res., 26(9),1803 (1987)
6. Hildebrandt, D. and D. Glasser, "The Attainable Region and Optimal Reactor Structures," Proc. ISCRE Meeting, Toronto (1990)
7. Balakrishna, S. and L. T.. Biegler, "Constructive Targeting Approaches for Synthesis of Chemical Reactor Networks," I & EC Research, 31, p. 300 (1992).
8. Balakrishna, S. and L. T. Biegler, "Targeting Strategies for the Synthesis and Heat Integration of Nonisothermal Reactor Networks" I & EC Research, 31, 9, p. 2152 (1992)
9. Lakshmanan, A. and L. T.. Biegler, "Reactor Network Targeting for Waste Minimization," submitted for publication (1994a)
10. Lakshmanan, A. and L. T.. Biegler, "An Improved MINLP formulation for Reactor Network Synthesis," presented at Annual AIChE meeting, San Francisco (1994b)
11. Balakrishna, S. and L. T. Biegler, "A Unified Approach for the Simultaneous Synthesis of Reaction, Energy and Separation Systems," I & EC Research, 32, p. 1372 (1993)
12. Groll, H. P. A., and G. Hearne, "Reaction of Vinyl Type Monochalides with Halogen," US Patent 2,060,303, Nov. 10 (1939).
13. Shell Chemical Corporation, "Allyl chloride and other allyl halides." Instituut voor Toegepaste Sociologie te Nijmegen, New York (1949)
14. McKetta, J. J. (ed.), Encyclopedia of Chemical Processing and Technology, 5th ed., Marcel Dekker, New York (1991)
15. Wahnschafft, O. M., T. P. Jurain and A. W. Westerberg, "SPLIT: a Separation Process Designer," Comput. Chem. Engng, 15, No. 8, 565-581 (1991).
16. Wahnschafft, O. M., J. P. LeRudulier, P. Blania and A. W. Westerberg, "SPLIT: II. Automated Synthesis of Hybrid Separation Systems" Computers Chem Engng, ESCAPE-I Supplement, pp S305-S312 (1992b).
17. Wahnschafft, O. M., J. P. LeRudulier and A. W. Westerberg, "A Problem Decomposition Approach for the Synthesis of Complex Separation Processes," Ind. Eng. Chem. Res., Vol. 32, 1121-1141 (1993a).
18. Wahnschafft, O. M., J. W. Koehler and A. W. Westerberg, "Homogeneous Azeotropic Distillation: Analysis of Separation Feasibility and Consequences for Entrainer Selection and Column Design," ESCAPE III Supplement, Comput. Chem. Engng, Vol. 18, S31-S35 (1993b).
19. Wahnschafft, O. M., J. W. Koehler, E. Blass and A. W. Westerberg, "The Product Composition Regions of Single-Feed Azeotropic Distillation Columns," I&EC Res, 31(10), 2345-2361 (1992a).
20. Wahnschafft, O. M., and A. W. Westerberg, "The Product Composition Regions of Azeotropic Distillation Columns: 2. Separability in Two-Feed Columns and Entrainer Selection," , Ind. Eng. Chem. Res., Vol. 32, 1108-1120 (1993).
21. Westerberg, A. W., and O. M. Wahnschafft, The Synthesis of Distillation-based Separation Systems, 124 page review submitted to Advances in Chemical Engineering (1995).
22. Safrit, B., U. Diwekar, O. M. Wahnschafft, A. W. Westerberg, "Extending Continuous Conventional and Extractive Distillation Insights to Batch Distillation," submitted (1994).

23. Meski, G. A.., and M. Morari, "Batch Distillation in a Column with a Middle Vessel," paper 152a, AIChE Annual Meeting, St. Louis, MO (1993).
24. Safrit, B., A. W. Westerberg, U. Diwekar, O. M. Wahnschafft, "Improved Operational Policies for Batch Extractive Distillation Columns," paper 82e, AIChE Spring National Meeting, Houston, TX (1995).
25. Cho, Y. S. and B. Joseph, "Reduced Order Steady-state and Dynamic Models for Separation Processes," AIChE J, 29, 261-269, 270-276 (1983)
26. Stewart, W. E., K. L. Levien, and M. Morari, "Collocation Methods in Distillation," in Westerberg, A. W., and H. H. Chien (eds.), Proc. Second Int'l Conf. Foundations Computer Aided Process Design (FOCAPD83), CACHE Corp., Ann Arbor, MI, pp535-569 (1984).
27. Seferlis, P., and A. N. Hrymak, "Reduced Order Models for Distillation Optimization" paper 152m, Annual AIChE Meeting, Los Angeles, CA (1991).
28. Huss, R. S., and A. W. Westerberg, "Collocation Methods for Distillation Design, paper 131c, Annual AIChE Meeting, San Francisco (1994).
29. Sargent, R. W. H., "A Functional Approach to Process Synthesis and its Application to Distillation Systems, manuscript from Centre for Process Systems Engineering, Imperial College of Science, Technology and Medicine, London SW7 2BY, UK (1994).
30. Talukdar, S., and P. de Souza, "Insects, Fish and Computer-based Super-agents," paper from Engineering Design Research Center, Carnegie Mellon University, Pittsburgh, PA 15213 (1995).

INTEGRATED APPROACHES TO THE APPLICATION OF ADVANCED MODELING TECHNOLOGY IN PROCESS DEVELOPMENT AND OPTIMIZATION

R. J. Allgor, W. F. Feehery, J. E. Tolsma, L. B. Evans, and P. I. Barton[‡]
Department of Chemical Engineering and Energy Laboratory
Massachusetts Institute of Technology
Cambridge, MA 02139

ABSTRACT

The batch process development problem serves as good candidate to guide the development of process modeling environments. It demonstrates that very robust numerical techniques are required within an environment that can collect, organize, and maintain the data and models required to address the batch process development problem. This paper focuses on improving the robustness and efficiency of the numerical algorithms required in such a modeling environment through the development of hybrid numerical and symbolic strategies.

1 INTRODUCTION

Over the past twenty five years process modeling technology has emerged as an invaluable and widely used tool for the solution of many problems in process design and operation [1]. A major current trend in this technology is the evolution of equation-based simulation tools, such as SpeedUp [2], ASCEND [3], POLYRED [4], or ABACUSS [7], into *process modeling environments* in which a common reusable process model may be used reliably for a variety of different computational tasks, such as steady-state and dynamic simulation, steady-state and dynamic optimization, data reconciliation and parameter estimation, etc. [6]. Concurrently to these advances in the underlying technology, it is necessary to investigate the complex process design tasks that might be addressed by such software. In this context, we can envision sophisticated software environments that can collect, organize, and maintain the data and models required to address complex design problems, and facilitate the seamless application of numerical algorithms to steps in the solution of the overall problem.

A process design task that serves as a good candidate for this approach is the batch process development problem recently formalized by Allgor *et al.*[5]. In the specialty chemical and pharmaceutical industries, major competitive advantages can be derived from the rapid development of efficient batch processes with low environmental impact. Allgor *et al.*[5] present an industrial case study in which the combined discrete/continuous simulation capabilities of ABACUSS [7] are used to develop a process design significantly more efficient than that resulting from a direct implementation of pilot scale experiments in the large scale plant. A prototype methodology in which process modeling technology is employed for batch process development is also presented.

Our current research is addressing two major issues in refining this methodology and making it accessible to the practicing engineer: development of a suitable software environment, Batch

---

[‡] Author to whom correspondence should be addressed.

Developer, that implements this methodology and coordinates the overall process development, and further developments of the underlying process simulation and optimization technologies driven by the challenging problems posed by the steps of the methodology. A simultaneous investigation of these two issues is proving particularly fruitful. This paper will focus on advances in the second category.

A major advantage of a process modeling environment, particularly when applied to problems such as batch process development, is the potential to decouple the process model from the numerical solution procedures applied to it. In addition to enabling a variety of different calculations to be performed with a single model, this feature frees the engineer to concentrate on the correct formulation of the model and the design, rather than the details of the numerical solution procedures. While this is a very desirable goal, it places very stringent demands and constraints on the robustness and generality of the solution procedures. Our experience has demonstrated that current technologies do not provide the level of robustness or efficiency required for routine application of modeling technology to the batch process development problem.

Detailed modeling of batch processes requires the use of combined discrete/continuous simulation applied to differential-algebraic models exhibiting complex and highly nonlinear behavior [8]. This problem is further complicated by the fact that during a batch operation state variables may vary over many orders of magnitude (e.g. the composition profile in a batch distillation column), and several physical regimes (e.g. the phase changes in a solvent switch operation). Recent research on combined discrete/continuous simulation [7, 9] has led to the development of what is termed an *interpretative* simulator architecture. In contrast to the more conventional code generation approach, in which the model is automatically coded as a FORTRAN subroutine and then linked with numerical solvers, the interpretative approach creates an image of the process model as data structures in machine memory, and during a simulation these data structures are 'interpreted' to pass residuals, partial derivatives, etc., to numerical solvers. The interpretative approach is ideally suited to discrete manipulation of the mathematical model at any point during the combined discrete/continuous simulation [10], and reporting and diagnosis of problems or errors in the solution process [11].

A further advantage of the intepretative architecture is that the complete functional form of the model is available in explicit symbolic form for analysis and/or manipulation throughout the entire simulation. This symbolic information has the potential to be extremely useful in addressing the issue of robustness discussed above. In addition, it prompts an investigation of hybrid symbolic and numerical strategies for more robust and efficient solution of simulation and optimization problems. This paper reports on the progress and results of our preliminary investigations. The current implementation of the interpretative architecture in ABACUSS serves as the platform for our efforts.

The next three sections of the paper identify areas in which the robustness and efficiency of existing numerical techniques can be improved. Section 2 demonstrates shortcomings of current numerical integration techniques for the solution DAEs and identifies improvements. Section 3 demonstrates the potential for exploiting the interpretative architecture for the efficient solution dynamic optimization problems. Finally, section 4 investigates a new method for the solution of large scale highly nonlinear optimization problems.

2 ROBUST NUMERICAL INTEGRATION OF DIFFERENTIAL-ALGEBRAIC SYSTEMS

As noted above, models of batch processes typically give rise to systems of differential-algebraic equations (DAEs):

$$\begin{aligned} \mathbf{f}(\dot{\mathbf{x}}, \mathbf{x}, \mathbf{u}, t) = \mathbf{0} \\ \mathbf{u} = \mathbf{u}(t) \end{aligned} \tag{1}$$

where $\mathbf{x}, \dot{\mathbf{x}} \in \mathbf{R}^n$, $\mathbf{u} \in \mathbf{R}^l$ and $\mathbf{f} : \mathbf{R}^n \times \mathbf{R}^n \times \mathbf{R}^l \times \mathbf{R} \rightarrow \mathbf{R}^n$. Standard BDF codes for numerical integration of DAEs provide certain guarantees on the accuracy of the numerical approximation. Results from the application of ABACUSS as part of a batch process development strategy, particularly the batch distillation of certain wide-boiling mixtures, indicate that under certain situations these guarantees break down. This section demonstrates the new result that a breakdown of the error control mechanism can stem from an ill-conditioned corrector iteration matrix. Bounds are derived that define the conditions under which the accuracy can be guaranteed, and scaling techniques are investigated to mitigate the problem. ABACUSS is currently interfaced to the DASOLV [12] implementation for sparse unstructured systems. Comparisons of DASOLV are made with the widely used dense implementation DASSL [13]

Accuracy is maintained by adapting the step size to control the local truncation error (DASSL also controls the interpolation error, using the more restrictive criteria to determine the allowable step size.) The local truncation error is defined as follows for both DASOLV and DASSL [13]:

$$\text{error} = M \cdot \left\| \mathbf{x}^C - \mathbf{x}^P \right\| \leq 1.0 \tag{2}$$

where $\mathbf{x}^C$ is the corrected solution and $\mathbf{x}^P$ is the predicted solution. In DASOLV M is defined as the inverse of the step size (h); M varies with the order of the method and the step size in DASSL, but for a first order method when $h_{n+1} \ll h_n$, M approaches $\frac{h_{n+1}}{h_{n+1}+h_n}$. Note that in both cases the truncation error scales with the integration step size, and the user requested tolerances are buried in the definition of norm used in (2).

The DASOLV implementation allows the step size to be reduced up to eight times before declaring that the step is too small. This permits large differences between the predicted and corrected values of certain variables to be accepted when the step size becomes small.[1] For example, Figure 1 shows the trajectory of the condenser duty for a batch distillation simulation performed with ABACUSS. The model has no discontinuities, and the observed 'spikes' are the result of successful integration steps with a very small step size. Effectively, the error control mechanism has broken down but solution has continued. On the other hand, the DASSL implementation defines a minimum allowable step size. This criterion is more likely to cause the equally undesirable premature termination of the simulation (a familiar phenomenon to experienced users of these codes).

The fact that DASOLV continues integration has enabled elucidation of the source of the problem: an ill-conditioned corrector iteration matrix. The corrector employs a modified Newton method, terminating iterations based on the size of the update vector $\Delta\mathbf{x}$ calculated in exact arithmetic.

$$\|\Delta\mathbf{x}\| \leq \tau \tag{3}$$

Assuming that the predictor provides an initial guess within the region of convergence of Newton's method and that the operations are performed using exact arithmetic, the superlinear convergence of Newton's method [14] bounds the distance from the current iterate $\mathbf{x}_k$ to the solution $\mathbf{x}^*$ using the Newton update $\Delta\mathbf{x}$ and the convergence rate β_k as follows:

$$\|\mathbf{x}_{k+1} - \mathbf{x}^*\| \leq \frac{\beta_k}{1-\beta_k} \|\Delta\mathbf{x}_k\| \leq \tau \frac{\beta_k}{1-\beta_k} \tag{4}$$

---

[1] The norm employed in DASOLV, a weighted root mean square norm, is scaled by the system size, so it is less restrictive than a weighted infinity norm.

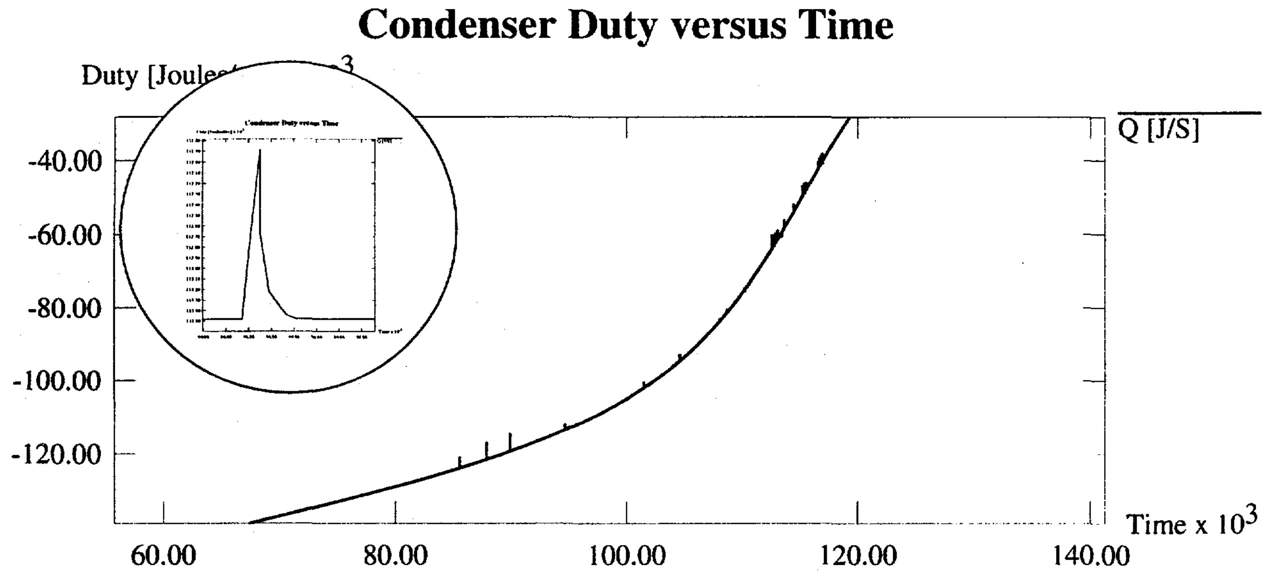

Figure 1: Plot of condenser duty resulting from ABACUSS simulation.

Unfortunately, the criterion defined in (3) cannot be applied directly because the only information available is the size of the Newton update $\overline{\Delta \mathbf{x}}$ calculated using floating point arithmetic. However, as long as the current iterate is within the region of convergence, we need only demonstrate that (3) is satisfied to attain the desired accuracy. The following linear error analysis uses $\overline{\Delta \mathbf{x}}$ and the condition number of the iteration matrix ($\kappa(\mathbf{J})$) to derive conditions under which (3) must hold.

The criterion of (3) dictates that $\Delta \mathbf{x}$ must lie in a closed neighborhood of the origin of radius τ, defined by $N_\tau(0)$. Although the exact location of $\Delta \mathbf{x}$ is not known, $\Delta \mathbf{x}$ must lie within a closed neighborhood of radius $r \geq \|\boldsymbol{\delta x}\|$ of the numerically calculated update $\overline{\Delta \mathbf{x}}$. Thus, (3) will hold as long as $N_r(\overline{\Delta \mathbf{x}}) \subset N_\tau(0)$. Linear error analysis is used to prove the following: If there exists a $\overline{\Delta \mathbf{x}}$ such that (5) and (6) are satisfied, then $N_r(\overline{\Delta \mathbf{x}}) \subset N_\tau(0)$.

$$\left\|\overline{\Delta \mathbf{x}}\right\| \leq \frac{\tau}{1+\kappa(\mathbf{J})\frac{\|\boldsymbol{\delta J}\|}{\|\mathbf{J}\|}} \tag{5}$$

$$\left\|\overline{\Delta \mathbf{x}}\right\| \leq \tau(1-\kappa(\mathbf{J})\frac{\|\boldsymbol{\delta f}\|}{\|\mathbf{f}\|}) \tag{6}$$

Linear perturbation analysis provides the following bounds.

$$\frac{\|\boldsymbol{\delta x}\|}{\|\Delta \mathbf{x}+\boldsymbol{\delta x}\|} \leq \kappa(\mathbf{J})\frac{\|\boldsymbol{\delta J}\|}{\|\mathbf{J}\|} \tag{7}$$

$$\frac{\|\boldsymbol{\delta x}\|}{\|\Delta \mathbf{x}\|} \leq \kappa(\mathbf{J})\frac{\|\boldsymbol{\delta f}\|}{\|\mathbf{f}\|} \tag{8}$$

Combining (5) and (7) using the triangle inequality produces (9) which shows that $\|\Delta \mathbf{x}\| \leq \tau$.

$$\tau \geq \left\|\overline{\Delta \mathbf{x}}\right\|(1+\kappa(\mathbf{J})\frac{\|\boldsymbol{\delta J}\|}{\|\mathbf{J}\|}) \geq \left\|\overline{\Delta \mathbf{x}}\right\| + \|\boldsymbol{\delta x}\| \geq \|\Delta \mathbf{x}\| \tag{9}$$

Given that $\|\Delta \mathbf{x}\| \leq \tau$, (8) provides an upper bound for $\|\boldsymbol{\delta x}\|$.

$$\|\boldsymbol{\delta x}\| \leq \kappa(\mathbf{J})\,\|\Delta \mathbf{x}\|\,\frac{\|\boldsymbol{\delta f}\|}{\|\mathbf{f}\|} \leq \kappa(\mathbf{J})\frac{\|\boldsymbol{\delta f}\|}{\|\mathbf{f}\|}\tau \;=\; r \tag{10}$$

(6) shows that $\left\|\overline{\Delta \mathbf{x}}\right\| + r$ is bounded from above by τ, which implies that $\|\boldsymbol{\delta x}\| \leq \tau$ by applying the triangle inequality. Thus, $N_r(\overline{\Delta \mathbf{x}}) \subset N_\tau(0)$, an (3) must hold.

In the best case, the only error in the calculation process comes from storing the original data, so the error in the data is bounded by the machine unit roundoff ϵ. In this case, $\|\boldsymbol{\delta f}\| \leq \epsilon \|\mathbf{f}\|$ and $\|\boldsymbol{\delta J}\| \leq \epsilon \|\mathbf{J}\|$. Thus, (6) reduces to (11).

$$\left\|\overline{\Delta \mathbf{x}}\right\| \leq \tau(1 - \kappa(J)\epsilon) \tag{11}$$

If the condition number is high, then we admit the possibility that the accuracy cannot be maintained. The condition number of the iteration matrices from the previously mentioned batch distillation experiments, show that it is impossible to find a $\overline{\Delta \mathbf{x}}$ to satisfy (11).

To obtain solutions to such numerical experiments, the condition number of the iteration matrix must be reduced, or the simulation must be performed in higher precision. Scaling the variables and the equations of the model offers the opportunity to improve the conditioning of the matrix. An ad hoc application of variable and equation scaling on the distillation model has shown significant improvement in the conditioning of the iteration matrix. Therefore, automated scaling techniques are currently being implemented within ABACUSS. Variables are adaptively scaled throughout the simulation, since a given variable may change over orders of magnitude during the simulation of a batch operation. The equations will be scaled based on their functional form.

3 HIGH-INDEX FORMULATIONS FOR DYNAMIC OPTIMIZATION

A subproblem of batch process development is the design of optimal operating policies for individual processing tasks [5]. For example, system level targets may require the selectivity from a reaction task to be maximized, and this can be achieved by searching for the optimal time profiles for reactant feed rate and reactor temperature. This subproblem can in principle be posed as a dynamic optimization problem. However, adequate models are relatively large and must reflect nonideal phase behavior, complex reaction kinetics, and discontinuous physical behavior. Further, formulations must accurately reflect equipment constraints such as design pressures, which typically translate into path inequality and equality constraints. The combination of these issues poses severe problems for current dynamic optimization algorithms [15, 16]. This section introduces a combined symbolic and numerical strategy that has the potential to solve large scale dynamic optimization problems with general path constraints in an efficient manner.

The *index* of a differential-algebraic system is defined as the smallest integer I such that the system formed from equations 1 and their first I time derivatives define $\dot{\mathbf{x}}(t)$ as locally unique functions of $\mathbf{x}(t)$ and t [13]. According to this definition, a system of ODEs is index-0. The term *high-index* is usually used to refer to systems with index ≥ 2. High-index DAEs can occur for two reasons. On the one hand, equations 1 may be inherently high index due to engineering assumptions made in the derivation of the model. On the other hand, the index of the system may be raised by the choice of which subset of model variables are specified as explicit functions of time $\mathbf{u}$ in order to satisfy the degrees of freedom (DOF). This latter property is of interest here. Note that in this context, even a system of ODEs may be made high index by specifying an output trajectory rather than an input trajectory.

In dynamic optimization, the functions $\mathbf{u}(t)$ are the decisions. If path equality constraints involving $\mathbf{x}$ are appended to equations 1, this reduces the DOF and raises the index. Path inequality constraints can be treated in a similar manner by introducing slack variables. In this case, the index is raised locally while the inequality is active. Hence, any solution method must adapt to changes in the index as the trajectory is traced.

The control parameterization approach to the solution of dynamic optimization problems [16] relies on a decomposition in which an augmented DAE system is repeatedly integrated to evaluate the objective function and gradients for a master NLP, which has as its decision variables the parameters of the basis functions chosen to approximate $\mathbf{u}(t)$. Current approaches [16] avoid the difficulties associated with integration of high-index systems [17] by removing path constraints from the DAE system, and lumping their violation over the entire time interval into terms in the master NLP. This infeasible path approach is less than satisfactory because the master NLP is provided with little information concerning the path constraints, and this leads to an excessive number of expensive DAE integrations.

We are investigating a feasible path control parameterization approach that includes all path constraints explicitly in the DAE subproblems. This should lead to a dramatic reduction in the number of DAE integrations required to solve path constrained problems. This work is predicated on the ability to solve high index systems reliably. Mattsson and Soderlind [18] have presented an algorithm in which the over-determined system of index-1 DAEs that can be derived from a high index system by differentiation is made fully-determined by the symbolic substitution of time derivative variables by 'dummy' algebraic variables. However, there are no reports on the application of this algorithm to anything other than small problems due to numerical issues associated with a large-scale implementation (dummy pivoting). We are currently resolving these issues and implementing the algorithm in ABACUSS.

Mattsson and Soderlind's approach uses Pantelides' [19] structural algorithm to identify which equations to differentiate in order to derive the index-1 system, and symbolic differentiation can perform the necessary differentiations. We have successfully implemented these two steps in ABACUSS and are currently using this feature for consistent initialization of large scale high-index DAE systems.

We have also demonstrated that certain classes of dynamic optimization problems can be solved extremely efficiently by deliberately making them high-index. In this case, the problem reduces to a NLP in terms of the model variables at a finite number of points. This is similar to the collocation approach [15] but gives rise to NLPs that are dramatically smaller.

4 ROBUST OPTIMIZATION OF LARGE SCALE HIGHLY NONLINEAR PROBLEMS

Many problems in process development and design give rise to large, highly nonlinear mathematical programming problems. Consider the following nonlinear program (NLP):

$$\min_{\mathbf{x}} f(\mathbf{x}) \tag{12}$$

$$\text{s.t.}\ \mathbf{h}(\mathbf{x}) = \mathbf{0} \tag{13}$$

$$\mathbf{g}(\mathbf{x}) \geq \mathbf{0} \tag{14}$$

The first-order necessary conditions for optimality are the well known Karush-Kuhn-Tucker (KKT) conditions, which are a mixture of nonlinear equations and inequalities. It is shown by Mangasarian that the complementary slackness condition in the KKT conditions can be reformulated as an equivalent set of nonlinear equations [20]. After applying Mangasarian's theorem, the KKT conditions become:

$$\nabla f(\mathbf{x}) - \nabla \mathbf{h}(\mathbf{x})^T \mathbf{v} - \nabla \mathbf{g}(\mathbf{x})^T \mathbf{u} = \mathbf{0} \tag{15}$$

$$\mathbf{h}(\mathbf{x}) = \mathbf{0} \tag{16}$$

$$M(|g_i(\mathbf{x}) - u_i|) - M(g_i(\mathbf{x})) - M(u_i) = 0 \quad \forall i \tag{17}$$

where $M : R \longrightarrow R$ is a strictly increasing function with $M(0) = 0$. This set of equations will be solved using the globally convergent homotopy continuation method. A similar approach has been proposed by Brengel and Seider [21] in an attempt to coordinate design and control optimization and by Sun and Seider [22] in Gibbs free energy minimizations. The ability to dervive equations (15–17) automatically by symbolic differentiation and manipulation in an equation-oriented simulation environment plays a pivotal role in this approach for solving large-scale NLPs. In addition, symbolic manipulation techniques are being investigated to improve the performance of the homotopy continuation method itself.

Homotopy continuation has been used in the past to solve systems of equations when a good starting point is not known or when the equations contain many singularities. Suppose $\mathbf{F}(\mathbf{x}) = 0$ is a set of equations we are interested in solving. One popular homotopy is the convex linear homotopy given by:

$$\mathbf{H}(\mathbf{x}, \lambda) = \lambda \mathbf{F}(\mathbf{x}) + (1 - \lambda)\mathbf{G}(\mathbf{x}) \tag{18}$$

where λ is the homotopy parameter and $\mathbf{G}(\mathbf{x})$ is set of equations which has a known solution $\mathbf{x}^0$. The idea behind homotopy continuation is to begin at $\lambda = 0$ and $\mathbf{x} = \mathbf{x}^0$, where $\mathbf{H}(\mathbf{x}^0, 0) = 0$, and track the homotopy path given by $\mathbf{H}(x, \lambda) = 0$ to $\lambda = 1$ and $\mathbf{x} = \mathbf{x}^*$, a solution of $\mathbf{F}(\mathbf{x}) = 0$.

One particular homotopy is the Newton homotopy where $\mathbf{G}(\mathbf{x}) = \mathbf{F}(\mathbf{x}) - \mathbf{F}(\mathbf{x}^0)$. The homotopy map is given by:

$$\mathbf{H}(\mathbf{x}, \lambda) = \mathbf{F}(\mathbf{x}) - (1 - \lambda)\mathbf{F}(\mathbf{x}^0) \tag{19}$$

Parameterizing $\mathbf{x}$ and λ with respect to the arclength of the homotopy path, and differentiating, we obtain:

$$\nabla \mathbf{F}(\mathbf{x})\frac{d\mathbf{x}}{ds} + \mathbf{F}(\mathbf{x}^0)\frac{d\lambda}{ds} = 0 \tag{20}$$

Combining this equation with equation (19) and rearranging, we obtain:

$$\frac{d\mathbf{x}}{ds} = \frac{d\lambda/ds}{1 - \lambda}\nabla \mathbf{F}(\mathbf{x})^{-1}\mathbf{F}(\mathbf{x}) \tag{21}$$

Now consider the global Newton method. The global Newton method can be interpreted as the integration of the autonomous ODE system:

$$\frac{d\mathbf{x}}{dt} = -\nabla \mathbf{F}(\mathbf{x})^{-1}\mathbf{F}(\mathbf{x}) \tag{22}$$

A damped Newton method, given by the iteration formula

$$\mathbf{x}^{k+1} = \mathbf{x}^k - \alpha^k \nabla \mathbf{F}(\mathbf{x}^k)^{-1}\mathbf{F}(\mathbf{x}^k) \tag{23}$$

can be obtained by a first-order explicit integration of equation (22) with a stepsize, α^k, selected such that $\left\|\mathbf{F}(\mathbf{x}^{k+1})\right\| \leq \left\|\mathbf{F}(\mathbf{x}^k)\right\|$. Now consider the successive quadratic programming (SQP) algorithm for nonlinear optimization. SQP converges to an optimum by obtaining search directions from the solution of a quadratic program (QP) subproblem formed by taking quadratic approximations of the objective function and linear approximations of the constraints. The current point is updated by moving in the direction obtained in the QP a stepsize determined by minimizing some merit function. It can be shown that the directions obtained in the QP subproblem are the same as the directions obtained by applying Newton's method to the KKT conditions of the NLP, considering only the active constraints (i.e. inequality constraints equal to zero). Thus, SQP can be interpreted as applying a damped Newton method to the KKT conditions. In the homotopy continuation approach for solving NLPs, the KKT conditions are solved using homotopy continuation. The relationship between homotopy continuation and the damped Newton method indicates that SQP and the homotopy continuation approach for solving NLPs are quite similar.

Although these two approaches are similar, using homotopy continuation has the following advantages. First, homotopy continuation can locate solutions where other methods fail due to both lack of a good initial guess and the presence of singularities. Homotopy continuation is globally convergent with probability 1 [23] and, unlike the related global Newton method, remains stable near singular points [24]. Second, under reasonable assumptions, the homotopy path given by (18) is a connected one-dimensional submanifold. This feature makes it possible to track out several solutions using homotopy continuation. Being able to track out multiple (possibly all) KKT points is, in many cases, better than obtaining a single global minimum (for example, the global minimum is useless if it is not possible to control the plant when operating at that point). Finally, deriving equations (15–17) does not change the sparsity of the original problem. Therefore, this approach should be able to handle large NLPs with many degrees of freedom. These properties suggest this approach has the potential to be effective in solving large-scale, non-convex NLPs with highly nonlinear constraints and many degrees of freedom, where the performance of SQP is seriously degraded.

Acknowledgments — This work was supported by the United States Department of Energy under grant DE-FG02-85ER13331.

References

[1] L. B. Evans, "Steady-state simulation: A state-of-the-art review," in *The Fifth International Symposium on Process Systems Engineering*, (Kyongju, Korea), pp. 953–967, July 1994.

[2] AspenTech, *SpeedUp User Manual Release 5.4*. Aspen Technology UK Ltd., 1993.

[3] A. W. Westerberg, K. Abbot, and B. Allan, "Plans for ASCEND IV: Our next generation equation-based modelling environment," in *AspenWorld 1994*, (Boston, Massachusetts), November 6–9 1994.

[4] H. W. Ray, "Dynamic modelling of polymerization process flowsheets using POLYRED," in *1st Industrial Chemical Engineering Technology Topical Conference, AIChE Annual Meeting*, (St. Louis, USA), November 7–12 1993.

[5] R. J. Allgor, M. D. Barrera, P. I. Barton, and L. B. Evans, "Optimal batch process development," in *The Fifth International Symposium on Process Systems Engineering*, (Kyongju, Korea), pp. 153–157, July 1994.

[6] C. C. Pantelides and P. I. Barton, "Equation-oriented dynamic simulation current status and future perspectives," *Computers Chem. Engng*, vol. 17, pp. S263–S285, 1993.

[7] P. I. Barton, *The Modelling and Simulation of Combined Discrete/Continuous Processes*. PhD thesis, University of London, 1992.

[8] P. I. Barton, "Batch process simulation: Why and how," in *AspenWorld 1994*, (Boston, Massachusetts), November 6–9 1994.

[9] P. I. Barton and C. C. Pantelides, "gPROMS - a combined discrete/continuous modelling environment for chemical processing systems," *Simulation Series*, vol. 25, no. 3, pp. 25–34, 1993.

[10] P. I. Barton and C. C. Pantelides, "The modelling of combined discrete/continuous processes," *AIChE Journal*, vol. 40, no. 6, pp. 966–979, 1994.

[11] P. C. Piela, *ASCEND An Object-Oriented Computer Environment for Modeling and Analysis.* PhD thesis, Carnegie-Mellon University, 1989.

[12] R. B. Jarvis and C. C. Pantelides, "DASOLV — a differential algebraic equation solver," tech. rep., Centre for Process Systems Engineering, Imperial College, London, March 1992.

[13] K. E. Brenan, S. L. Campbell, and L. R. Petzold, *Numerical Solution of Initial-Value Problems in Differential Algebraic Equations.* New York: Elsevier Science Publishing Co., Inc., 1989.

[14] J. J. Moré and D. C. Sorensen, "Newton's method," in *Studies in Numerical Analysis* (G. H. Golub, ed.), pp. 29–83, ??, 1984.

[15] J. E. Cuthrell and L. T. Biegler, "On the optimization of differential-algebraic process systems," *AIChE J.*, vol. 33, pp. 1257–1270, 1987.

[16] V. S. Vassiliadis, *Computational Solution of Dynamic Optimization Problems with General Differential-Algebraic Constraints.* PhD thesis, University of London, 1993.

[17] L. R. Petzold, "Differential/algebraix equations are not ODEs," *SIAM J. Sci. and Stat. Comp.*, vol. 3, pp. 367–384, 1982.

[18] S. E. Mattsson and G. Soderlind, "Index reductiion in differential-algebraic equations using dummy derivatives," *SIAM J. Sci. and Stat. Comp.*, vol. 14, pp. 677–692, 1992.

[19] C. C. Pantelides, "The consistent initialization of differential-algebraic systems," *SIAM J. Sci. and Stat. Comp.*, vol. 9, pp. 213–231, 1988.

[20] O. L. Mangasarian, "Equivalence of the complementarity problem to a system of nonlinear equations," *SIAM J. Appl. Math*, vol. 31, p. 89, 1976.

[21] D. D. Brengel and W. D. Seider, "Coordinated design and control optimization of nonlinear processes," *Computers and Chemical Engineering*, vol. 16, pp. 861–886, 1992.

[22] A. C. Sun and W. D. Seider, "Mapped homotopy continuation algorithm for global optimization," in *Recent Advances in Global Optimization*, 1991.

[23] L. T. Watson, "Hompack: A suite of codes for globally convergent homotopy algorithms," *ACM Transactions on Mathematical Software*, vol. 13, pp. 281–310, 1987.

[24] E. L. Allgower and K. Georg, *Numerical Continuation Methods.* New York: Springer-Verlag, 1990.